Two-Dimensional Infrared Spectroscopy of Heterogeneous Systems: On the Path to

Measuring Charge Transfer in Solution Processed Organic Electronic Thin Films

A Thesis
SUBMITTED TO THE FACULTY OF THE UNIVERSITY OF MINNESOTA

BY
Ivan C. Spector

IN PARTIAL FULLFILLMENT OF THE REQUIREMENTS FOR THE DEGREE OF
DOCTOR OF PHILOSOPHY

Adivsor Aaron Massari

December 2020

Acknowledgements

It is my personal conviction that I would be remis if I didn't thank my God for the opportunities and work set before me. I am a Christian and I credit all that I am to my faith. Though I credit all things I am thankful for to God, I recognize that this is not everyone's viewpoint so I would like talk about something more relatable; the people and things I have deep gratitude for.

First, I am very grateful to and for Aaron Massari. He is an exceptional advisor both scientifically and personally. He repeatedly has put the path of his students at the forefront of his guidance. He has been infinitely understanding as I went through a divorce shortly after my preliminary exam. He has been patient with the personal struggles of other lab members. He is calm and collected in the midst of stress over research, grant writing, lab operations, and his own difficult personal circumstances. I have never seen him judge with bias or act petty. In addition to his exceptional moral character he managed to run a physical chemistry lab with multiple spectroscopic techniques running a laser at 150% efficiency. I could not have asked for a better advisor.

Secondly, I am grateful to the University of Minnesota. I do not know another person in my extended family or from my childhood that pursued and achieved a PhD. This could not have happened without guidance at Saint Cloud State University from Michael Dvorak. His guidance led me to apply for a Lando Summer Research Experience. I received this and worked under Steven Kass who would have been my next choice for advisor.

Coming into graduate school with a wife and two children was challenging but completely doable with a supportive wife. I also received a 3M fellowship from the University of Minnesota and the approval of Bill Tohlman to work 10 hours per week outside of research to meet the financial needs of my family. In this vein I am thankful for my NSF fellowship that allowed me to support my family and ultimately pay for a costly divorce so that I did not lose custody of my children.

Thirdly, I'm thankful for all the academics and intellectuals that I was privileged to spend so much time with. I left graduate school with five amazing friends: Gereon Wuu-Yee (formerly Yee), Benjamin Geisbauer, Guillem Dehoe, Cynthia Pyles, and Samuel Egger. I would never have been able to continue to put one foot in front of the other without them. Professors like Andreas Stein, Ilja Siepmann, Chris Cramer, James Johns, Renee Frontiera, David Blank, Ken Liepold, and Steven Kass allowed me to accost them with conversation whenever I saw them. These conversations were scientific, philosophical, or personal. The time and patience these professors gave me was invaluable. As a graduate student it is easy to feel like less than all these professors. However, at the University of Minnesota, in nearly 100% of interactions I had with professors they were patient, humble, and kind. This enabled me to carry on when things were difficult or quite frankly I felt stupid.

Fourth, I could have done none of this without the support staff. Nancy Thao is an amazing administrator who simplified all the paperwork along the way. Dan McEwan is an invaluable resource for using all forms of software. All the IT folks are fantastically helpful. Everyone involved in outreach like U on the Prairie, Energy and U, and the State Fair Exhibits deserve all our gratitude. We all have our place in society and there is

necessity as well as deep personal reward in drawing people into the discussion about scientific solutions to basic needs like food, medicine, and energy. We're not all scientists but none of us could hardly be without our administrators, facilities personnel, and the countless other fundamentally necessary individuals. I cannot emphasize their part enough.

Finally, I must acknowledge my wife Betsy and my children. My wife is an amazing woman and I cannot believe how fortunate I am to have found my person. My children bring so much magic to my life and because of my education I can teach them to think critically. My hope is that one of the benefits of all that I have been blessed with will carry on in them for future generations. So, while I acknowledge my personal faith in all this, it is just that; personal. It does not dictate the needs or choices of others. I'm grateful that science brings a focus to our common ground as a species. I'm grateful for all the faith, art, and philosophy that allows us to enjoy our shared human experience.

Abstract

Research Motivation

Entering graduate studies, I had a clear vision: renewable, tunable, biodegradable organic electronics. Renewable technologies and luxuries enjoyed by society might prevent catastrophe due to energy shortage as demand increases. With this vision in mind, my focus was to work towards applications of organic electronics. Specifically, work towards the goal of biodegradable, tunable, renewable organic electronics was focused on heterogeneous systems. Scientists and engineers most often work with composites, mixtures, and amorphous materials and Nature has produced optimized structures that are heterogeneous. Recognizing this and knowing that energy is the world's primary concern motivated the study of electronic processes in heterogeneous systems.

Being a physical chemist with a background in automotive repair meant having an interest in both fundamental science and its applications. I believed that the farthest reaches of computation could meet the farthest reaches of experiment on challenging but applicable systems. Applicable implies commercially and industrially viable systems. This also implies ease of processing which is often associated with an increase in heterogeneity. Ideally, measuring charge transfer in heterogeneous organic electronics on a mechanical level would enable their rational design. Mechanical here refers to ultrafast time scales or molecular scales. For example, the measurement of the rate of individual charges hopping would be the mechanical level as opposed to a thermodynamic bulk level measurement like charge mobility or conductivity.

Researching the connection between mechanical properties like ultrafast vibrational dynamics or molecular charge hopping and then correlating thermodynamic bulk properties of heat capacity, charge mobility, or conductivity is still an enticing challenge. Bulk properties that have been historically observed are catalysis reaction rates, charge mobility, large-scale morphological changes like glass transition or annealing, coefficient of thermal expansion, etc. Their mechanical corollaries would be molecules reaching transition states, charge hopping between molecular sites or distinct subensembles as opposed to bulk mobility, or ultrafast changes in vibrational correlation as these processes occur. Catalysis is an example of why this might be of interest. For a rate of catalysis with a given concentration, one could have 100% of the catalytic species facilitating 10 times the uncatalyzed reaction rate. Alternatively, one could have 1% of the catalytic species facilitating 1000 times the uncatalyzed reaction rate. Both scenarios would appear the same on the thermodynamic level but would differ on the mechanical level. Rational design of chemical systems begins at the mechanical level, but the effects of interest are often observed on the bulk scale.

This connection between the quantum mechanical and the thermodynamic is an open area of research both theoretically and experimentally. These connections are almost completely obfuscated for disordered systems and in many respects are only approachable with phenomenological analysis. Affirming or negating hypotheses that specific vibrational dynamics unique to each molecular configuration give rise to protein function, catalytic mechanisms, or are the source of the apparent charge mobility ceiling in organic electronics (OEs) would change the direction of a tremendous amount of research effort. To illustrate with another example, if it were known that charge mobility were limited by

charge hopping rates, and charge hopping was limited by molecular motions modulating wavefunction overlap, then the applications of OEs would be limited. If this were known, it would prevent wasted effort on applications that were practiallly beyond reach. Similarly, if a catalytic species had only a small population of extremely active conformers it would be necessary to know this in order to improve their function in an efficient rational way.

Given the challenges in applying theory to heterogeneous systems, comparative experiments are one way to connect 2D-IR data to physical processes on both the thermodynamic and mechanical level. This approach involves changing one variable within the molecule or system, observing changes in spectra, and then connecting these to system properties to enable rational design of systems or their moieties. The ultrafast time scales of 2D-IR and its multidimensional nature allow one to decompose ensembles within heterogeneous systems experimentally. Then the efficient application of theory to a subset of a system is approachable. This is opposed to the currently intractable task of modeling an entire heterogeneous system and all its properties at once. Ultrafast 2D-IR is a technique capable of decomposing ensemble measurements and monitoring their dynamics on femtosecond time scales. The capabilities of this technique are manifest in the results below: measurement of temperature dependent intramolecular proton exchange rates, gas adsorption and exchange within heterogeneous systems, solvent effects on complex formation, and morphological changes in the surfaces of nanoparticles.

Research Progression by Chapter

The holy grail of measuring ground state charge transfer with 2D-IR still beckons. However, work toward this measurement resulted in a variety of successful research projects and publications. First, was modification of the laser system to overcome the problem of scatter, or unwanted light swamping 2D-IR signals. Experimental challenges of scatter were apparent when attempting measurements on nanoparticle systems. These challenges prompted instrument modification to cancel the scattered laser light which is often resultant from heterogeneous solid-state samples. Scatter cancellation is based on the phase relationship between the measured 2D-IR signal and the pulse that stimulates its emission. These two pulses can be modulated simultaneously to maintain their phase relationship while also being modulated against other pulses. The modulation against other pulses causes electric fields to cancel. This work is presented in Chapter 2.

While searching for a solution to scatter a concurrent research project less susceptible to its challenges began: study of a catalyst in solution. Experimentally it was less challenging but arduous data analysis was required to extract temperature dependent intramolecular proton exchange in a dimeric ruthenium hydrogenation catalyst (Shvo's catalyst or Shvo). This was in a homogeneous system composed of a hydrogenation catalyst in solution. Clean optics and homogeneous solution samples avoided scatter with comparatively minimal experimental effort. This work is presented in Chapter 3.

Synthesis of Shvo analogues as well as numerous DFT calculations were integral to confirming results of this study. The result was measurement of the activation energy for proton exchange between two cyclopentadienyl ligands. Initial intentions were the investigation of the correlation function of a hydrogenation catalyst in solution to build on previous research. When analyzing the cross peaks in 2D-IR spectra the lifetimes were

longer than expected. This increased cross peak lifetime was ultimately explained by vibrational exchange convoluted with anharmonic coupling. The exchange signals were attributed to intramolecular proton exchange between ligands. Explaining this required computation, synthesis, and temperature dependent 2D-IR studies. My results challenged the nature of the structure of the catalytic species which is an open question about Shvo's catalyst. The rate of exchange is the upper bound for the rate of catalysis based on the currently accepted hydrogenation mechanism. This work was foundational for understanding the exchange signals in 2D-IR spectra that would appear the same if they were due to other phenomena, one of which might be charge transfer.

Following this were exchange measurements on the surfaces of intrinsic and doped silicon nanoparticles (SiNPs) which elucidated surface domain segregation. The measurement of SiNPs was exploratory and was not expected to yield results beyond vibrational lifetimes and possibly spectral diffusion similar to Shvo. We were shocked to see exchange and this observation prompted a comparative study that brought to light the challenges in nanoparticle synthesis. Silicon nanoparticle studies highlighted the sensitivity of the nanoparticle surface to dopants. Many other nanoparticle properties are sensitive to the surface and therefore the study highlighted the need to explore a narrower range of synthesis conditions in greater detail. This is presented in Chapter 4.

Measurement of the rovibrational spectra of gaseous CO_2 follows this in Chapter 5. Interest in gas adsorption and interaction with surfaces arises from a multitude of applications. This directly mattered for CO_2 adsorbed to metal-organic frameworks (MOFs) and iodine adsorbed to a self-assembled monolayer (SAM) of a light absorbing ruthenium compound on the surface of a thin film of titanium dioxide nanoparticles

(N3@TiO$_2$). An understanding of a pure gas measurement using 2D-IR is then a good place to start to understand a more complex system.

Finally, the longest standing research project is measurements of iodine complexation to N3 tethered to the surface of TiO$_2$ nanoparticles. The culmination of this work was an increased understanding of the intra and intermolecular contributions to vibrational dynamics as well as the complexity of solvent and complex effects on vibrational dynamics. This is found in the closing chapter. Gaseous iodine was initially introduced into the film to increase conductance. Though this increased conductance it did not result in measurable charge transfer between N3 molecules, however it did reveal dynamics sensitive to iodine adsorption and complexation. Gas adsorption and solvent effects on vibrational dynamics in iodine doped films were measured here. This work was the inception of nanoparticle film studies and the final chapter; 6.

Dye sensitized solar cells (DSSCs), specifically the Graetzel cells, were chosen for study based on the hypothesis that their isothiocyanate (SCN) ligands were directly involved in charge transfer. This suggested that ground state charge transfer could be observed via the SCN ligands. The SCN ligands have a strong transition dipole and long lifetime similar to the four CO ligands in Shvo. Though observation of CT was never realized, this research project proved fruitful.   Vibrational lifetime effects due to complexation of iodine to DSSCs were observed. Spectral diffusion was also observed to change both dramatically and non-intuitively. This is important because an I$_2$/I$_3^-$ redox couple is used in these cells. The results raise questions about intermolecular interactions in these systems and our understanding of how they mechanistically impact DSSC efficiency.

The DSSC and SiNP systems displayed large amounts of static inhomogeneity or heterogeneity in the chromophore environment. Various measurements of polymer thin films were carried out along the way as well as several solution phase studies which are not presented here. Computation was utilized throughout these as necessary and was a necessary tool in analyzing experimental results.

Table of Contents

List of Tables

List of Figures

Abbreviations

CLS – centerline slope

CT – Charge transport

CW – Continuous wave

DFFT – Digital fast Fourier transform

DSSC – Dye-Sensitized Solar Cell

FFCF – Frequency-frequency correlation function

FWHM – Full width at half maximum

HDMA – hexadecyl malonic acid

IVR – intramolecular vibrational energy redistribution

LO – Local oscillator

MCT – HgCdTe detector

N3 - cis-diisothiocyanato-bis(2,2'-bipyridyl-4,4'-dicarboxylic acid) ruthenium(II)

NP - nanoparticle

OE – Organic electronic

OFET – Organic field effect transistor

SAM – Self-Assembled Monolayer

VER – Vibrational Energy Relaxation

VET – Vibrational Energy Transfer

Z907 - cis-diisothiocyanato-(2,2'-bipyridyl-4,4'-dicarboxylic acid)-(2,2'-bipyridyl-4,4'-dinonyl) ruthenium(II)

Chapter 1 Two-Dimensional Infrared Spectroscopy

1.1 Introduction and Motivation for 2D-IR of Heterogeneous Systems

Spectroscopy in one form or another has fascinated scientists for centuries. It has satisfied our greatest curiosities, solved intractable problems, and changed our lives in incalculable ways. Spectroscopy is responsible for: supporting quantum mechanical theory, NMR aiding chemical research, MRI improving healthcare, measurement of environmental systems giving people EPA guidance, and more. Spectroscopy has been integral to nearly every technological advancement of the 20th century. These successes continue to drive increasingly advanced spectroscopic experimentation aimed at observing the most fundamental physical phenomena. Continuing advances of experimental techniques are the application of sophisticated theories and the resultant engineering in detectors, lasers, processes, materials and controls. The last 20 years have seen the growth of ultrafast spectroscopic techniques that are capable of temporal resolution on the time scale of tens of femtoseconds (fs). This enables direct observation of charge transfer (CT), vibrational motion, polaron formation, plasmon dynamics, and more. The spectral window of the light used in experiments determines both the temporal resolution as well as the physical phenomena that can be observed. Broadening the spectral window that is experimentally accessible coincides with better temporal resolution allowing scientists to elucidate a more complete picture of systems of research.

In any spectroscopic technique, there is the challenge of observing spectral changes or features and rationalizing their molecular origins. Often connections are made to familiar drawings and concepts from organic chemistry where we rely on our first
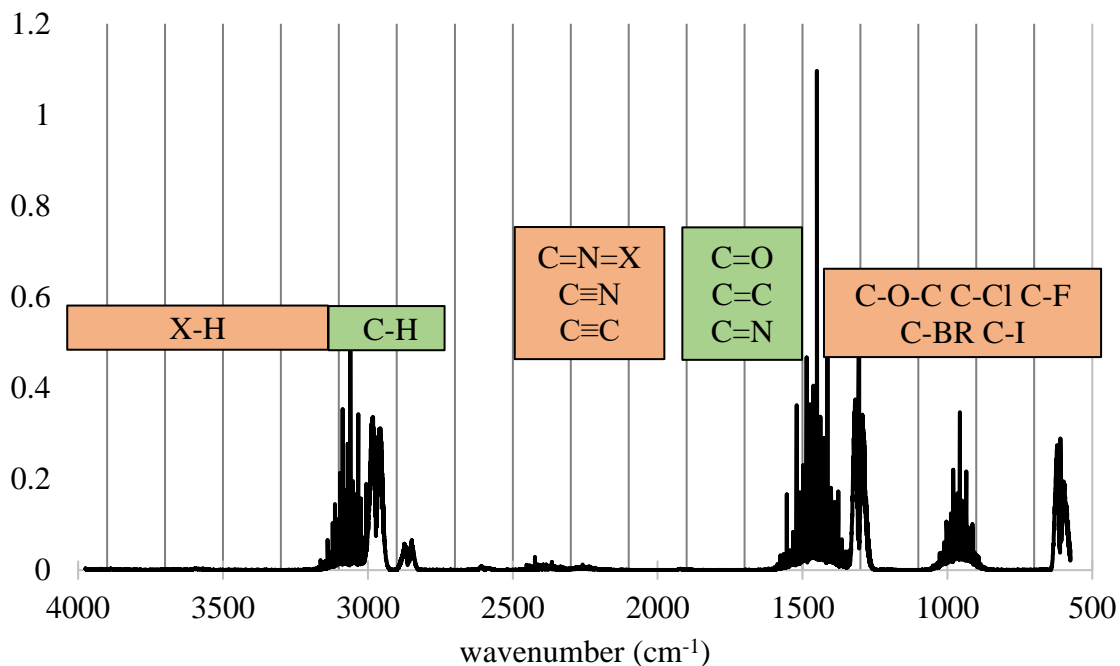
Figure 1: The FTIR spectrum of gas phase bromomethane from NIST is shown above. Labels indicate the approximate regions where normal mode vibrational frequencies for the indicated bonds appear.

conceptions of molecules in terms of fixed bonds and atoms as stationary objects with discrete charges. Charge delocalization can be somewhat conceptualized through the partial charges discussed in resonance structures of molecules with pi bonds.

When these concepts fail, quantum mechanical calculations are at our disposal to obtain a deeper level of understanding beyond the intuitive ideas learned in undergraduate chemistry. Experimentally we can probe the detailed information that comes from theory. For example, linear vibrational spectroscopy (e.g. Fig. 1) provides a wealth of information about available normal modes associated with chemical bonds but is limited by long time ensemble averaging and so cannot resolve mechanistic steps. This is in accord with the

intuitive static system picture. These approaches certainly continue to result in scientific discovery, but the frontier of spectroscopy lies at short time scales, broad spectral range, and small spatial resolution

Temporal resolution is limited by pulse width or spectral collection time. Fourier transform infrared (FTIR) linear spectroscopy uses a light source that emits a broadband spectrum of infrared (IR) light that is largely incoherent but has a small amount of coherence. The light is continuously emitted from a blackbody source meaning that the times at which the light arrives at the detector are controlled using electronics and are longer than vibrational dynamical time scales. It takes seconds to produce an FTIR interferogram. During this time the coherent light from the source is fluctuating on the order of fs but is constant when averaged over the detection time. The light is interacting with the sample continually while the stage in the Michelson interferometer moves the distance required for a spectrum. FTIR uses continuous radiation so the time required to collect a spectrum is the time required to move the interferometer stage to generate an interferogram and this time defines the temporal resolution. Any changes due to molecular dynamics (MD) occurring on times scales shorter than this time will not be resolved. Vibrational modes generally have picosecond (ps) dynamics. Even an FTIR capable of producing scans in a nanosecond would deliver an FTIR with relatively constant peak shapes.

The spectral resolution of an FTIR measurement is limited by how long one wishes to scan in time, making the potential frequency resolution quite high but at the expense of worse temporal resolution. The position and width of peaks provide chemical information via functional group or bond identification. Introducing variables like temperature or

reactants further expands this technique's capability. Its major limitation is the lack of temporal resolution beyond seconds.

Instead of using Fourier transform to obtain absorbance versus wavenumber, one could use temporally short pulses that have a broadband spectrum. Short pulses, as opposed to continuous radiation, can be detected at separate points in time relative to some initial time or background signal. If a pulse of light is 100 fs wide at its full width and half maximum height (FWHM), then it only interacts with a sample for ~100 fs while passing through it. Any dynamics shorter than 100 fs would be averaged out during sample interaction but anything longer can be observed as spectral changes in peak shape or intensity as the time of interaction relative to the initial time is changed. Though the time the light interacts with a detector may be longer, the resolution is still controlled by the interaction with the sample if there is a background or reference spectrum at time zero. The pulses can then be spectrally resolved in a monochromator to measure intensity as a function of wavenumber with and without a sample in the beam, thereby allowing the user to generate an absorbance versus wavenumber plot that is identical to the FTIR result.

This would not provide additional information beyond FTIR spectroscopy with only a background signal without a sample, but if two pulses were used with a delay time between them this would enable new information to be obtained. If temporally narrow pulses were used and the time at which they interact with a sample was controlled, then pump-probe spectroscopy could be performed. Producing temporally narrow pulses intense enough to measure a response requires an intense coherent infrared light source: the laser. With this source the light pulses can be beam-split producing two equivalent pulses termed "pump" and "probe". The pump excites the vibrational oscillators and the

probe measures their evolution in time. After the initial excitation with the pump pulse, the second spectrally broad and temporally narrow pulse provides absorbance versus wavelength data. These data contain both ground state bleach (a lack of absorbance due to less ground state population after excitation) and excited state absorption (absorbance of the excited mode). Ground state bleach and excited state absorption are observed from signal of a probe pulse with a pump pulse relative to a probe pulse without a pump pulse. An initial pump pulse provides a reference time and data for analysis is the difference of signal with and without a pump pulse (Fig. 2).

Most optical measurements require a background or a reference. The probe pulse measurement without a pump provides a reference. Optical spectroscopy often uses "chopping" in which every other spectrum has a pulse blocked by a synchronized rotating chopper for subtraction.[2] The time between the pump and probe pulses can be varied to add a time dimension to the absorption data. Figure 2 depicts a pump-probe experiment. A chopper alternately blocks the pump pulse while the probe pulse passing through the sample provides the background for subtraction. The probe pulse passing through the sample after the pump pulse gives the signal. The pump-probe spectrum is obtained by
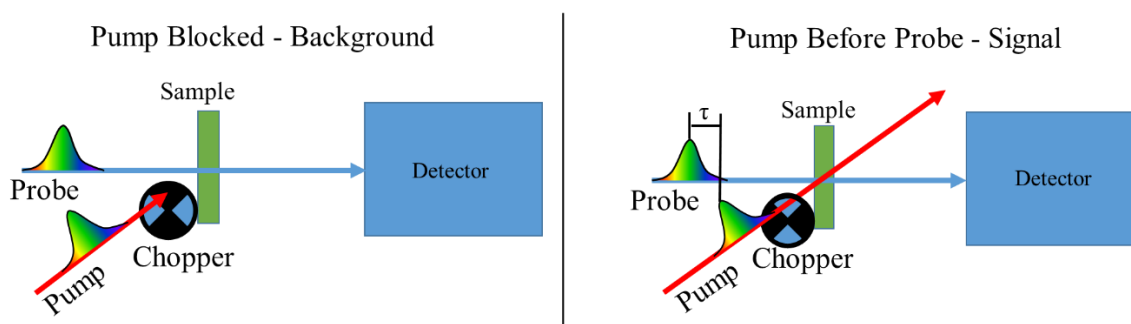
Figure 2: The left figure depicts a chopper blocking the pump beam. A detector measures the probe beam passing through the sample. The right figure depicts a window in the chopper allowing the pump beam to overlap spatially in the sample with the probe beam. The time delay, τ, is the time after the pump pulse arriving at the sample that the peak of the probe pulse arrives at the sample.

subtracting the background from the signal spectrum. For further information another "pump" pulse could be included in the experiment.

Two-dimensional infrared spectroscopy (2D-IR) uses multiple pulses to observe vibrational dynamics on the time scale relevant to the most fundamental processes, such as nuclear and, in some cases, electronic motions. It is a four-wave mixing multidimensional nonlinear spectroscopy: three input fields (pulses) and a fourth emitted. It rests upon quantum mechanical theory analogous to NMR, and similarly can be used to observe coupling between subensembles. An outline of the basic underpinnings of this theory is in section 1.4. If no visible or higher energy light is used, the complication of excited electronic states or excess deposited energy is avoided. Summarily this means 2D-IR has a niche position of measuring the fastest changes of molecules in their electronic *ground* states as they exist and function in electronic materials. The 2D-IR technique is significantly more complicated than linear spectroscopies but provides information otherwise inaccessible.

1.2 Brief History of 2D-IR

The last 20 years have seen the development of multidimensional ultrafast measurement techniques.[3, 4] The first three-pulse heterodyne detected vibrational photon echo experimental results were published by Robin Hochstrasser in 1998.[4] Some of the earliest studies of vibrational dynamics using 2D-IR spectra were of amide bands.[3-5] Research on the amide vibrations using ultrafast infrared spectroscopy continues to grow and further elucidate protein structure.[6] This is observed through peak shape, vibrational lifetime, and rates of vibrational energy transfer (VET). Water continues to be heavily studied due to its unique properties and rich vibrational states with their associated

dynamics.[4, 7] Water spectra indicate inhomogeneous dynamics on unexpected time scales.[8] Exchange of various types in various systems has been studied and as aforementioned is the topic of much of the research presented herein.[9-13]

Theories governing multidimensional spectroscopy are over 60 years old but the advent of intense, fs pulse-length, IR lasers has allowed the application of these theories to vibrational spectroscopy.[1, 14] Theories describing multiple pulse experiments and quantum mechanical phenomena were first applied to spin systems in 1946 and 1957 with the work of Bloch and Fano.[14, 15] This mathematical formalism is now utilized in 2D-IR spectroscopy except the cross products of electric fields and spins have been traded for dot products and dipoles. The density matrix is central to the mathematical formalism used to describe complicated systems having many eigenstates. Application of density matrices for modeling nonlinear spectroscopy is described in depth by Mukamel, and more conceptually by Hamm and Zanni.[1, 16, 17] Before unpacking the theory governing 2D-IR it is useful to consider conceptually what can be observed with the technique.

Vibrational dynamics are directly tied to information about molecular structure and chemical processes. Vibrational dynamics refers to the time evolution of vibrational states where these states are usually described as eigenstates of the nuclear Hamiltonian. This is more complicated than the classical notion of them as masses in motion on springs. Vibrational dynamics are manifested as changes in the IR absorption or emission frequency of IR chromophores due to intramolecular and intermolecular effects. Dynamics can be due to stochastic structural fluctuations of molecules and phonon modes in condensed phase systems.[18, 19] These can be internal vibrations, coupling with neighboring molecules or functional groups, librations, and rotations. The most prominent of these interactions is

dipole-dipole coupling. This happens through space where the electric fields interact but there is also the case of mechanical through-bond coupling. This is where two vibrational modes far apart are affected by the atomic displacements in the atoms between them even if the modes are not resonant or directly coupled.[20, 21] This can be likened to linked mechanical springs and this type of vibrational mode coupling has been used to measure oligomer length.[21] Observation of IR frequency changes with system changes allow comparative measurements of vibrational dynamics or VET. System changes can be solvent composition, pH, molecular moieties, concentration, and heterogeneity induced by annealing or other effects.[22, 23]

Analysis of the vibrational dynamics of normal modes often requires an understanding of VET. Exchange of vibrational energy from one normal mode to another is described by quantum mechanical creation and annihilation operators: energy leaving one bond and going to another.[13, 24, 25] Alternatively, chemical exchange is a different type of vibrational dynamics that manifests in the same way as VET and is observed as discrete changes in frequency with time. These changes are associated with a chemical reaction such as complexation, structural changes, and bond formation or breaking.[9-12] Different vibrational dynamics or VET exhibited in 2D-IR spectra require unique analysis like centerline slope (CLS) decay correlating to the frequency-frequency correlation function (FFCF), nodal angle decay, cross peak intensity, or frequency dependent vibrational lifetime.[26-29] All of these phenomena and analysis will be seen in the later chapters of this thesis.

1.3 Conceptual 2D-IR View

Two-dimensional infrared spectroscopy is a three-pulse technique that resolves the dynamics of the sample system into another dimension. Pulses are controlled such that each 2D-IR spectrum occurs at a point in time which is the difference between the 3rd and 2nd pulses. This time is typically referred to as the "waiting time", or T_w. Data in each 2D-IR spectrum gives absorbance as a function of two frequency axes: a pump (ω_τ) axis and probe (ω_m) axis. The convention used herein is that the pump (ω_τ) axis is the x axis and probe (ω_m) axis is the y axis.

Two-dimensional peak shapes evolve with T_w. The frequency at which a chromophore is probed with respect to where it was pumped can be monitored as a function of T_w. We expect to probe a chromophore at T_w zero at the same frequency it was pumped, and this results in on-diagonal spectral intensity. For T_w's later than zero, environmental changes amounting to vibrational dynamics result in a chromophore red or blue shifting with time, due to the Stark effect.[1, 30, 31] If a frequency has red-shifted with T_w relative to its initial probe frequency this would result in intensity below the diagonal. If blue-shifting occurred after the initial probe frequency it would be observed as intensity above the diagonal. This results in apparent broadening along the probe axis. By the same mechanisms and dynamics, two chromophores pumped at different frequencies could be probed at the same frequency later in time. This results in apparent broadening along the pump axis. The net result is peak broadening along the antidiagonal direction due to changes in chromophore frequency. This is termed spectral diffusion.

Figure 3A illustrates what an early T_w 2D-IR spectrum could look like, and 3B illustrates what a later T_w might look like. Figure 3B illustrates the result of dynamics allowing every chromophore to sample every environment. 2D-IR spectra display a $|0\rangle \rightarrow |1\rangle$ vibrational transition and a $|1\rangle \rightarrow |2\rangle$ anharmonically-shifted transition. Interference of the absorbance of these two transitions results in the node between them. Their interference is a result of spectral overlap between the ground state bleach and excited state absorption. Analyzing peak shapes in 2D-IR spectra as a function of T_w is how they are used to relate system dynamics to physical processes.
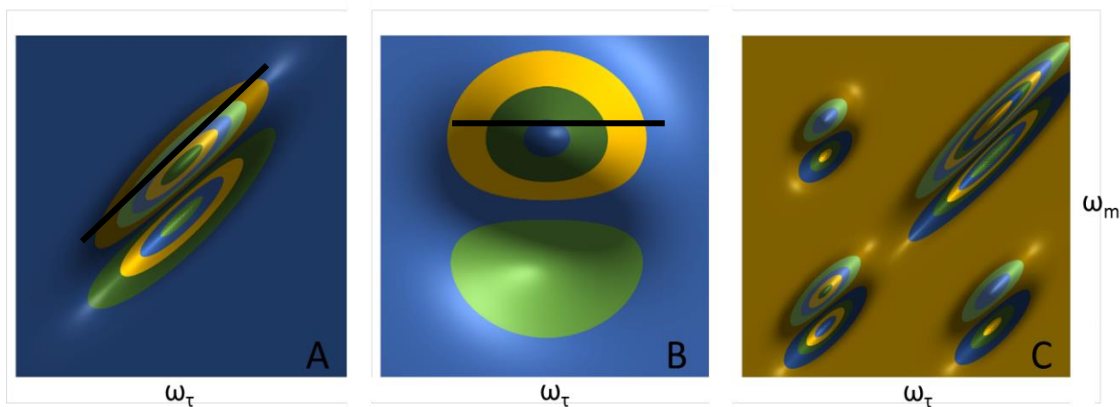
Figure 3: Idealized 2D-IR spectra with upper peaks positive going and lower peaks negative going. Units are signal intensity. Values are arbitrary. A corresponds to a spectrum at an early time or T_w. B corresponds to a spectra of the same sample at a later T_w. C corresponds to cross peaks that occur from frequency changes due to charge transfer, through space coupling, or mechanical coupling. The peak pairs are 0 to 1 and 1 to 2 transitions. The peaks have opposite signs. The negative absorbance of the ground state is referred to as bleach. This is due to decreased population of the ground state relative to a reference and is a consequence of multiple pulses. In pump-probe experiments the decay of ground state bleach and excited state absorption is monitored.

A useful metric for characterizing dynamics is the FFCF.[32] Correlation refers to the similarity of a property to itself at two different time points. Each 2D-IR spectrum is a signal that is a function of time (t) and two frequencies: $A(\omega_\tau, \omega_m, t)$. These spectra can be related to a general description of the correlation function with an arbitrary initial time point of zero:[33]

$$C(t) = \langle \omega_{\tau,m}(0) | \omega_{\tau,m}(t) \rangle \qquad \qquad \textit{(1)}$$

This frequency function $\omega_{\tau,m}(t)$ can be taken as a delta function of a fundamental frequency where the correlation is a weighted average. The signal function $(A(\omega_\tau, \omega_m, t))$ that is measured is directly related to the correlation function by its Fourier transform. Knowledge of the FFCF from the CLS decay allows calculation of all linear and nonlinear experimental observables, including any dynamics.[32] A centerline can be defined as the signal maxima along slices through the peak for each slice at a single pump frequency (overlaid black line in Figures 3A and 3B). This slope cannot be greater than one and decays to zero for complete spectral diffusion. The centerline slope change with time is proportional to the FFCF.

The time resolution of dynamics measured by 2D-IR is limited by the temporal width (100 fs) of the laser pulses used to make the measurement. A unique chemical environment will result in a unique IR frequency of a given chromophore. The resolution of eigenstates having distinct transition frequencies due to unique environments is limited by the spectral resolution of the detection system used to analyze the mixed vibrational echo signal. Within these limits 2D-IR can measure state specific vibrational dynamics, exchange phenomena, and their relationship. Exchange phenomena can be VET, CT, or chemical exchange. Ideally VET or CT measurements would appear as off diagonal peaks (Figure 3C). These are termed cross peaks. In the case of CT, they reflect the discrete changes in chromophore frequency arising from a change in oxidation state. The same peaks arise from VET due to mechanical coupling through bonds and through space coupling for proximal chromophores. Cross peaks can also arise from anharmonic

coupling but this is easily differentiated based on signal decay as discussed in Chapter 3. Observing complexation, CT, hydrogen bond reorganization, or other exchange effects using 2D-IR goes well beyond the time scales of the analogous capability of 2D-NMR (microseconds) which observes atom proximity and through bond coupling in addition to chemical environment.

Multidimensional NMR is often quoted as being somewhat analogous to 2D-IR due to the origin of the theories governing both spectroscopies.[1, 3, 16, 34] Rigorous theory for both rests in the time dependent perturbation of the density matrix. [1,16]. In 2D-IR the expectation value of this operator is the time dependent macroscopic polarization. Macroscopic polarization is a collection of electric dipoles moving in a coherent fashion. The square modulus of the oscillating field emitted by these oscillators is what is *actually* measured as light intensity. Absorption of light is the destructive interference of an input field and a field emitted by an oscillating macroscopic polarization. The oscillation of dipoles is described by the sinusoidal variation of the density matrix coefficients and corresponds to the frequencies detected. Below is a brief outline of the quantum mechanical theory underlying 2D-IR with the inclusion of electric fields (laser pulses) used to observe what this theory describes.

1.4 2D-IR Theory; Schrödinger

To arrive at the formalism to describe an experiment, the simplest place to start is the time dependent Schrödinger equation:

$$-i\hbar \frac{\partial}{\partial t}|\Psi\rangle = \hat{H}|\Psi\rangle \qquad (2)$$

Here $\hat{H}$ is the entire Hamiltonian describing the unperturbed time independent eigenstates as well as any perturbations that are time dependent.

$$\hat{H} = \hat{H}_o + \hat{H}(t) \tag{3}$$

One typical approach is to expand the wavefunction, $|\Psi(t)\rangle$, in a time-independent eigenstate basis of $\hat{H}_o$ with time-dependent coefficients: $|\Psi\rangle = \sum_n c_n(t)e^{-iE_nt/\hbar}|n\rangle$. The first term in the Hamiltonian ($\hat{H}_o$) will be ignored as it simply scales the energy of the system without time dependence and is not directly observed in 2D-IR measurements. The remaining term in the Hamiltonian includes time-dependent perturbation. Specific to 2D-IR, the perturbation is an electric field. This field acts on an electric dipole to put it into a coherence or superposition of states. Then the time dependent coefficients describing the populations of states and coherences can be obtained by applying the Schrödinger equation:

$$i\hbar \frac{\partial}{\partial t}|\Psi\rangle = \hat{H}(t)|\Psi\rangle = -\hat{\mu}\vec{E}(t)|\Psi\rangle \tag{4}$$

$$i\hbar \frac{\partial}{\partial t}\sum_n c_n(t)e^{-iE_nt/\hbar}|n\rangle = \hat{H}(t)\sum_n c_n(t)e^{-\frac{iE_nt}{\hbar}}|n\rangle = \tag{5}$$

$$-\hat{\mu}\vec{E}(t)\sum_n c_n(t)e^{-iE_nt/\hbar}|n\rangle$$

Where $\hat{\mu}$ is the dipole operator ($\frac{d\hat{\mu}}{dx}\hat{x}$) and $\vec{E}(t)$ is the time dependent electric field. With the wavefunction decomposed into an orthonormal eigenstate basis, left multiplying with a specific eigenvector ($\langle m|$) yields:

$$\frac{\partial}{\partial t} c_m \delta_{mn} = \frac{\partial}{\partial t} c_m \langle m|n \rangle e^{-i(E_n - E_m)t/\hbar} \tag{6}$$

$$= -\frac{i}{\hbar} \langle m|\widehat{H} \sum_n c_n(t) e^{-i(E_n - E_m)t/\hbar} |n \rangle$$

$$= -\frac{i}{\hbar} \sum_n c_n(t) e^{-i(E_n - E_m)t/\hbar} \langle m| - \hat{\mu}\vec{E}(t)|n \rangle$$

$$= \frac{i}{\hbar} \sum_n c_n(t) e^{-i(E_n - E_m)t/\hbar} \vec{E}(t) \langle m|\hat{\mu}|n \rangle$$

Left multiplying by $\langle m|$ results in the survival of only the mth coefficient's time derivative because of the orthogonality of the eigenstate basis. Already there is an assumption that the laser field does not perturb the basis eigenstates. Even if some perturbation of the eigenstates occurred, it can be corrected by a higher order perturbative expansion.

The above equations also highlight a fundamental quantity; the transition dipole ($\langle m|\hat{\mu}|n \rangle = \mu_{mn}$). The eigenstates ($\langle m|, |n \rangle$) acted on by the dipole operator ($\hat{\mu}$) compose the transition dipole ($\hat{\mu}_{mn}$). Signal is proportional to the probability and magnitude of transitions between two eigenstates. This probability is described through the transition dipole as the overlap of two eigenstates. The derivative of the dipole operator ($\frac{d\hat{\mu}}{dx}$) describes the magnitude of dipole change with a transition. The dipole vector direction ($\hat{x}$) is the normal mode coordinate that determines the extent of interaction with the electric field vector. Typically, linearly polarized light is used and the projection of the dipole vectors onto the electric field vector defines the magnitude of interaction. Without the dipole operator the inner product between two vibrational eigenstates would be zero and there would be no transition, no coherence, and hence no time dependence of the state coefficients to correlate to time dependent properties of interest. All the time dependence of interest is contained in the coefficients of the eigenstates ($c_n(t)$).

Integration of equation 6 gives the time dependent coefficients of the wavefunction. This task is not trivial when considering complicated laser pulses. However, some simplifying assumptions give qualitative results similar to what can be derived using more complex methods.[16, 35] Treating the laser pulse as a delta function, assuming a two level system, ignoring spatial constants, letting $c_o = 1$, $\frac{dc_o}{dt} = 0$, because $c_o \gg c_1$ for all times; it can quickly be shown that:

$$\frac{dc_1}{dt} = \frac{i}{\hbar} e^{-i\omega t} \tag{7}$$

$$\omega = \frac{E_1 - E_o}{\hbar} \tag{8}$$

This is the simplest way to show that the time dependence of the coefficients is sinusoidal in nature. Measurement of these coherent states relies on the emission of an oscillating electric field which can be observed directly (homodyne detection) or interfered with another electric field (heterodyne detection). The field emitted from a sample is the result of a coherent oscillation of many oscillators giving rise to an oscillating macroscopic polarization. The macroscopic polarization is the expectation value of the transition dipole:

$$P(t) = \langle \mu \rangle = \langle \Psi | \hat{\mu} | \Psi \rangle \tag{9}$$

Again, the wavefunction can be expanded as necessary to describe the system of interest:

$$\langle \mu \rangle = \sum_m c_m{}^*(t)\, e^{\frac{iE_m t}{\hbar}} \langle m | \hat{\mu} | \sum_n c_n(t) e^{-\frac{iE_n t}{\hbar}} | n \rangle = \tag{10}$$

$$\sum_{mn} c_m{}^*(t) c_n(t) e^{-\frac{iE_n t}{\hbar}} e^{\frac{iE_m t}{\hbar}} \langle m | \hat{\mu} | n \rangle$$

The terms in the sum where m does not equal n are referred to as coherences. These describe the transition between states and carry phase information.[1, 16, 36]

The magnitude of the transition dipole, the energy difference between the two states, and the resonance condition of the electric field of the perturbative laser pulse with that energy difference affect the macroscopic polarization. If every molecule in the sample were exactly the same, the emitted field due to polarization would scale as the number of molecules with a frequency width limited by the uncertainty principle ($\Delta E \Delta t = \frac{\hbar}{2}$). Though simplified or unphysical the preceding equations give some level of prediction. The preceding equations describing an ideal case give some expectation as to what the polarization should be under more sophisticated treatment.[1, 15-17] To describe a physical system in which all molecules are not identical (a mixed state) the density matrix is introduced.

1.5 2D-IR Theory: The Density Matrix

The density matrix is invoked to describe a probabilistic distribution of states and is also referred to as the statistical operator or density operator.[37] The density matrix operator is composed of a basis of eigenstates with time dependent coefficients ($\hat{\rho}(t) = \sum_{mn} c_m^*(t) c_n(t) |\text{n}\rangle\langle\text{m}|$). The density matrix operator contains a projection operator of the eigenstate basis ($|n\rangle\langle m|$) . The compact density matrix is as follows:

$$|\Psi(t)\rangle\langle\Psi(t)| = \sum c_n(t)|n\rangle \sum c_m^*(t)\langle m| = \cdots \qquad (11)$$

$$\cdots \sum_{mn} c_m^*(t)c_n(t)|n\rangle\langle m| = \sum_{mn} \rho_{mn}|n\rangle\langle m| = \hat{\rho}(t)$$

This operator is a square matrix and its diagonal elements $(|c_n(t)|^2)$ are proportional to the relative expectation values of the eigenstate populations. Off-diagonal elements $(c_m(t)^* c_n(t))$ describe the coherences with a time-dependent component. Each coherence represents a pathway between states where different pathways are what give rise to phase differences even when two oscillators occupy the same states at the same times.[1] This means the different ways that oscillators change states is observable.

Populations do not emit measurable fields in and of themselves but the number of oscillators in a population changing with time can be observed. Oscillators spontaneously decaying out of an excited state to the ground state is called population decay. Population decay is one source of dephasing of the polarization. Dephasing refers to the loss of phase relationships among a collection of oscillators due to slight changes in frequency and amplitude of individual oscillators. Fluctuations in the environment also induce dephasing. Dephasing is observed as spectral diffusion or the decay of correlation. Theoretically all the information on populations and phase relationships can be extracted using the density matrix operator.

The density matrix (ρ) is explicitly a function of time (t) because the coefficients $c_m(t)^*$ and $c_n(t)$ are time dependent. The density matrix is conveniently put to use through the Liouville-Von Neumann equation:[1, 16, 17, 35, 38]

$$\frac{\partial \hat{\rho}}{\partial t} = -\frac{i}{\hbar}[\hat{H}, \hat{\rho}] \qquad (12)$$

Notice that acting with the operator $\hat{\rho}(t)$ on any system state $|\Psi\rangle$ would project the system state onto the m-n basis. Exact solutions for either the mixed system state or in some limit the pure eigenstates are not known but the Liouville-Von Neumann equation can be used to extract the time dependence of the coefficients. This time dependence is the main component describing system evolution. So again where $\hat{H} = -\vec{E}(t)\hat{\mu}$ one obtains:

$$\frac{\partial \hat{\rho}}{\partial t} = \vec{E}\frac{i}{\hbar}[\hat{\mu}, \hat{\rho}] \qquad (13)$$

If this system is in some initial state and is perturbed by a laser pulse, the system evolves after the laser pulse just as it did in the simple case above (Equation 7). It is commonly stated that the expectation value of an operator is the trace of its product with the density matrix:

$$P(t) = \langle \hat{\mu} \rangle = Trace[\hat{\mu}\hat{\rho}] \equiv \langle \hat{\mu}\hat{\rho} \rangle \qquad (14)$$

It is clear from equation 14 that the on-diagonal elements of the density matrix, through ket-bra projections, are same state outer products and thus give the coefficients for eigenstate contributions to the system state or relative eigenstate populations. As previously stated though, it is the coherences or oscillations between states that carry the signal and information that 2D-IR makes accessible.

1.6 2D-IR Theory: The Evolution Operator and Electric Fields

The last operator to introduce to fully describe the 2D-IR signal is the time evolution operator, which will be combined with the time derivative of $\hat{\rho}$.[35] The time evolution operator arises from the fact that a state at some point in time must be accessible from some former state. This fact and the definition of the Hamiltonian result in:

$$\hat{U}(t, t_o) = e^{-i\hat{H}_o(t-t_o)} \tag{15}$$

To evolve the density matrix in time one acts on the ket with $\hat{U}$ and on the bra with the complex conjugate $\hat{U}^*$. It might be intuitive that any number of time steps between t and t_o can be taken. To get the value of $\hat{\rho}$ at a given time, one simply integrates its commutator with the Hamiltonian. The general result is:

$$\hat{\rho}_o^{(n)} = -\left(-\frac{i}{\hbar}\right)^n \int_{t_o}^t d\tau_n \int_{t_o}^{\tau_n} d\tau_{n-1} \dots \tag{16}$$

$$\int_{t_o}^{\tau_2} d\tau_1 e^{-i\hat{H}_o(t-t_o)} \left[\hat{\mu}(\tau_n) \dots [\hat{\mu}(\tau_1)[\hat{\mu}(t_o), \rho(t_o)]]\right] e^{i\hat{H}_o(t-t_o)}$$

One final step is to include the electric field perturbation in this function. The field has a finite width and passes through the sample so it will be convolved with the polarization. This also might be intuitive because the sample begins to respond to the laser pulse as it enters the sample, which continues to respond and emit signal as the pulse passes through it. If the sample were oscillating prior to the laser pulse entering it, the same would be true. Were the laser pulse a δ function, the convolution would simply return the expectation value of the transition dipole perturbed by the field. This is a common simplifying assumption referred to as the impulsive limit.

$$\hat{\rho}^{(n)} \tag{17}$$

$$= -\left(-\frac{i}{\hbar}\right)^n \int_{t_o}^t d\tau_n \int_{t_o}^{\tau_n} d\tau_{n-1} \dots \int_{t_o}^{\tau_2} d\tau_1 \vec{E}(t-\tau_n)\vec{E}(t-\tau_n-\tau_{n-1})\vec{E}(t$$

$$-\tau_1)e^{-i\hat{H}_o(t-t_o)} \left[\hat{\mu}(\tau_n) \dots [\hat{\mu}(\tau_1)[\hat{\mu}(t_o), \rho(t_o)]]\right] e^{i\hat{H}_o(t-t_o)}$$

In equation 17 each integral propagates the system to a time point after the initial time point t_o and convolves an electric field occurring at time τ_n with the dipole. The relative populations of the eigenstates dictate the magnitude of oscillation between these states and thus the macroscopic polarization, which is the expectation value of the density matrix operator, and is the following:

$$P(t) = \langle \hat{\rho}^{(n)} \rangle = -\left(-\frac{i}{\hbar}\right)^n \int_{t_o}^{t} d\tau_n \int_{t_o}^{\tau_n} d\tau_{n-1} \ldots \int_{t_o}^{\tau_2} d\tau_1 \vec{E}(t - \tau_n)\vec{E}(-\tau_n \tag{18}$$

$$- \tau_{n-1})\vec{E}(t - \tau_1)e^{-i\hat{H}_o(t-t_o)}R^{(n)}(t)e^{i\hat{H}_o(t-t_o)}$$

$R^{(n)}(t)$ is defined as the following:

$$R^{(n)}(t) = \langle \hat{\mu}(\tau_n) \ldots [\hat{\mu}(\tau_1)[\hat{\mu}(t_o), \rho(t_o)]] \rangle \tag{19}$$

The nth order response functions ($R^{(n)}$) contain all the quantum mechanical information about the system state. Laser pulses can be controlled and kept relatively constant over the course of an experiment so the variation in macroscopic polarization with changes in pulse timing is a measurement of the actual response function. Thus, the response functions are the connection between measurement, the density matrix, the probability of configurations,
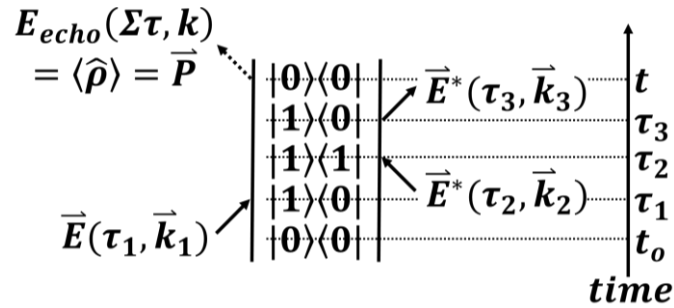
Figure 4: This is a common depiction of a Feynman diagram. The vertical axis represents time. The left eigenstate vectors are kets and interact with the real component of the electric field while the right are bras and interact with the imaginary component. The many complex arguments of the equations describing this picture result in many permutations.

and ultimately the quantum states. Feynman diagrams (Figure 4) are graphical representations of the interactions between light and the system described by the response

functions. In 2D-IR there are three input pulses and one output pulse so this would give rise to $R^{(3)}(t)$:

$$R^3(\tau_3, \tau_2, \tau_1) = \langle \mu(\tau_3) \left[\mu(\tau_2) [\mu(\tau_1) [\mu(0), \rho(-\infty)]] \right] \rangle \qquad (20)$$

In equation 20, τ_3 refers to the arrival time of pulse 3 in Figure 4. Of the multiple terms resulting from the commutator relationship, there are 6 that survive when applying the rotating wave approximation. The rotating wave approximation ignores terms that are highly oscillatory and physically means eliminating terms that involve de-excitation of the ground state to produce an excited state.[16]

The electric field of the laser pulse has a phase (ϕ) and direction ($\vec{k}$) as well as real and imaginary components. The wave vector $\vec{k}$ is defined as follows where $\hat{z}$ is the direction of laser beam propagation and λ is wavelength:
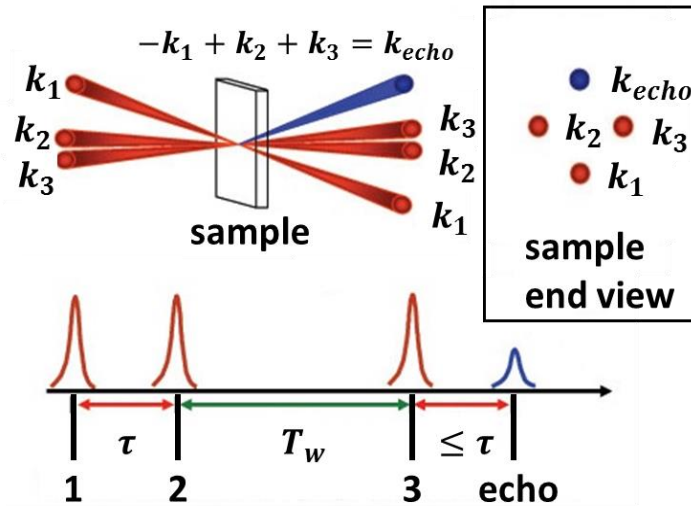
Figure 5: This figure depicts three light pulses entering the sample with a unique direction described the vector k. Spatial separation of these pulses allows isolation of the echo signal. The timing of the pulses to obtain the pump axis of a 2D-IR spectra is depicted as well. Tw is the time during which dynamics induce spectral diffusion or cross peaks.

$$\vec{k} = \frac{2\pi}{\lambda}\hat{z} \tag{21}$$

The real and imaginary components act on the ket and bra components of the density matrix respectively. To understand how data are collected it is informative to view the plane wave solutions of Maxwell's equations that describe the oscillating electric field component of light:[39]

$$\widetilde{E_1}(t) = Ee^{i(\vec{k}_1 \cdot \vec{r} - \omega_1 t + \phi)} \tag{22}$$

Here $\vec{r}$ is the vector following the path to the point in space where one would look for signal. For multiple pulses with unique phase and direction, equations 21-23 show that there is a direction of maximum signal depicted in figure 5:[32]

$$\widetilde{E_1}(t)\widetilde{E_2}(t)\widetilde{E_3}(t) = Ee^{i(\vec{k}_1 \cdot \vec{r} - \omega_1 t + \phi_1)}Ee^{i(\vec{k}_2 \cdot \vec{r} - \omega_2 t + \phi_2)}Ee^{i(\vec{k}_3 \cdot \vec{r} - \omega_3 t + \phi_3)} \tag{23}$$

$$\tilde{E}_{max} \Longrightarrow \vec{r} = \pm\vec{k}_1 \pm \vec{k}_2 \pm \vec{k}_3 \tag{24}$$

This applies to the emitted polarization from the sample as well. This occurs because the polarization in the sample is induced by the incoming coherent light.

One final aside is that in the case of ensembles the wavefunction $(|\Psi^s\rangle)$ would correspond to unique sets of coefficients (c_n^s) and the complete system would be described by a weighted sum over s with probably coefficients (p_s). This would also correspond to a weighted sum of density matrices. This does not change any of the concepts. Limitations to the information that can be gained about the microscopic system are rooted in the fact that systems are probabilistic and what is observed is a time and frequency resolution-

limited ensemble measurement.   Higher order spectroscopies may yield further information.[40]

1.7 Experimental Setup and Data Collection

The experimental setup relies on a variety of laser physics beyond this discussion, but some salient features pertain to the measurement. Standard descriptions of light generation for the experimental setup in the Massari lab will also be mentioned. Much of the description is given in references for this thesis.[22, 41] A block diagram of the laser setup is shown in figure 7 of Chapter 2 excluding laser components for IR pulse generation, however generation of IR pulses will be briefly described.

First, light is produced by pumping a titanium sapphire (Ti:Sapph) oscillator with a continuous wave (CW) neodymium vanadate laser. This generates mode-locked pulses at 800 nm with a FWHM of 45 nm. Mode-locked means that constructive interference of multiple wavelengths with a fixed phase relationship, occurs periodically and this is what generates pulses. Generated pulses are stretched in time and then used to seed a regeneratively amplified Ti:Sapph laser pumped by a Q-switched neodymium yttrium lithium fluoride (Nd:YLF) laser. After recompression of the amplified pulses, the output pulses have a temporal profile of 40 fs, a bandwidth of 30 nm, and a repetition rate of 1000 Hz. This light is then used to pump an optical parametric amplifier (OPA). This OPA uses a β-barium borate (BBO) crystal to generate a near infrared signal pulse and an idler pulse. These pulses are then mixed in a silver gallium sulfide ($AgGaS_2$) crystal where difference frequency mixing generates tunable infrared pulses approximately 90 fs temporally with a frequency FWHM of 200 cm^{-1}.[22]

To obtain multiple light pulses an incoming pulse is split using a zinc selenide (ZnSe) beam splitter. Beam refers to the path of light and is often used interchangeably with pulse. Two beam splitters are used to create four beams: 1, 2, 3, and local oscillator (LO). Pulses 1, 2, and 3 pass through identical amounts of material on their path to the sample. The LO does not pass through the sample, which is usually mounted between calcium fluoride (CaF$_2$) windows. This difference in the amount of optics that a pulse passes through causes slightly different group velocity dispersion (GVD, colloquially called chirp) in the LO pulse compared to pulses 1, 2, and 3. Chirp is the delay in time of blue wavelengths relative to red wavelengths when passing through a medium with a frequency dependent refractive index. This GVD difference results in a frequency dependent phase error between the blue and red frequencies in the signal and LO that requires a phase factor (Q) correction to the Fourier Transform of the tau time step signal. It is a multiplicative factor in the exponential used in digital Fourier transform (DFFT or FFT).

The delay stages that are moved to create the tau signal interference have some error associated with their movement. The error is proportional to the movement. This happens for each 2D-IR spectrum collected necessitating additional phase factors, Δ_{12} and Δ_{3LO}, that account for the pulse timing error between pulses 1 and2 and the error between pulse 3and the LO pulse, respectively. "Phasing" refers to the process by which 2D-IR data are adjusted by these phase parameters so that the projection of a spectrum on the ω_m axis best matches the pump-probe.[28] This is called the pump-probe projection theorem and it requires that pump-probe data be collected for each corresponding T$_w$ time point of a set of 2D-IR spectra.[28] Phasing can have a variety of effects on peak shapes and thus what can

be interpreted from the data. Chapter 6 highlights some of the challenges associated with phasing. For measurements of dynamics it has been shown that peak shapes changed by apodization do not affect the CLS decay, which is related to the FFCF.[32]

In generating 2D-IR signal then light pulses are split into four beams. Pulses 1, 2, and 3 are of equal intensity but the LO beam is approximately 0.01 % of the incoming beam power and is heterodyned with the echo signal that is generated by mixing the three remaining equal intensity beams in the sample. The beams are arranged in the BOXCARS geometry (Figure 5) where the echo is generated in the phase matched direction as previously discussed.[42] Heterodyne detection of the echo signal gives phase information of the echo (detected signal $\propto \vec{E}_{echo}\vec{E}_{LO}$) as opposed to detecting echo intensity ($\vec{E}_{echo}^2$).[16] It also strengthens the detected signal as $\vec{E}_{LO}$ has a larger amplitude than $\vec{E}_{echo}$. Heterodyne detection allows measurement of weaker oscillators because the heterodyned signal scales as μ^4 as opposed to homodyne detected signal, which scales as μ^8. Heterodyne detected signal also decays half as quickly as homodyne detected signal allowing dynamics to be measured over a longer range of time.

Signal detection is performed using a mercury cadmium telluride (MCT) detector cooled with liquid nitrogen. In our lab there are three grating options within the 0.34 m monochromator that directs light onto the MCT detector.[41] With a 75 line/mm grating the resolution is approximately 2 cm^{-1}. There are 150 line and 300 line gratings for higher spectral resolution as well. Each pixel in the MCT detector is used to record a time-domain interference pattern by scanning the time between pulses 1 and 2, called τ. This time-dependent interference signal is Fourier transformed to obtain the pump axis frequency (ω_τ). Scanning the τ time is accomplished by moving a delay stage in discrete 5 fs delay

steps (roughly 1.5 microns). The error for this movement is small and the chirp phasing factors are constant over a given experiment. The beam pairs (1 & 2, 3 & LO) can also be moved relative to each other for improved signal as described in further detail in Chapter 2. The MCT detector performs an optical Fourier transform using a monochromator which is the y axis called ω_m.

The FFCF is a common tool for 2D-IR data analysis but is of limited use for systems with large static inhomogeneities such as the nanoparticle films discussed in the last Chapters 4 and 6. Phasing uncertainty combined with large static disorder can be a problem when looking for small differences in spectra collected from comparative experiments. This problem was circumvented preliminarily for the TiO_2 research as these phase factors were fixed by experimental means for two spectra to be compared as discussed in Appendix A section 5. This worked well to show that CT was not being measured in the DSSC system discussed in Chapter 6. If a system is reasonably conductive then charge diffusion as well as field driven CT would be convoluted with any other anharmonic coupling or VET. All these processes would appear the same in a 2D-IR spectrum. Thus, each time point in the tau scan must be collected with and without a perturbation (voltage on and off respectively).

With a qualitative grasp of formal 2D-IR theory and experimental details understood a 2D-IR experiment and data analysis can be reasonably performed. In every experiment performed there are unforeseen challenges. Some are exciting experimental results that provide new information about the systems under study. Others are a hinderance to obtaining usable data. Time and again when measuring samples, the challenge of scatter was a major obstacle. After two years of complaining about this, we

had an idea of how to deal with this. The resultant solution is outlined in the next chapter. The experiments that follow in this thesis as well as other published works would not have been possible without "fibrillation".

Chapter 2 A Simple Fully-Reflective Method of Scatter Reduction in 2D-IR Spectroscopy

Reproduced in part with permission from:

"Simple fully reflective method of scatter reduction in 2D-IR spectroscopy," Ivan C. Spector, Courtney M. Olson, Christopher J. Huber, Aaron M. Massari; *Optics Letters,* **2015**, 40(8), 1850-1852

2.1 Introduction

A fully-reflective 2D-IR setup is described in this chapter that enables efficient cancelation of scattered light from multiple pulses in the phase matched direction. The LO pulse and the pulse that stimulates the vibrational echo signal are synchronously modulated (or fibrillated) in time maintaining their phase relationships with the echo wavepacket. The modification is cost-effective and can be easily implemented on existing 2D-IR instruments, and it avoids the addition of dispersive elements into the beam paths. The fibrillation results in a decrease of waiting time resolution of only tens of femtoseconds and has no impact on the spectral lineshape, making it a general improvement for 2D-IR spectrometers even for weakly- or non-scattering samples.

As previously mentioned 2D-IR has emerged as an important method for measuring ultrafast dynamics of model compounds [32, 41,43,44], neat liquids [45-47], and biomacromolecules [48-50]. With greater confidence in data interpretation and ever improving instrumental tools at their disposal, the 2D-IR community has begun to study more advanced materials, including solid state films and nanoporous glasses [22, 51-54]. A common challenge that arises

with these complex heterogeneous samples is extracting signal in the presence of significant scatter from multiple beams in the phase matched direction.

As described in Chapter 1, in a 2D-IR measurement, three ultrafast IR pulses are overlapped in the sample. The first pulse prepares a macroscopic polarization that evolves over the τ period until the second pulse transfers the surviving coherences into population states. After a second time period, T_w, a third pulse transfers some of the surviving populations back to their phase conjugate coherences. These can rephase to regenerate a macroscopic polarization in the sample and emit a vibrational echo pulse in a phase matched direction.[1, 16] The dynamical evolution of the vibrational oscillators during the τ and T_w periods is encoded in the phase and amplitude of the echo wavepacket, and this information is extracted by interfering it with the LO reference pulse. As discussed, frequency resolving the signal and LO pulses with a monochromator and Fourier transforming the data along the τ dimension, a 2D-IR spectrum is produced.[1, 16]

2.2 Scatter and Phase Relationship

For a single 2D-IR spectrum, the LO timing is fixed and is generally time coincident with pulse 3. The T_w time period between the second and third pulses is also fixed while the τ period is scanned in time steps that move the echo wavepacket by a fraction of a period of the IR light. Positive τ values are obtained by scanning beam 1 and negative values are obtained by scanning beam 2, hence both of these pulses move in time over the course of collecting a single absorptive 2D-IR spectrum.[55] Moving pulse 1 to arrive earlier at the sample (positive τ scan) emits the echo wavepacket later in time causing it to alternately interfere constructively and destructively with the stationary LO reference field

on the detector. This is the desired interference that produces the temporal interferogram that is Fourier transformed to produce the 2D-IR spectrum.

Introducing scatter from each of the three beams at the sample sends additional "pulses" in the phase matched direction. Even though they are not time coincident, spectrally resolving these scattered pulses changes their temporal duration by one or two orders of magnitude so that they are all overlapping with the LO and signal in time and space at the detector element(s). This leads to additional interferences between each scattered pump beam and the LO, as well as between the scattered beams and the echo signal. The integrated intensity is the squared modulus of the sum of all electric fields reaching the detector, which includes the desired and undesired interferences between all fields.

$$I \propto \left| E_{LO} + E_{signal} + E_{1,scatter} + E_{2,scatter} + E_{3,scatter} \right|^2 \qquad (25)$$

This produces 25 terms, some of which can be eliminated by synchronously chopping one beam (as we do with pulse 2 in Figure 2 or beam 1 in Figure 7). The remaining 16 terms have either an E_{signal} or $E_{2,scatter}$ term in them and are not removed by chopping. During a positive τ scan, pulses 2 and 3 are stationary relative to each other and the LO. Scatter from pulse 3 will interfere with the LO at the detector, but the two pulses are time coincident and nearly identical in spectrum and phase. Hence, beam 3 scatter simply augments the LO in a τ-independent way. Pulse 2 scatter is not time coincident with the LO (or pulse 3 scatter) at the detector but is offset by T_w, producing spectral interference fringes in the LO. There are no oscillations in the integrated signal intensity due to pulse

2 or pulse 3 scatter as τ is scanned in the positive direction, but the scatter from pulse 2 can have insidious amplitude effects by shaping the LO reference pulse differently at each T_w. For this positive τ scan, pulse 1 is moving towards the sample, and its scatter is arriving earlier at the detector and interfering at each frequency within the LO field spectrum. This leads to an intense temporal interferogram that Fourier transforms to produce the laser spectrum as a bright ridge down the diagonal of the 2D-IR spectrum. Pulse 1 scatter and the echo pulse are moving in opposing directions and hence interfere at twice the carrier frequency. This interference is ideally filtered out during the Fourier transform of the time-domain data. For negative values of τ, pulse 2 is scanned to earlier arrival times and the role of scatter from these first two pulses is reversed from the description above.
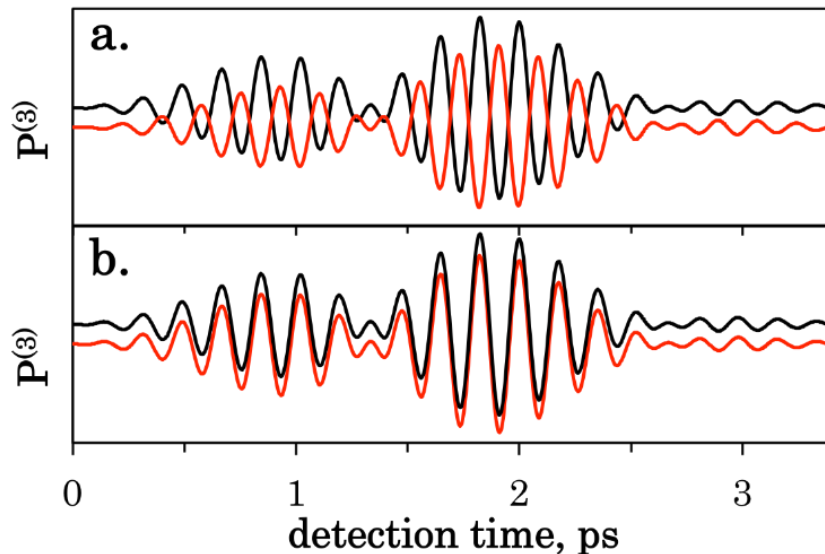
Figure 6: Real part of the third-order polarization as a function of the detection time, t3, calculated from the rephasing diagrams using a single exponential frequency-frequency correlation function [1]. The transition frequency is lowered here to 200 cm-1 so that the phase of the oscillations is evident. In both frames the black trace shows the P(3) at τ = 2 ps and Tw = 3 ps. The red traces show the result of increasing a) τ or b) Tw by the temporal equivalent of a half cycle of light. Black and red traces have been vertically offset for clarity.

For homodyne detected vibrational echo data, a simple solution to the scattering issue was demonstrated by modulating the arrival of one pulse at the sample by a fraction of a wavelength, termed "fibrillation".[56] In that case, the first beam in the pulse sequence

was fibrillated, causing the echo wavepacket to be fibrillated as well. Figure 6a demonstrates how the third-order polarization (echo wavepacket) advances in time when the τ period is increased by the temporal equivalent of a half-wavelength. Since the signal field was not heterodyne detected with a reference field, after some averaging, scatter from the first pulse would cancel scatter from the other two, leaving only the averaged signal intensity.[56] This approach no longer works with heterodyne detected 2D-IR signals where the interference between the LO and the signal produces the spectrum. Fibrillation of the first or second pulses changes the τ period, which modulates the emission time after pulse 3, t_3, of the echo signal (Figure 6a) while the LO reference field is fixed. This causes cancelation of all signal, rather than just the scatter. To achieve the same scatter cancelation, one needs to maintain the phase relationship between the third pulse (and its scatter), the LO, and the signal fields.

Response function formalism dictates that the echo signal pulse is phase locked to the third interaction pulse.[1] This means that fibrillation of the third pulse, and therefore modulating the T_w period, will maintain the phase relationship between these two fields. Figure 6b demonstrates how the calculated echo emission from the rephasing third-order polarization changes with temporally delaying pulse 3. It is clear that fibrillating the third pulse maintains the phase of the echo wavepacket. A nearly imperceptible change in the echo amplitude is present, as would be expected for increasing the T_w period. However, a typical 2D-IR setup uses a LO pulse that follows a different path to the detector. In these

cases, fibrillating the third pulse while keeping the LO stationary will still lead to total signal cancelation.

2.3 Experimental Results With Scatter Reduction

Here we demonstrate a simple experimental setup that can utilize the fibrillation approach to scatter cancelation without eliminating the signal-LO interference term. This concept has been reported previously by Bloem and coworkers by the insertion of a wobbling Brewster window and a photoelastic modulator.[57] The current design improves on this approach in that it is a completely reflective solution, which is important for maintaining ultrafast pulse durations. Although the group velocity dispersion introduced by transmissive optics can be partially compensated by adding other materials to the beam path, third order dispersion is difficult to eliminate, making a reflective approach preferable.[58] The same effect has also been achieved by completely flipping the relative phase of the pump and probe pulses using a mid-IR pulse shaper, but this can be cost prohibitive.[59] The current design is simple and cost-effective, and can be easily implemented on an existing 2D-IR instrument with commercially available parts.

Figure 7 shows the basic experimental approach. The important element is that the LO and beam 3 traverse a delay stage that is fibrillated. Fibrillation is achieved with a piezoelectric actuator (PZA) (Thorlabs PE4 with MDT694A controller) driven by a triangle-wave waveform generated at approximately 17 Hz. Before the 2D-IR experiment, a distance (delay time) versus voltage calibration curve was constructed by applying a
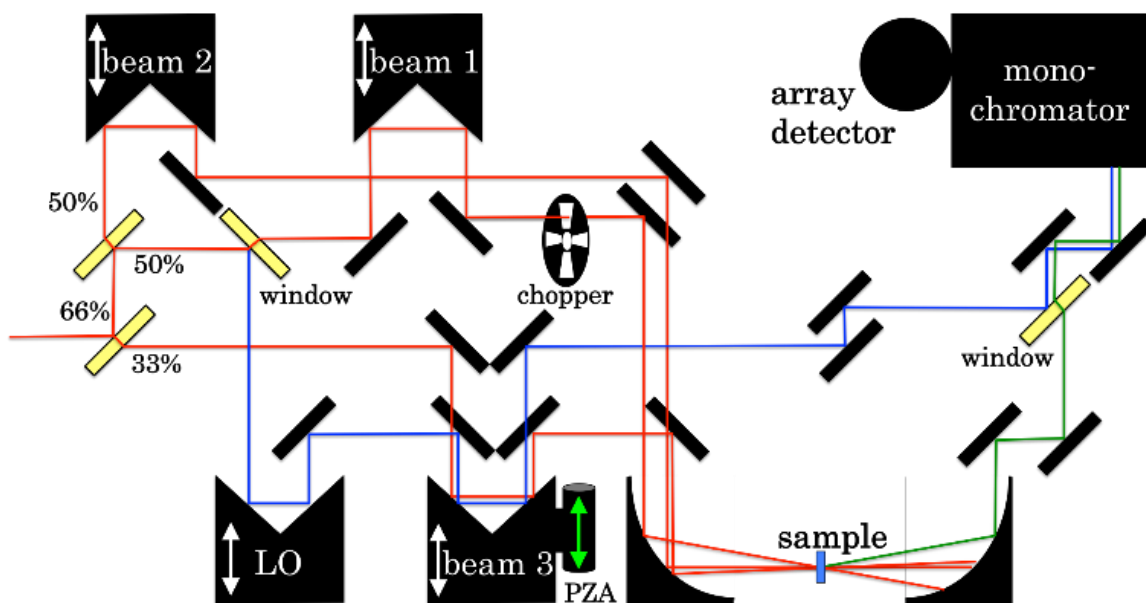
Figure 7: Schematic of the experimental 2D-IR setup. Red lines are pump beams, blue is the LO, and green is the echo signal path. Key to this work is that the LO and beam 3 traverse the same delay stage that is fibrillated by the PZA (green arrow).

range of DC voltages to the PZA and recording the two-pulse autocorrelation of pulse 3 with pulse 2 in a type-I $AgGaS_2$ doubling crystal. During the 2D-IR experiment, the amplitude of the PZA was adjusted to move the delay stage position by approximately one IR wavelength at the center of the laser spectrum. The precise frequency of the generated waveform is not crucial but should be selected to avoid even division of the pulse repetition rate, while providing enough oscillations of the beam path length to give effective scatter cancelation after averaging. As shown in Figure 7, since both the LO and beam 3 are directed into the fibrillated delay stage these pulses remain in phase with each other and
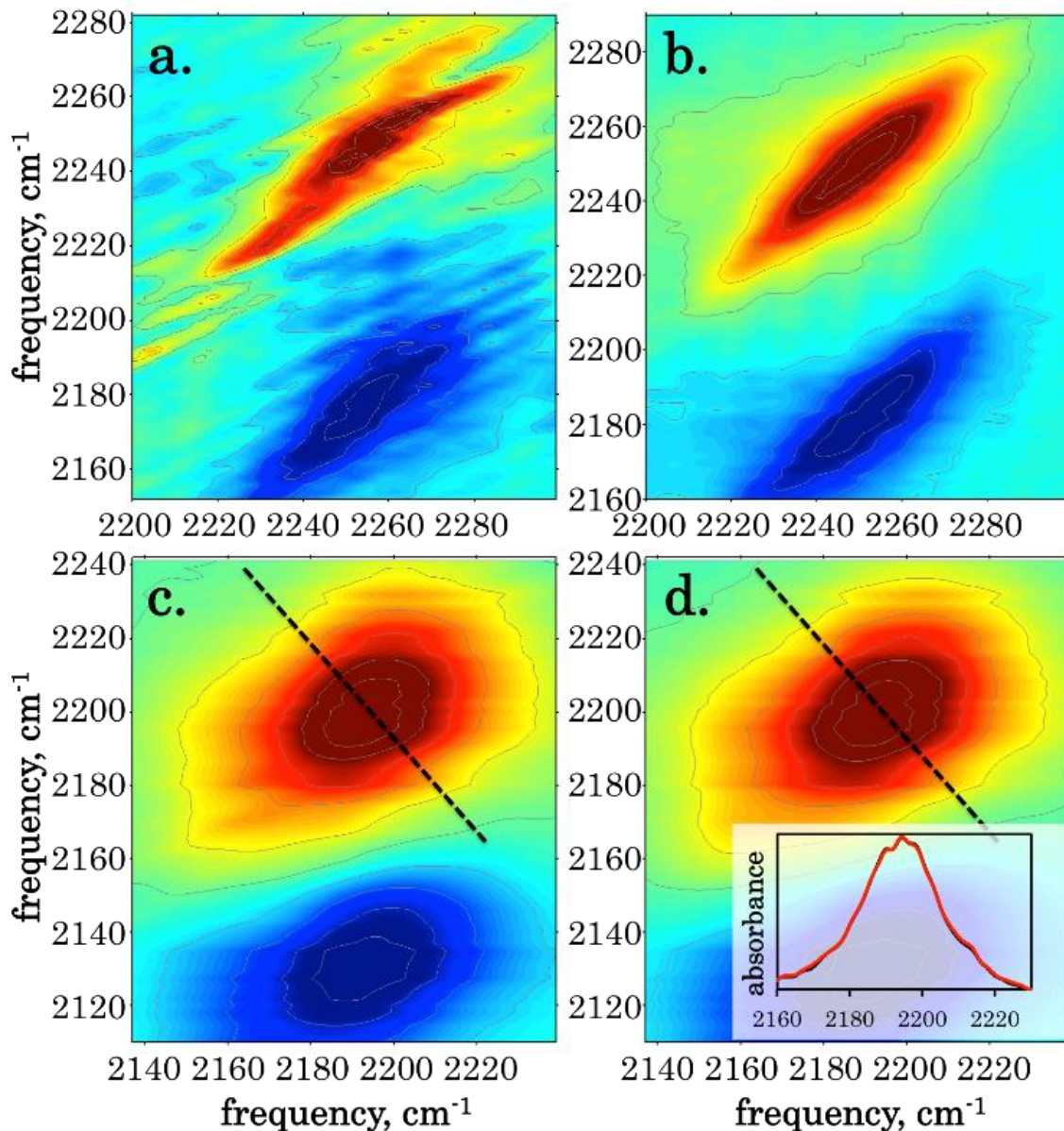
Figure 8: 2D-IR spectra collected for the Si-H vibration on a scattering porous silica sample a) without fibrillation and b) with fibrillation. Also shown are the 2D-IR spectra of the Si-H vibration on a silane in solution (low scatter sample) c) without fibrillation and d) with fibrillation. All four spectra were collected at T_w = 1 ps. Inset in frame d are the antidiagonal slices marked as dashed lines across frames c and d projected onto the frequency axis without (black) and with (red) fibrillation.

the echo wavepacket. The beam modulation leads to a decrease of T_w resolution of no more

than 15 to 20 fs for vibrational modes in the 1650 to 2300 cm^{-1} range.

To demonstrate the effectiveness of our method, we have collected 2D-IR spectra

on a porous silica sol-gel glass infiltrated with isopropyl alcohol. The material has IR-

active Si-H vibrations on the silica surface but is a relatively strong scatterer across the mid-IR, making it a challenging sample to study by 2D-IR. The 2D-IR instrument has been described in detail for previous experiments was only modified to include the changes shown in Figure 7.[60] In Figure 8a, the deleterious effect of scatter on the 2D-IR spectrum is evident in both the fundamental and anharmonically shifted transitions. With no other adjustments than turning on the PZA, including no additional shots averaged, the spectrum in Figure 8b is obtained with scatter artifacts removed. The effect is dramatic and enables the relevant peaks to be analyzed. To show that the fibrillation has no impact on non-scattering samples, 2D-IR spectra were also collected for the Si-H vibration on trimethoxysilane in isopropyl alcohol with and without fibrillation (Figures 8c and 8d). The spectra are indistinguishable and the inset antidiagonal slices show that the dynamical lineshape is unaffected by fibrillation.

The result of the work presented in this chapter was a fully-reflective, cost-effective approach to scatter reduction that can be readily implemented in an existing 2D-IR setup. Thus far we have found that this design is effective at eliminating scattered light that is a factor of five larger than the signal itself. Although we fibrillated the LO and pulse 3 in the experimental setup, this is completely analogous to fibrillating pulses 1 and 2 simultaneously. Furthermore, when a 2D-IR instrument utilizes the pump-probe geometry [61], only the third pulse would need to be fibrillated to achieve the same result. The results presented here demonstrate that the implementation of this approach enable 2D-IR spectroscopy to more readily address complex dynamical questions in highly scattering media.

All work presented in subsequent chapters was performed with fibrillation in whole or in part. Even homogeneous solution samples that shouldn't scatter still have small amounts due to scratches or dust on sample windows. The heterogeneous surface of silicon and TiO_2 nanoparticle films was a constant source of scatter.

Chapter 3 Observation of Proton Transfer Between Bridging Ligands on a Catalyst by 2D-IR Spectroscopy

Reproduced in part with permission from:

3.1 Introduction

Currently accepted hydrogenation mechanisms of Shvo's catalyst include an activation step in which the inactive ruthenium dimer undergoes scission to form two different catalytic species. In this chapter, 2D-IR measurement of the metal carbonyl vibrations of Shvo's catalyst was used to monitor early reaction dynamics for the inactive and activated catalyst. Kinetic analysis of exchange or cross peaks in the 2D-IR spectra demonstrate that thermally-activated intramolecular proton exchange occurs on the ultrafast time scale. The results indicate an activation barrier for proton transfer of 2.1 kcal/mol and an upper limit for dimer scission of 1.3×10^{11} s^{-1}. Deprotonation of the dimer leads to a pseudo stable species that remains dimeric at the ruthenium-hydride bridge for several hours. Measurements of this species using 2D-IR show that proton transfer is turned off, as expected. The data reveal new mechanistic details of the dynamic behavior of Shvo's catalyst leading up to activation and introduce the feasibility of substrate binding to the dimeric form of the catalyst prior to scission.

Elucidating catalytic mechanisms is performed almost exclusively by indirect methods. Hypothesized mechanisms are tested by comparing measured outcomes under varying reaction conditions to those predicted by the proposed mechanism. Landis and coworkers have referred to this as the "outside-in approach".[62] One reason for the indirect nature of mechanistic studies is a lack of time resolution. A slow temporal lens only allows observation of equilibrium average structures, obscuring short-lived catalytic intermediates. In reality, even very slow chemical reaction rates are the culmination of very fast barrier crossing events that are accompanied by structural dynamics that sample thousands of molecular configurations in a picosecond; a "slow" reaction means that the number of barrier crossing events per time is small, even though the crossings themselves are extremely fast. In fact, to experimentally observe elementary reaction steps requires a technique with temporal resolution on the ultrafast time scale of femtoseconds to picoseconds, commensurate with making and breaking of bonds. Notwithstanding the power of computational methods for this task, ultrafast spectroscopy is one of the few approaches that can offer direct glimpses into the movements of atoms and electrons during chemical reactions.[63-68]

Hydrogenation and dehydrogenation are two of the most important classes of chemical reactions that benefit from catalysis and 1-hydroxytetraphenylcyclopentadienyl-(tetraphenyl-2,4-cyclopentadien-1-one)-μ-hydrotetracarbonyldiruthenium(II), or Shvo's catalyst (Figure 9, **1**), is an important model compound capable of catalyzing both of these processes.[69-73] Shvo's catalyst has been studied for decades as a hydrogenation and dehydrogenation catalyst[69, 70] and has recently received renewed attention for its use in hydrogen storage and production.[72] Its rich chemistry is believed to arise from its

bimetallic nature and asymmetric scission yielding two similar catalytic species having very different reactivities (see Figure 9). Casey and coworkers performed isotope studies on scission product analogues that strongly suggested a simple one step outer sphere hydrogenation mechanism for carbonyl reduction by **2a** in Figure 9.[74] Catalysis then involves simultaneous donation of the acidic proton and a nucleophilic hydride to an organic carbonyl. It is the proximity and differing charge of these hydrogen atoms that make **2a** an effective catalyst. Although there is compelling (albeit indirect) evidence supporting scission as the activation step, the dissociation products are not observed under catalytic reaction conditions until after all of the substrate is consumed.[75] Hence, the equilibrium strongly favors the dimer species but involves some ultrafast chemical dynamics that produce transient reactive catalytic moieties.
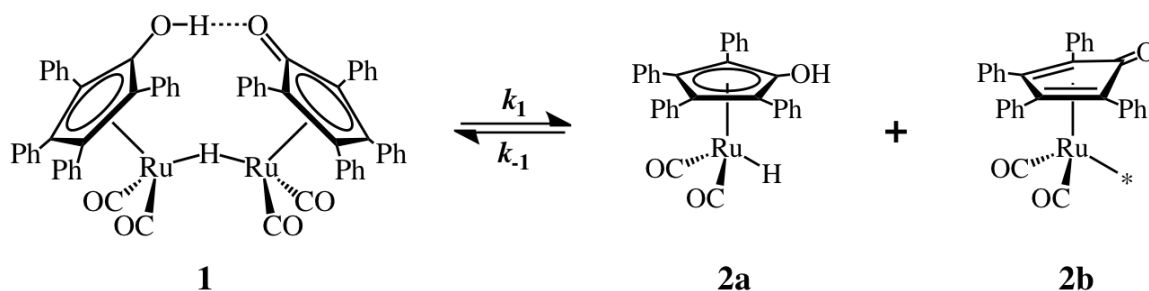
Figure 9: Accepted mechanism of Shvo's catalyst activation.

Unfortunately, ultrafast time resolution is not enough to capture direct evidence of the hypothesized scission intermediates. In an instantaneous snapshot of a reaction mixture, a large collection of catalysts and substrates may coexist in various states in the catalytic cycle. Therefore, even if FTIR spectroscopy had the time resolution to follow the reaction coordinate, which it does not, its spectral features would not show the interconversion of reaction intermediates under equilibrium or pseudo-equilibrium conditions that accompany transient species. For example, considering only the activation

step in Figure 9, every time a dimer dissociated to monomers a dimer would reform elsewhere in the sample volume, producing no net change in the FTIR spectrum. This is confirmed by the aforementioned FTIR studies that reported no changes in the spectrum of **1** while catalytic turnover was occurring.[75] A solution to this dilemma is found 2D-IR which, due to its coherent nature, can monitor the exchange of energy and chemical populations under equilibrium conditions on the ultrafast time scale.[5, 16, 76]

In the current study, the carbonyl vibrations on Shvo's catalyst were used to directly monitor its dynamic behavior by 2D-IR spectroscopy. Infrared spectroscopic measurements were performed over a range of temperatures and pH conditions to yield new insight into the dynamic behavior of this catalyst before and during activation. We employed density functional theory (DFT) calculations to assist in assigning vibrational modes to molecular structures. The results demonstrate that there is fast interconversion of molecular configurations on the time scale of ps, despite the seemingly static view presented by FTIR and even IR pump-probe spectroscopy. Importantly, we find that rapid proton exchange occurs between the bridged cyclopentadienyl ligands on resting and activated complexes while the hydride bridge remains intact. The kinetics of this exchange set an upper bound for the activation rate constant of Shvo's catalyst, an important and previously unmeasured detail of its catalytic mechanism.

3.2 Experimental Methods: Materials

1-Hydroxytetraphenylcyclopentadienyl-(tetraphenyl-2,4-cyclopentadien-1-one)-μ-hydrotetracarbonyldiruthenium(II) (Shvo's catalyst, **1**), tetrahydrofuran (THF), 1,8-diazabicyclo[5.4.0]undec-7-ene (DBU), and toluene were used as received from Sigma Aldrich. Fourier transform infrared spectra were collected on a Nicolet 6700 FTIR

spectrometer (Thermo Scientific) with at least 16 scans and a resolution of 2 cm^{-1}. Synthesis of **2a** was performed according to the literature procedure by placing 10 mL of a 2.295 mM solution of Shvo's catalyst in THF in a 25 ml dram vile while bubbling H$_2$ through the solution and stirring at 85 °C for 18 hours.[77] Mass spectrometry was used to confirm the products of the reaction were **2a** in at least 85% yield with some remaining **1**. Mass spectrometry was performed on a Bruker BioTOF II using electrospray ionization and PEG 600 as an internal calibrant. Deprotonated **2a** requires a peak at 543.0537 and a peak was observed at 543.0534.

3.3 Experimental Methods: DFT calculations

Density functional theory calculations were carried out on representative structures of **1**, **2a**, and **2b** to aid in data analysis. In all representative structures, the phenyl groups on the cyclopentadienyl ligands were replaced with hydrogen atoms. Gaussian 09 was used to perform calculations at the M06l level of theory using a 6-31 G(d) basis set for all nonmetal atoms and a LANL2DZ basis set and core potential for Ru.[78] Geometries were optimized followed by frequency calculations. Vibrational frequencies were scaled according to Laury and coworkers using a value of 0.964 though there does not appear to be a test set that uses core potentials for heavy metal atoms.[79]

3.4 Experimental Methods: 2D-IR Spectroscopy Laser Details

The 2D-IR instrument was described in Chapter 1.[60] Briefly, mid-IR pulses (3 μJ /pulse, 1 kHz repetition rate, 90 fs duration FWHM, ~200 cm^{-1} bandwidth FWHM) were tuned to the ruthenium carbonyl (Ru-CO) stretching region (~ 1985 cm^{-1}), divided into three ~1 μJ p-polarized pulses, and focused on the sample in a BOXCARS geometry.[42] The generated vibrational echo signal was coaligned with a local oscillator reference pulse (0.3-0.5 nJ per

pulse), spectrally resolved in a 0.32 meter monochromator with a 75 line/mm grating, and detected with the liquid N_2 cooled 64-element mercury cadmium telluride (MCT) linear array detector (Infrared Associates, Inc). The spectral resolution of the detection system was ~ 4 cm^{-1} using the 75 line/mm grating. Purely absorptive 2D-IR spectra were obtained using the technique described by Khalil and coworkers.[43, 55] In order to account for systematic and random errors in the instrumentation, the data were phase processed for analysis as opposed to absolute value spectra.[29] The pump-probe projection theorem and absolute value center method were used as constraints during this procedure.[28] IR pump-probe spectroscopy was carried out using the same laser system as described previously.[80] The resulting data plots were then analyzed using peak volumes to extract kinetic information directly from the 2D-IR data, as described in more detail below.[31, 81] For 2D-IR measurements, the ω_τ, (pump or excitation) axis was achieved by scanning τ in increments of 5 fs and subsequent Fourier transformation. Beam 3 was chopped at 500 Hz and the chopped signal was divided by the laser spectrum to account for the laser power differences across the range of frequencies examined.

3.5 Results and Discussion of Shvo
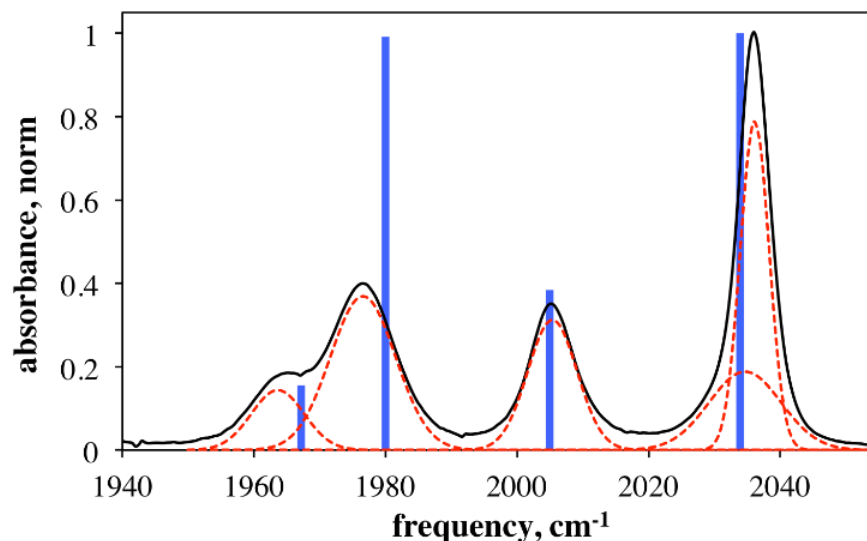
Figure 10: Baselined, normalized, and solvent subtracted room temperature FTIR spectra of Shvo's catalyst, 1, in toluene. Dashed red lines are Gaussian curves that best fit the lineshapes. Overlaid in blue are the DFT calculated vibrational frequencies and amplitudes for a model complex.

The FTIR spectrum of **1** in toluene, a common reaction solvent,[69, 74, 75, 82-84] is shown in Figure 10. The spectrum reflects the room temperature resting state of Shvo's catalyst with four peaks in the carbonyl stretching region at 1964, 1977, 2005, and 2036 cm^{-1}. Peak centers were determined by fitting to Gaussians (overlaid dashed lines), and all fit parameters are tabulated in Table 1. A weak fifth Gaussian was necessary to capture the asymmetry of the 2036 cm^{-1} peak. The DFT calculated frequencies for a representative structure of **1** are overlaid on the spectrum in Figure 10. Calculations provided normal

mode atom displacements, which were used to facilitate assignment of the four peaks when treating Shvo's catalyst under C_{2v} symmetry. Under this pseudo symmetry shown in Figure

	Room Temp			High temp	
species	peak center ν_{CO} (cm^{-1})	peak width FWHM (cm^{-1})	lifetime T_1 (ps)[a]	peak center ν_{CO} (cm^{-1})	peak width FWHM (cm^{-1})
1 (dimer)	2036.12	5.19	15.9 ± 0.2	2036.04	5.16
	2034.66	12.93		2033.71	12.46
	2005.37	8.82	15.0 ± 0.4	2005.36	9.12
	1976.57	11.67	18.5 ± 0.4	1976.81	12.52
	1963.62	9.46		1962.74	10.03
2a (hydride monomer)	2013.12	8.19			
	1954.02	9.51			

Table 1: Tabulated FTIR parameters for Shvo FTIR fits.

11 the carbonyl vibrational modes are assigned as $v_1 = 2036$ cm^{-1} = A$_1$, $v_2 = 1964$ cm^{-1} = A$_2$, $v_3 = 2005$ cm^{-1} = B$_1$, $v_4 = 1977$ cm^{-1} = B$_2$. The four modes are depicted graphically in Figure 11. The A$_2$ mode is not IR active under perfect C_{2v} symmetry but is observed experimentally due to a break in molecular symmetry. It has the weakest signal consistent with a weaker transition dipole moment. The positions of the peaks at 2036 cm^{-1} and 2005

cm^{-1} are consistent with those reported previously by Casey and coworkers for Shvo's catalyst in the same solvent.[75] The peaks at 1964 and 1977 cm^{-1} were previously unassigned, and the full IR spectrum has not been reported to the best of our knowledge.

Scission of **1** is believed to occur at ~ 328 K, the temperature at which catalytic reactions are often carried out, although a range of reaction temperatures are reported in the literature.[69, 74, 75, 82-84] This mechanistic step producing **2a** for hydrogenation/reduction and **2b** for dehydrogenation/oxidation reactions requires the two bridging hydrogen atoms to remain on one species,[71, 73] producing ruthenium complexes with different hapticities to the cyclopentadienyl ligand, as shown above in Figure 9. Monomers **2a** and **2b** should have different FTIR spectra. In practice, the FTIR spectra of solutions of **1** at room temperature and 328 K are indistinguishable; no evidence of the either **2a** or **2b** was observed. There are no reported frequencies of **2b** as it is believed to be short lived, however, Casey and coworkers reported the carbonyl vibrations for **2a** to be 1957 and 2018 cm^{-1}.[75] We performed DFT calculations on a **2a** model compound and found the corresponding vibrations at 1976 and 2028 cm^{-1}. We also synthesized monomer **2a** in THF and its FTIR spectrum (shown later in this report in Figure 19d) showed two peaks in agreement with Casey and coworkers.[77] Based on FTIR analysis, the resting state of

Shvo's catalyst and its activated form at 328 K appear to be generally static, but we will demonstrate below that this is not the case.

The vibrational lifetime of the high frequency carbonyl modes on **1** are important because they reflect the time scales of configuration space sampling leading to a chemical turnover event. Figure 12a shows the IR pump – IR probe spectrum collected for **1** in toluene at a delay time of 1 ps. Positive spectral peaks due to ground state bleaching are accompanied by red shifted negative-going peaks due to absorption of the first excited vibrational state within an anharmonic potential (the v=1 to v=2 transition). The spectrum

$$v_1 = 2036 \text{ cm}^{-1} = A_1 \qquad v_3 = 2005 \text{ cm}^{-1} = B_1$$

$$v_4 = 1977 \text{ cm}^{-1} = B_2 \qquad v_2 = 1964 \text{ cm}^{-1} = A_2$$
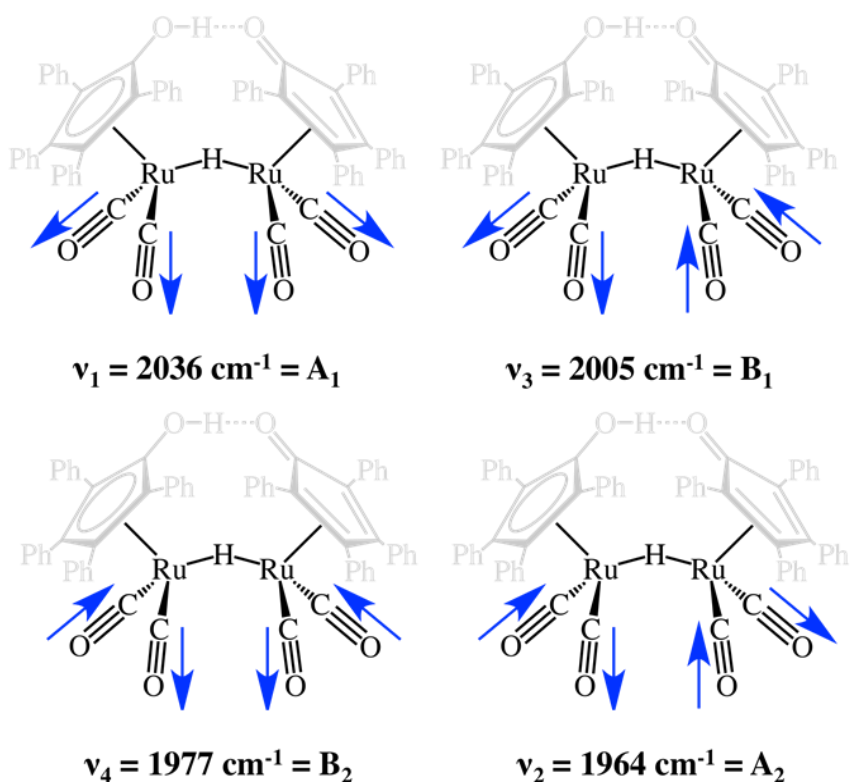
Figure 11: Vibrational mode atom displacements.

contains multiple overlapping peaks that required the spectra at each delay time to be fit

with a sum of Gaussians. A single Gaussian peak was fit to each positive and negative

peak (8 Gaussians) at an early probe delay time to reproduce the pump-probe spectrum.
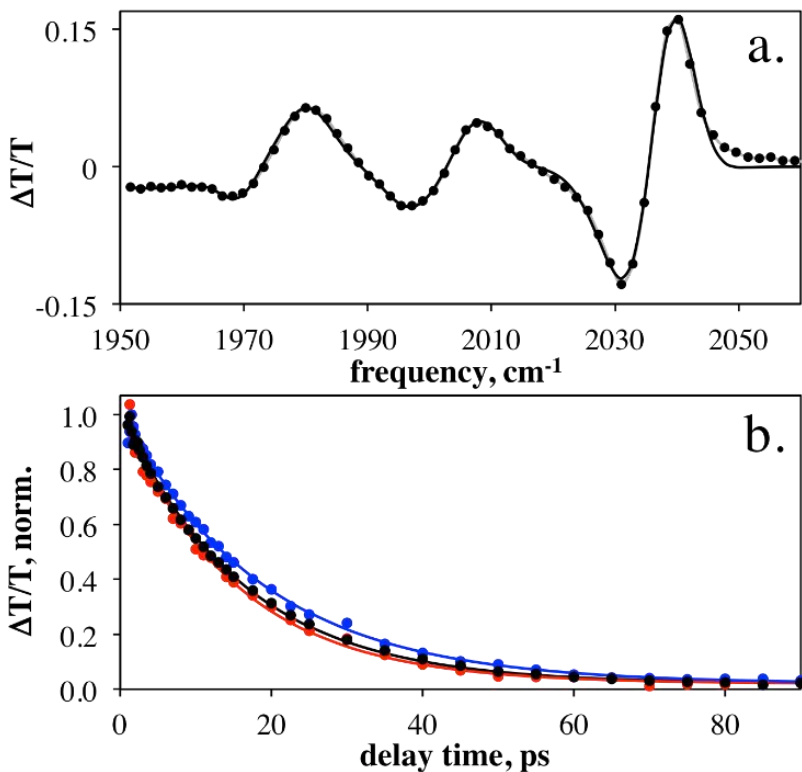
Figure 12: a) IR pump-IR probe spectrum measured at a pump delay time of 1 ps; overlaid solid line shows multi-Gaussian fit to the spectrum used to determine mode relaxation times. b) Amplitude decays (vibrational relaxation) for the modes centered at 2036 (black), 2005 (red), and 1977 cm^{-1} (blue). Overlaid solid lines are single exponential fits to the data.

Then the center frequencies of these Gaussians were fixed based on this fit while the

amplitudes and widths for all peaks were allowed to vary as a function of spectrum delay

time. The amplitude decays for the three most intense peaks are shown in Figure 12b, and

their time constants are included in Table 2. The vibrational lifetimes for the 1977, 2005,

and 2036 cm^{-1} modes are similar with values of 15-18 ps based on single exponential fits

(overlaid in Figure 12b). The signal-to-noise for the A$_2$ mode at 1964 cm^{-1} was not

sufficient to determine the relaxation time by this measurement. Fit qualities were

marginally improved with a second exponential term but the time scales of the second

terms were similar to the first, so their inclusion was not justifiable. Within experimental error the similar vibrational lifetimes suggest similar energy dissipation pathways for all the carbonyl vibrations on **1**. The pump-probe spectra, like the FTIR spectrum, support a static view of the resting state of Shvo's catalyst in the sense that the relative populations of each mode remain constant over the time scale of vibrational relaxation.
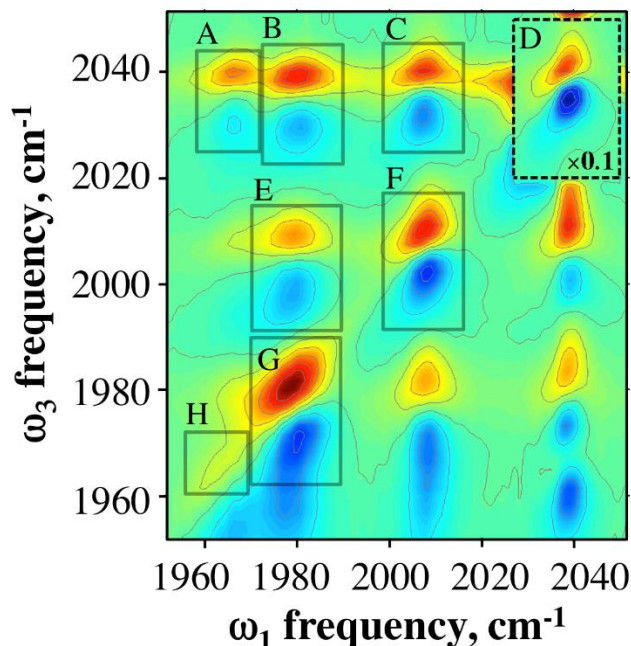
Figure 13: 2D-IR spectrum of Shvo's catalyst (1) in toluene at 293 K at T_w = 1.5 ps. Red and blue features are positive- and negative-going, respectively. Contour lines indicate 10% of the max-to-min values for the plot taken after the intense peaks in the dashed box were multiplied by 0.1 to make all peaks visible on the same scale. Boxes A-H indicate regions where volume analysis was performed on 1 or 2 peaks.

To delve deeper into the molecular dynamics of **1**, we first carried out 2D-IR measurements at room temperature (293 K). A representative 2D-IR spectrum of **1** at a waiting time of 1.5 ps is shown in Figure 13. It is immediately apparent that the multidimensional spectra contain a wealth of new information not revealed by FTIR or pump-probe spectroscopy. Normal modes on the same molecule are often anharmonically coupled such that excitation of one mode immediately results in amplitude in the coupled modes. This appears in a 2D-IR plot as off-diagonal peaks at all T_w values (particularly early times).[31, 85, 86] Chemical exchange and intramolecular vibrational redistribution (IVR)

can also result in off-diagonal peaks that increase in amplitude as a function of T_w, which differentiates them.[44, 76, 86-88]

In Figure 13, four on-diagonal ($\omega_1 \cong \omega_3$) resonances are observed as positive-going (red) peaks, and each has a corresponding negative-going v=1-2 transition below it, anharmonically shifted by about 10 cm^{-1}. The similar anharmonicities of all the vibrational modes suggest that their potential energy surfaces have comparable curvature, which is expected since each mode involves atomic displacements within all four carbonyl ligands (see Figure 11). All four on-diagonal modes also show prominent off-diagonal peaks even at the shortest measured T_w times, confirming that these modes are anharmonically coupled and the vibrational energy is very rapidly redistributed among them.[31, 85, 86] Even the weak 1964 cm^{-1} vibration is clearly coupled to the higher frequency modes as its off-diagonal peaks are amplified by the stronger modes. Each off-diagonal ($\omega_1 \neq \omega_3$) peak appears as a positive and negative pair where the peak separation is a direct measure of the coupling strength (~10 cm^{-1}) of the modes that they connect on the diagonal. In the limit of no coupling, the peak separation is zero and the positive and negative features perfectly cancel.[31] The fact that all cross peaks are of relatively equal intensity and that all diagonal peaks are coupled further confirms that these four modes are on the same molecule and are not due to monomer **2a** or **2b**.

Eight boxes have been labeled A-H on Figure 13 to indicate regions where the volumes of peaks were obtained by fitting positive- and negative-going Gaussian peaks to the data. The kinetics of these volumes reflect the time-dependent populations and coherences of the carbonyl vibrational modes. Figure 14a shows the on-diagonal volumes from locations D, F, G, and H, which correspond to the A_1, B_1, B_2, and A_2 modes,

respectively, in Figure 11. The relaxation of the A_1, B_1, and B_2 populations are similar, while the weak A_2 mode is notably faster. The A_1, B_1, and B_2 modes required a biexponential functional form to model their volume decays. Time constants of the fitted parameters are tabulated in Table 2 and are the same within error at 4.6 and 23 ps, on average. The A_2 mode relaxation is well described by a single exponential with a time

region	approximate coordinates (cm^{-1})	anharmonicity (cm^{-1})[b]	coupling (cm^{-1})[b]	time constant(s) (ps)[a]	high T	Low T	normalized decays (ps)[d]
A	1964 / 2036		9.0 ± 2.5	31 ± 17			9.3 ± 2.6
B	1977 / 2036		7.9 ± 1.2	22 ± 4			11.3 ± 3.1
C	2005 / 2036		4.2 ± 2.3	19 ± 4			6.5 ± 1.9
D	2036 / 2036	3.6 ± 1.7		4.6 ± 2.9, 23 ± 19	4.3 ± 1.6, 17 ± 2	1.3 ± 0.3, 18 ± 4	
E	2005 / 1977		5.8 ± 2.3	23 ± 5			4.4 ± 1.0
F	2005 / 2005	6.1 ± 2.7		3.8 ± 1.9, 21 ± 10	4.7 ± 1.3, 29 ± 3	17 ± 2	
G	1977 / 1977	15 ± 3		5.3 ± 3.1, 24 ± 27	3.1 ± 1.8, 23 ± 18	11 ± 3	
H	1964 / 1964	N/A[c]		2.5 ± 0.5	13 ± 3	–	

Table 2: Kinetic fits to 2D-IR spectra of Shvo. Error a reflects the standard error for the fitted parameter. Error b is standard deviation for fitted peak centers. For c anharmonicity could not be obtained. For d, the A, B, and C are normalized by D, E, and F respectively.
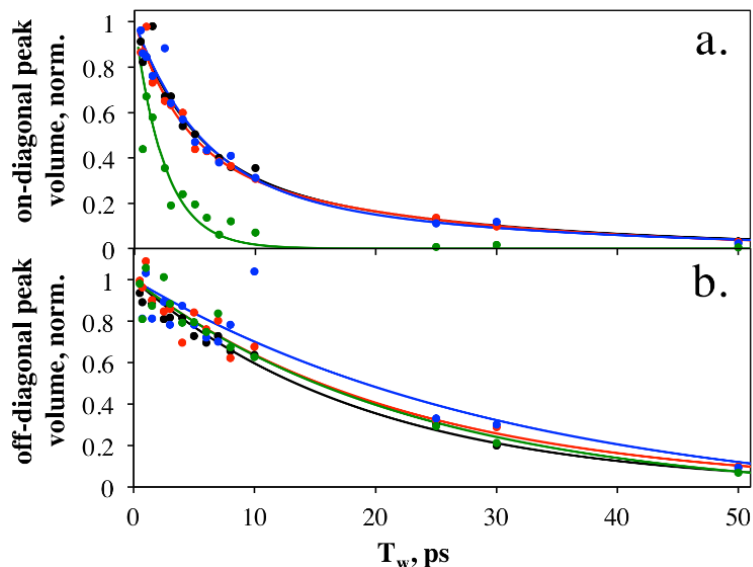
Figure 14: Normalized volume decays for a) on-diagonal regions D (black), F (red), G (blue), and H (green), and b) off-diagonal regions A (blue), B (red), C (black), and E (green). In both frames the markers show data and solid lines are exponential fits to the data.

constant of 2.5 ps. We believe that the fast relaxation of this peak is the result of strong spectral overlap with a solvent peak in toluene at nearly the same frequency, leading to efficient energy transfer from this mode into the bath.[80, 89, 90] The population decays from the 2D-IR spectra are different than the pump-probe measurements of the CO modes on **1**. The pump-probe spectra (Figure 12a) are reproduced by the projection of the absorptive 2D-IR spectra (Figure 13) onto the vertical axis, superimposing the off- and on-diagonal peak dynamics.[28] Therefore, the relaxation times of the vibrational modes of **1** are more accurately given by the decay of the on-diagonal peak volumes.

The off-diagonal peak volumes (A, B, C, and E) shown in Figure 14b also have similar kinetics. Single exponential decays reproduce the data well and give an average time constant of 24 ps. Comparing Figures 14a and 14b it is clear that the off-diagonal volumes decay differently than the on-diagonal peaks, which indicates that there must also be exchange occurring during the T_w period.[44, 76, 86-88] Since the off-diagonal peaks should decay with the on-diagonal populations, we normalized each off-diagonal peak by its on-diagonal peak volume at the emission frequency.[31, 81] All four normalized off-diagonal peak volumes (A/D, B/D, C/D, and E/F) grew with the same T_w dependence within the error of the measurements (see Table 2), and the averaged normalized off-diagonal volumes at 293 K are shown in Figure 15a. The averaged data were well fit by a single exponential rise with a time constant of 7.5 ± 1.3 ps.
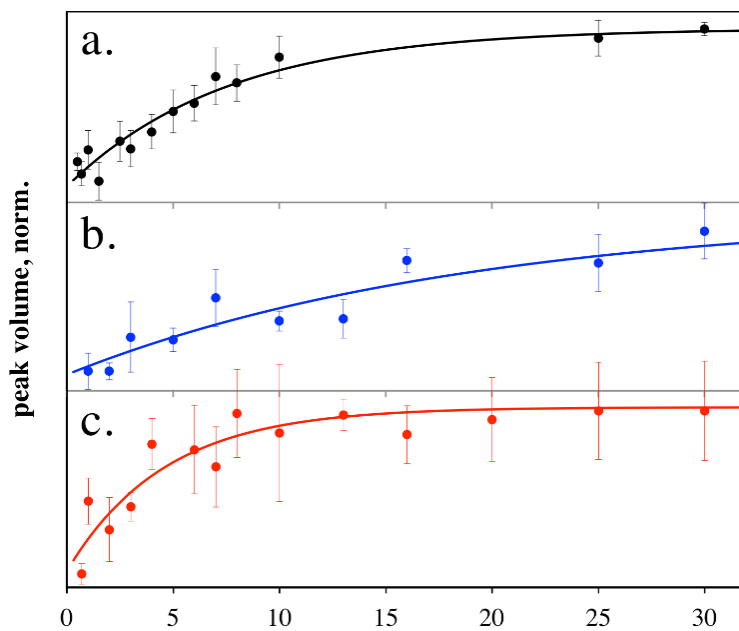
Figure 15: Combined average off-diagonal peak volumes for regions A, B, C, and E normalized by their on-diagonal volumes at the emission frequency (A/D, B/D, C/D, and E/F) as a function of T_w measured at a) 293 K, b) 230 K, and c) 328 K. Solid lines show the exponential rise fit to the data and error bars reflect the standard deviation of the normalized data at each T_w.

One possible explanation for the off-diagonal dynamics in Figure 15a is intramolecular vibrational redistribution (IVR) among the CO modes on **1**. Alternatively,

one could invoke chemical exchange between two resting state conformations that have
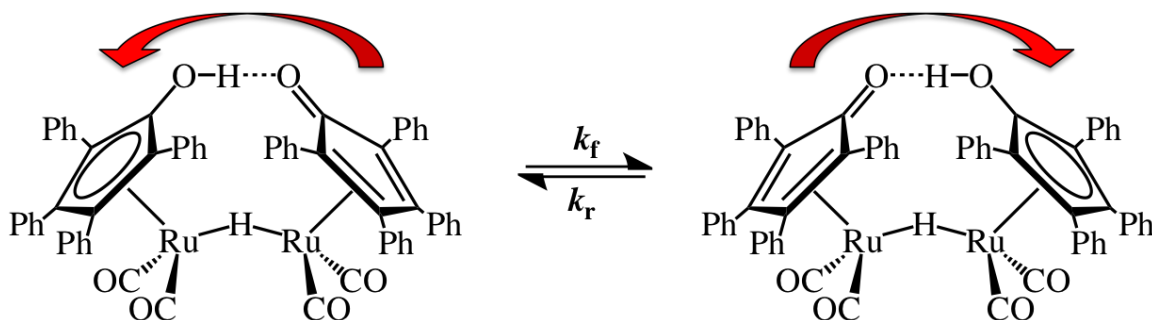
Figure 16: Proposed ring-slip mechanism in Shvo's catalyst.

similar vibrational spectra. To this point, DFT calculations performed on a representative

dimer structure indicate that the acidic bridging proton is not equally shared between the

cyclopentadienyl rings (see Figure 17). The carbon-carbon bond lengths in the

cyclopentadienyl rings indicate that the ketone-like ring binds to ruthenium in an η^3

configuration whereas the alcohol-containing ring binds η^5. More importantly, ring-slips

from η^5 to η^3 have been invoked in catalytic mechanisms to explain substrate binding,

lending some indirect support to the notion that this configuration is fluxional during

catalysis.[91] It has also been reported that the alcohol proton on the cyclopentadienyl ligand

of an analogue of **2a** is more acidic than benzoic acid.[77] An organic carbonyl such as the

ketone-like cyclopentadienyl ring in **1** could be protonated by such an acid. Therefore, it

is reasonable and potentially relevant for catalysis that the bridging proton in **1** could

exchange on the ultrafast time scale, as shown in figure 16. In fact, the measured time

scale of 7.5 ps in Figure 15a is consistent with the time scale of hydrogen bond exchange

in liquids.[92, 93] Our own DFT calculations of the dimer species reveal an active low

frequency vibrational mode at 254 cm^{-1} that matches the structural motion of ring-slip and

proton exchange depicted in Figure 16 and also the time scale of off-diagonal peak growth

in Figure 15a. Therefore, dynamic exchange between two resting state conformers that are

equal in energy and have identical vibrational spectra as opposed to IVR is a feasible alternative explanation for the off-diagonal dynamics observed by 2D-IR.

As enticing as the proton exchange mechanism seems, Occam's razor predicts that IVR is the more likely explanation for off-diagonal dynamics in the 2D-IR spectra of Shvo's catalyst. IVR can be differentiated from chemical exchange by its temperature dependence.[9, 19, 94] Chemical exchange for a process requiring an activation energy, E_a, is predicted to have an Arrhenius behavior with temperature:

$$k_{exchange} \propto exp\left[-\frac{E_a}{k_B T}\right] \qquad (26)$$

In contrast, IVR requires energy in the form of phonons from the bath to match the mode splitting, E_p, giving a different temperature dependence:

$$k_{IVR} \propto \left(exp\left[\frac{E_p}{k_B T}\right] - 1\right)^{-1} \qquad (27)$$
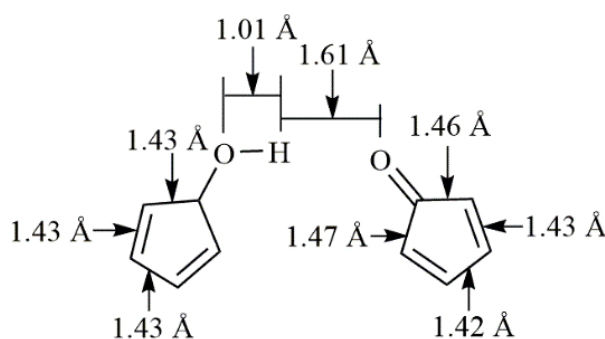
Figure 17: Bond lengths or atom distances predicted by Gaussian calculations. The two unlabeled bonds have bond lengths the same as on the other side of the ring. The lengthening of the two bonds near the ketone group indicate less electron density and the pi electrons are more concentrated on the remaining three bonds which is consistent with η³ binding to its Ru.

We collected 2D-IR spectra for **1** at 230 K and 328 K to complement the 293 K data. DFT calculations indicate a proton exchange transition state 3.2 kcal/mole higher than the ground state. For this E_a, we expect that the exchange rate should be a factor of four times lower at 230 K than it is at 293 K, and nearly a factor of two times higher at 328 K than it is at 293 K. In contrast, assuming a mode separation of $E_p = 30$ cm^{-1}, the rate coefficient for IVR would increase by less than a factor of 1.5 over this entire ~100 K temperature range. Therefore, although both rate coefficients should increase with temperature, the magnitude of the change should assist in assigning an origin to the off-diagonal kinetics.

The on-diagonal populations are not overly sensitive to temperature differences and have the same dynamics within the errors of our measurements. A plot of the on-diagonal peak volumes for the A$_1$ mode that has the highest S/N indicates that all the decays are indistinguishable. In contrast, the averaged off-diagonal volumes normalized by the appropriate on-diagonal peaks are quite different, as shown in Figures 15b and 15c at 230 K and 328 K, respectively. It is clear that the low temperature off-diagonal peak growth has been significantly slowed, yielding a rise time constant of 19 (±6) ps. At the higher temperature (Figure 15c), the off-diagonal kinetics show a time constant of 4.6 (±1.3) ps, which closely matches the two-fold increase predicted for a thermally activated exchange process. It is likely that both IVR and proton exchange are occurring simultaneously, but our temperature dependent 2D-IR analysis demonstrates that the dynamics on the time scale of a few to tens of ps is dominated by exchange rather than IVR. Presumably IVR is completed within 1 ps. An Arrhenius plot of the rate coefficients at these three
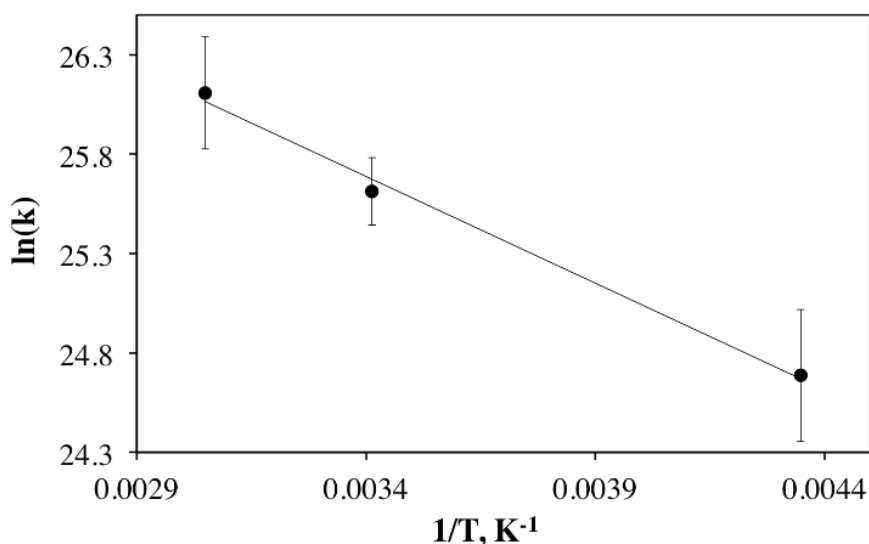
Figure 18: Arrhenius plot of the rate constant for off-diagonal peak volume growth at 230, 293, and 328 K.

temperatures is shown in Figure 18 and its slope indicates an $E_a = 2.1$ kcal/mol, which is consistent with an activation energy for proton transfer.[95]

To further confirm our hypothesis of proton exchange in **1**, we performed 2D-IR spectroscopy on **1** deprotonated with 1,8-diazabicyclo[5.4.0]undec-7-ene (DBU), a bulky organic base. DBU extracts the cyclopentadienyl proton and opens up the top half of the dimer. Measurements were performed on deprotonated **1** using a 2:1 ratio of DBU:**1** in toluene at room temperature (293 K). The FTIR spectrum of the initially prepared sample is shown in Figures 19b and 19e. The spectrum of **1** is plotted above it in black (Figure 19a) as a reference. Initially, the solution contains a mixture of two species: the dimeric Shvo's catalyst **1** with the proton bridge broken, which we call **1'**, and a new decomposition product with only two carbonyls on a single ruthenium. This is almost certainly the conjugate base of **2a**, which we call **2a'**. Dashed lines indicate how the four modes on **1** (Figure 19a) red-shift to the four modes on **1'** (Fig 19b). DFT calculations corroborate a red shift of between 27 and 42 cm^{-1} upon scission of only the proton bridge to yield the

anionic **1'**. This species is pseudo-stable but irreversible decomposition occurs after many hours to give **2a'**. DFT calculations predict a red shift of 68 to 74 cm^{-1} upon deprotonation of **2a** to **2a'**, which is consistent with the red-shift observed in the FTIR spectrum of **2a'** (Figure 19c) relative to **2a** (Figure 19d). Calculations for **1'** and **2a'** predict red shifts larger than experimental values but the trends are correct in both cases. Additionally we find that the FTIR spectrum in Figure 19a is recovered if acid is added in excess of DBU within 24 hours. At longer times (>24 hours) the spectrum approaches irreversibly that of Figure 19c. When Hunig's base is added to Shvo's catalyst in toluene the resulting carbonyl frequencies are identical to those in Figure 19c. Hunig's base is more basic than DBU but does not bind to metals, confirming the assertion that the DBU treatment breaks the proton bridge but not the metal hydride bridge. Pyridine, which is less basic than DBU but a stronger chelator, was also added in excess to Shvo's catalyst and but gave no change in the carbonyl frequencies indicating that it neither deprotonates **1** nor binds to the Ru atoms. All of this supports the assignment of **2a'** to the decomposition product whose spectrum is shown in Figure 19c. The dashed lines show how the two modes on this decomposition product match up to two of those on the earlier spectrum.

A 2D-IR spectrum of the sample prepared upon initial addition of DBU is shown

in Figure 19f. Three zones have been indicated as regions where peak volume analysis
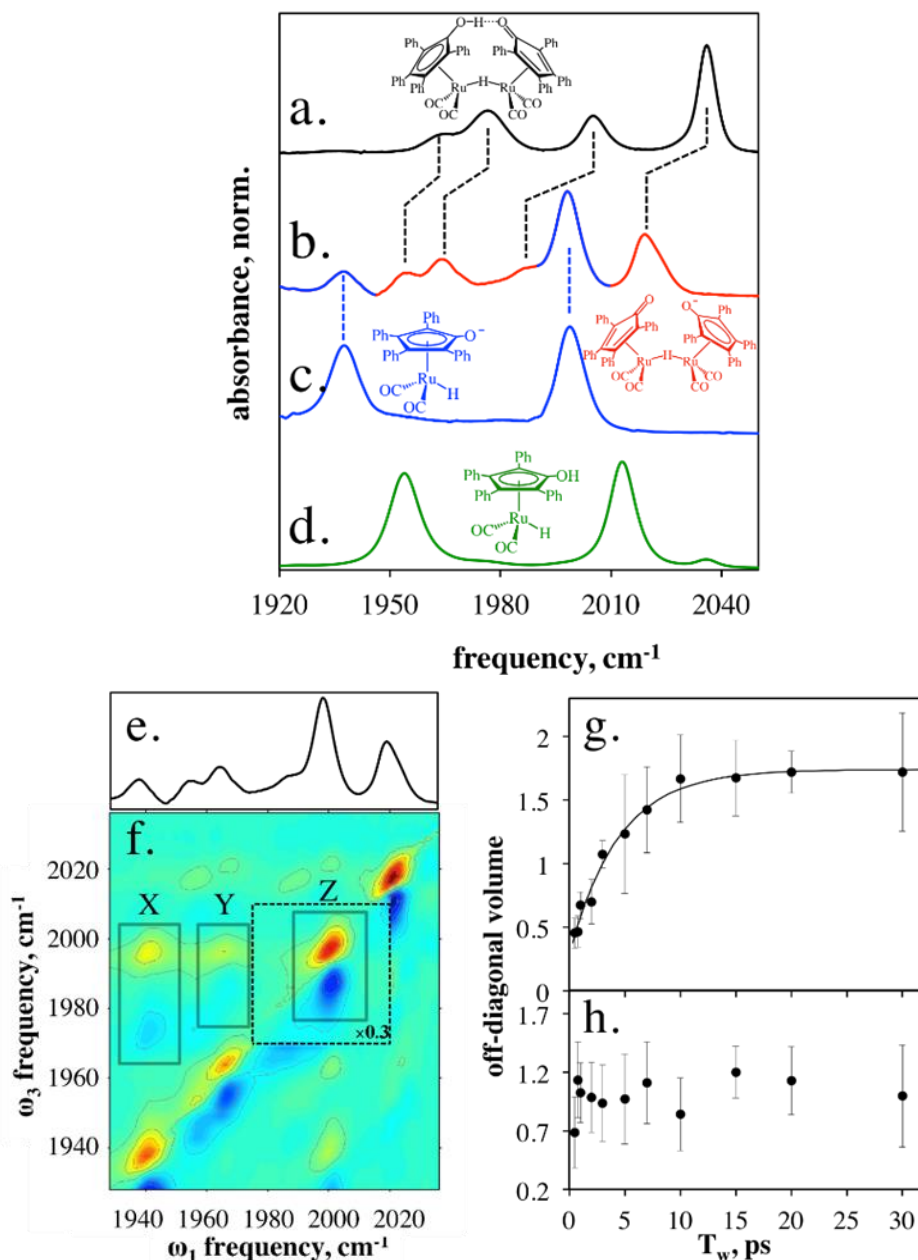
Figure 19: : FTIR spectra for a) 1, b) 1', c) 2a', d) 2, and e) 1 reproduced above the 2D-IR spectrum for clarity.
f) 2D-IR spectrum of a 2:1 ratio of DBU:1 in toluene. g) Off-diagonal peak volumes from region X
corresponding to 2a' normalized by their corresponding on-diagonal population in region Z. h) Off-diagonal
volume in region Y corresponding to 1' normalized by the peak volume in region Z.

was performed. Zone X represents the off-diagonal peak that couples the two modes on

the decomposition product, which is notably more strongly coupled than the modes on the

dimer based on the peak separation of nearly 20 cm^{-1}. Normalizing the peak volumes in this region by the on-diagonal peak volume gives the exponential rise in Figure 8g that has a time constant of 4.4 ($\pm$0.5) ps. In contrast, the peak volumes in zone Y are associated only with **1'** and demonstrate that the exchange dynamics have been turned off upon deprotonation (Figure 19h).

The spectral resolution of 2D-IR enables us to confirm our hypothesis that the off-diagonal dynamics reflect thermally activated proton transfer in the bridging species. Analysis of the 2D-IR spectra collected at later reaction times for the solution that contains only the decomposition product **2a'** corresponding to the FTIR spectrum in Figure 19c reveals that the off-diagonal kinetics persist with effectively the same time dependence. We have not identified the origin of these dynamics, but they should be different than those of **1** since this is a different molecule. We hypothesize that the 4.4 ps dynamics in **2a'** likely represent some solvent-mediated IVR pathway as has been observed for other metal-bound carbonyl systems.[44]

The accepted mechanism for carbonyl hydrogenation by **1** involves concerted proton transfer from the hydroxycyclopentadienyl ring and the metal hydride regions of the complex.[74] On the other hand, imine reduction is greatly affected by ligand substituents and was reported to follow a wholly different mechanism from carbonyl reduction based on isotope studies.[73] One question that arises from this disparity is whether or not the substrate is bound to the dimer before scission occurs. The fact that we see proton exchange is important in this regard since intramolecular proton exchange occurs along one of the main reaction coordinates for dimer scission. Our results show that the bridging proton is labile and becomes more so approaching the activation temperature. We also

observe that the dimer persists even after deprotonation, held together by the bridging hydride that must form a stronger junction than the proton bridge. Taken together, our results support a view of the reaction in which the substrate is first protonated by the hydroxycyclopentadienyl ring on the dimer, followed by dimer scission and catalytic turnover. This would of course depend on the pKa of the substrate relative to the pKa of Shvo's catalyst. If the mechanism were pKa dependent that would explain the disparity of mechanisms between imines and carbonyls.

3.6 Shvo's Catalyst Conclusions

The temperature dependent studies described herein show that there is thermally activated proton transfer occurring on the time scale of a few ps in the resting state of Shvo's catalyst that is accelerated at higher temperatures approaching activation conditions. The dynamics and lability of this bridging proton is mechanistically relevant since it occurs along the reaction coordinate for the scission of **1** (Figure 9) producing the catalytic species. The rates of exchange give an upper limit for the time scale of dimer scission of 1.3×10^{11} s^{-1}. This rate is distinct from vibrational relaxation and could not have been determined without the aid of 2D-IR spectroscopy. At 328 K, no monomer was observed showing that even when the system is activated most of the catalyst exists in the resting state under catalytic conditions. Proton exchange coupled to a ring slip mechanism reflects a transient softening of the dimeric structure that potentially allows the substrate to begin to dock at the catalyst active site. We propose that the binding of the substrate might first occur at the bridging proton even before the dimer splits to the monomeric form. This mechanistic detail could be tested by ultrafast measurements on the complex in the presence of substrate. Based on our results, it can also be concluded that the scope of this

particular transition metal catalyst may also be extended using multifunctional aromatic ligands that are pH sensitive. The current study shows that the 2D-IR technique and the CO ligands on Shvo's catalyst offer an exquisitely sensitive, "inside-out"[62] approach to directly monitoring the chemical steps occurring within the catalytic cycle on the time scale of chemical reactions or barrier crossings for transition states. Ultimately, we envision that such efforts will yield greater insight into catalytic mechanisms and allow rational design of improved catalysts. This example of exchange measurement was particularly challenging to determine due to anharmonic coupling and the counter intuitive self-exchange. Following this were clearer exchange measurements on a unique system allowing surface sensitivity.

Chapter 4 Measuring Dopant-Modulated Vibrational Energy Transfer Over the Surface of Silicon Nanoparticles by 2D-IR Spectroscopy

4.1 Introduction

2D-IR spectroscopy was used to characterize the vibrational dynamics of surface hydride modes on silicon nanoparticles (SiNPs). Energy transfer was compared between undoped (intrinsic) SiNPs and particles that were doped with boron and phosphorus. FTIR spectra reported changes in the relative proportions of $Si-H$, $Si-H_2$, and $Si-H_3$ populations when boron and phosphorus atoms were incorporated, while 2D-IR spectroscopy revealed that there was VET on the tens of ps time scale between all three mode types for intrinsic SiNPs. This energy transfer was severely diminished by including just 0.05 atomic % of boron and was completely extinguished for 2.5 atomic % of phosphorus. In addition, the vibrational lifetimes of mono- and polyhydride modes on intrinsic silicon particles were uniformly fast, while doped nanoparticles showed frequency dependent relaxation times reminiscent of porous and amorphous silicon films.

The unique properties of nanomaterials depend largely on the characteristics of their surfaces.[96-98] Surface atoms are necessarily different from bulk atoms in their bonding characteristics, surface energies, and electronic structures, and in nanoparticles with diameters less than 10 nm, a large fraction of the atoms are considered surface atoms.[99] A primary example of the emergent properties of nanoparticles is found in silicon, a material that is ubiquitous in electronics applications. Unlike bulk silicon, SiNPs exhibit enhanced absorption in the infrared[100, 101] and tunable photoluminescence due to quantum confinement effects.[102-104] More recently, doped SiNPs and nanowires have been explored as potentially less-toxic replacement materials for traditional quantum dots in electronic and opto-electronic applications.[105-107] Since the surface comprises a large proportion of the particle volume, it is critically important to control the surface chemistry in order to preserve silicon nanoparticle behavior. Well-defined nanoparticle surfaces are needed in order to draw quantitative connections between surface structure and particle function. Although noble metal and other semiconductor nanocrystals can be synthesized with well-defined terminal faces,[108-114] this is rarely the case for silicon particles. The surfaces of SiNPs are readily oxidized leading to inhomogeneous, amorphous coatings that are difficult to characterize.[107, 115-119] Chemical doping leads to similar disruptions of particle surface structure that obscure surface features in a shroud of heterogeneity.[105]

Infrared absorption and Raman spectroscopies offer two approaches to characterizing the structure and inherent disorder of silicon surfaces.[97, 120, 121] Single crystal and amorphous silicon materials are commonly hydrogen-passivated to eliminate defects and improve their electronic properties.[122] This results in surfaces that are covered with monohydride (R_3Si-H) and polyhydride (R_2Si-H_2 and $RSi-H_3$) vibrational modes that are

sensitive to their local chemical environments.[52, 120, 123-126] Surface adsorption, desorption, and functionalization depend largely on the vibrational lifetime of these surface modes,[122, 127] whose relaxation dynamics are often dominated by defects.[128] Lyding and coworkers reported that hot electron degradation in silicon transistors was up to 50 times slower for deuterium-passivated surfaces,[129] leading to enhanced carrier transport as a direct result of a shorter Si-D vibrational lifetime.[122] Vibrational dynamics have been measured in single crystal,[128, 130-133] porous,[134] and amorphous silicon.[135-138] The current study expands this body of knowledge by applying ultrafast two-dimensional infrared (2D-IR) spectroscopy to undoped and doped SiNPs for the first time. The measurements enable us to not only determine the relaxation times of these modes, but to also monitor coupling and energy transfer between surface modes in the presence and absence of doping. In doing so, we are able to infer structural information from within the heterogeneous environment of SiNP surfaces.

4.2 Silicon Nanoparticles Experimental

Silicon nanoparticles were synthesized via a nonthermal plasma process.[105, 139] Pure silane gas was introduced into an argon plasma to produce Si atoms while diborane, diluted to 10% in hydrogen, and phosphine, diluted to 15% in hydrogen, introduced dopant atoms. These atoms nucleate and grow into nanocrystals within the plasma region. The dopant incorporation efficiencies were considered to be ~10% and ~50-100% of the fractional dopant flow for boron and phosphorus respectively. Gas mixtures were adjusted to give atomic percentages in the SiNPs of 0.05% and 0.25% boron and 2.5% phosphorus.[96] The hydrogen in which the dopant precursors are diluted may influence the amount of hydrogen at the surface of the nanocrystals. Unfortunately, we are unable to experimentally assess

the role of this relatively small additional hydrogen flow, because hydrogen cannot be independently controlled with our experimental setup. Atomic percentages throughout the text refer to the estimated composition of the synthesized particles. These particles consist of a crystalline core with a 1 nm amorphous shell.[96, 105] The current synthesis produced particles that were nominally 9 nm in diameter. An 8 nm core would contain ~13,400 silicon atoms (d_{Si} = 2.33 g/cm^3) and a 1 nm amorphous shell would contain ~5570 atoms ($d_{Si, amorphous}$ = 2.29 g/cm^3); nearly one third of the atoms in the SiNP are in the outermost shell. Boron and phosphorus doped SiNPs can be plasmonic, but not at the low doping levels studied here.[139] Surface oxidation affected the SiH_x 2D-IR signals, hence, nucleated particles exiting the plasma were deposited directly onto CaF_2 windows and kept under inert atmosphere during transfer to the sample cell. The sample cell was then purged with ultra-high purity N_2 during the entire course of the experiment. A piece of Na metal was also placed inside the sample cell to scavenge any trace water or oxygen that entered the cell throughout the process.

The 2D-IR instrument has been described previously.[41, 80] Here the only difference was that the mid-IR pulses were tuned to the silicon hydride stretching region: ~ 2100 cm^{-1}. Spectral resolution in the 0.32 meter monochromator with a 75 line/mm grating, was again ~ 4 cm^{-1}. Data collection was performed with fibrillation to remove scatter from all three pump beams, as described in Chapter 2.[140] The resulting absolute value 2D-IR spectra were analyzed using peak volumes to extract kinetic information directly from the 2D-IR spectra.[31, 81, 141]

4.3 Results and Discussion

Figure 20 shows the FTIR spectrum for a film of intrinsic SiNPs (black trace). The vibrational features are consistent with those reported for silicon nanowires and quantum dots.[116, 119, 142] The spectrum is complex, exhibiting multiple peaks that have been previously assigned.[143-145] According to work on acid-etched silicon films, fundamental resonances at 2077, 2111, and 2137 cm^{-1} are further split into asymmetric and symmetric
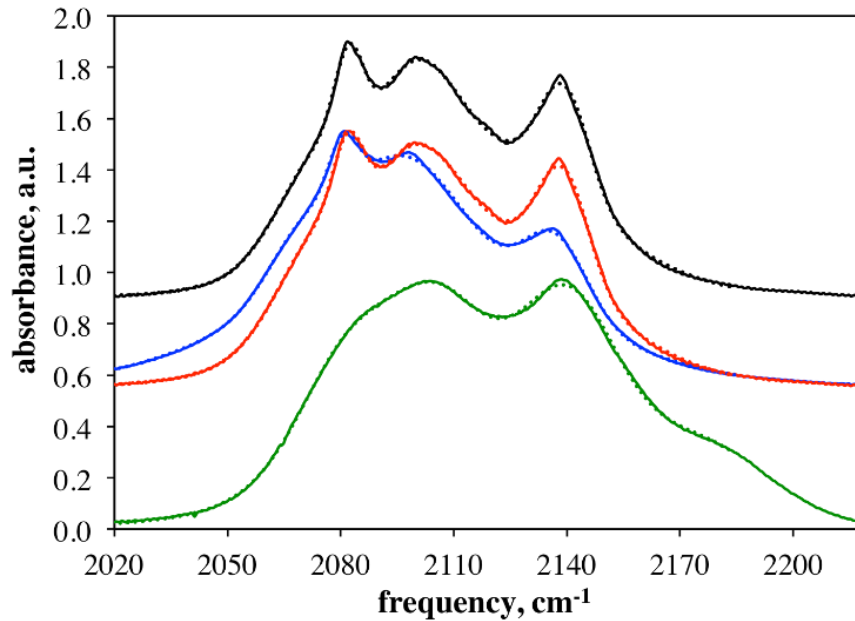
Figure 20: Baselined and normalized FTIR spectra of the SiH$_x$ stretching region for dry films of intrinsic SiNPs (black), 0.05% B-SiNP (red), 0.25% B-SiNP (blue), and 2.5% P-SiNP (green). Overlaid dotted lines show the multi-Gaussian fit results. SiNP, B-SiNP, and P-SiNP spectra are offset vertically for clarity.

bands due to through-bond coupling,[127] leading to silicon monohydride peaks at 2072 and 2083 cm^{-1}, silicon dihydride peaks at 2106 and 2115 cm^{-1}, and silicon trihydride peaks at 2129 and 2139 cm^{-1}. We find that the intrinsic SiNP spectrum in Figure 20 can be readily fit by a sum of six Gaussians with their peak centers constrained to within a few cm^{-1} of these earlier values (the calculated fit is overlaid as a dotted line). Therefore, the FTIR spectrum of the SiNPs captures monohydride terminated silicon species at 2080 cm^{-1}, and dihydride and trihydride terminated silicon atoms around 2100 cm^{-1} and 2135 cm^{-1},
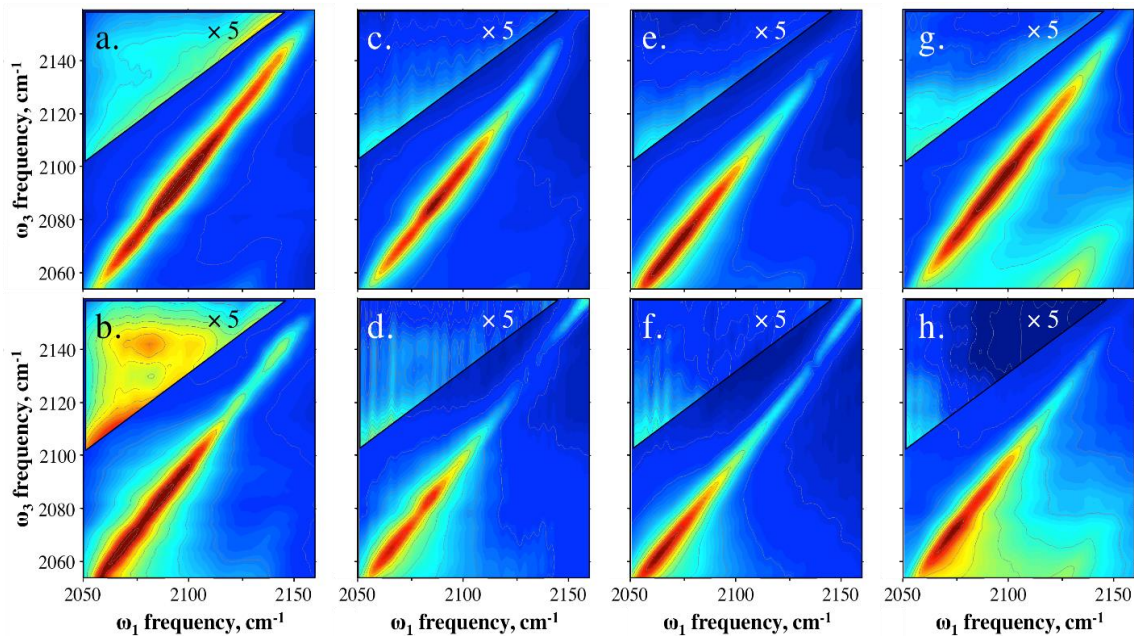
Figure 21: 2D-IR spectra of the silane stretching region at T_w = 1 ps (top row) and T_w = 25 ps (bottom row) for (a and b) intrinsic SiNP, (c and d) 0.05% B-SiNP, (e and f) 0.25% B-SiNP, (g and h) 2.5% P-SiNP. Top left corner of all frames have been magnified × 5 for clarity.

respectively. The trihydride species can only come from a defect or dangling Si-Si bond.[145, 146] A blue shift with added hydrogen atoms was also corroborated by DFT calculations carried out in our lab at the M06l level of theory with a 6-31G(d) basis set on 2-silyl tetrasilane.

Using the fact that the monohydride absorption is only about 41% as strong as the combined polyhydride vibrations,[147] we can estimate from our fitted peak areas that one third of the intrinsic SiNP surface is characterized by monohydride silicon environments, leaving the rest as polyhydrides. Doping of SiNPs with boron (B-SiNP) causes the monohydride proportion of the spectrum to drop to 30% and 18% for 0.05% and 0.25% boron doping, respectively. This is consistent with a view in which the surface hydride vibrations experience an increase in morphological disorder, exchanging monohydrides for polyhydrides and defected sites as doping increases. The same trend is observed upon

doping SiNPs with 2.5% phosphorus atoms (P-SiNP), which decreases the monohydride contributions to 28% (Figure 1, green) and substantially broadens all of the peaks.

2D-IR spectra were collected for these same samples to compare the vibrational dynamics of the mono- and polyhydride surface vibrations (Figure 21). In these spectra, the ω_τ axis was again achieved by scanning τ, in increments of 5 fs while ω_m was the heterodyne detected vibrational echo signal resolved on the monochromator.[41, 80] All eight frames in Figure 21 have a region in the top left corner that has been magnified by a factor of five to make the features more apparent. At a relatively short waiting time of $T_w = 1$ ps, the off-diagonal region connecting the mono- and polyhydride stretches has a small amplitude for the intrinsic SiNP sample but is nearly featureless for the doped samples. Increasing T_w to 25 ps brings the off-diagonal peaks for the intrinsic SiNP sample into focus but has no obvious effect on the doped samples. The 0.05% B-SiNP sample in fact has some increased amplitude upon close inspection. The off-diagonal amplitudes in the Figures 21a and 21b indicate that excitation that was initially in the SiH stretching modes has transferred to SiH_2 and SiH_3 modes on the ps time scale. There is also evidence in this same region for transfer of vibrational energy from dihydride to trihydride modes.

To quantify vibrational energy transfer (VET) between the surface modes of all four particle types, the regions in the 2D-IR spectra corresponding to transfer from SiH to SiH_2 or SiH_3 were normalized by the on-diagonal volumes at their respective emission frequencies (ω_m). The energy transfer is indicated by the off-diagonal features decaying with a longer time constant than the on-diagonal populations and normalization by the on-diagonal peak yields a rise; when VET is absent, normalization yields a constant.[81, 141] Figure 22 shows the normalized off-diagonal peak volume that captures VET between the
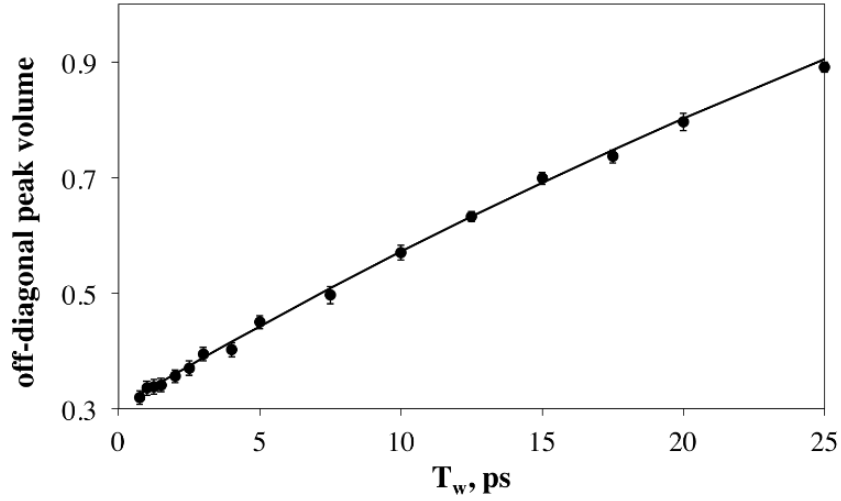
Figure 22: Off-diagonal peak volume (2083 cm⁻¹, 2142 cm⁻¹) normalized by the on-diagonal volume showing VET from SiH₂ and SiH₃ modes on the surface of intrinsic SiNPs.

mono- and polyhydride modes. The best fit results for the time constant in the exponential

rise function are compiled in Table 3 for all four sample types.

modes	SiNP	0.05% B-SiNP	0.25% B-SiNP	2.5% P-SiNP
	τ_{VET} (ps) [a]	τ_{VET} (ps) [a]	τ_{VET} (ps) [a]	τ_{VET} (ps) [a]
SiH₁ to SiH₃	61.7 (±21.3)[b]	19.3 (±8.5)[b]	8.1 (±4.3)[b]	-
SiH₁ to SiH₂	64.0 (±40.9)[b]	37.1 (±17.7)[b]	19.6 (±9.4)[b]	-

Table 3: Best fit parameters for exponential rise time (τ) for VET between silane modes. Error bars represent 95% confidence interval

Functional form of the exponential rise is as follows:

$$\frac{I_{off-diagonal}}{I_{on-diagonal}} = A * (1 - B * e^{-\frac{t}{\tau}}) \qquad (28)$$

The time scale for VET (τ_{VET}) between the monohydride and polyhydride modes on the SiNPs is about 60 ps. For comparison, Kuhnke and coworkers reported previously that the τ_{VET} from Si-H terraces to dihydride step edges on acid-etched single crystal silicon surfaces was 450 ps, but transfer from a mode at 2100 cm^{-1} to 2140 cm^{-1} was notably faster at 30 ps.[133] Likewise, Guyot-Sionnest determined the time scale for transfer between surface modes on Si(100) at 2100 cm^{-1} and 2085 cm^{-1} to be 95 ps at 10 K but faster than 10 ps at room temperature.[128] Given the limited temporal resolution of these previous studies, our measured τ_{VET} values for the undoped SiNPs agree semi-quantitatively with measurements on single crystal systems. VET is not substantially affected by structural differences between single crystal and amorphous silicon. This could be understood with a model in which the amorphous SiNP surfaces contain domains that are enriched with mono- or polyhydride species on some length scale, and the structure between these domains in SiNPs provides similar coupling for VET as those between single crystal faces. This model is consistent with transient grating measurements on amorphous silicon by Rella and coworkers in which the authors concluded that nonexponential relaxation was due to a distribution of hydride environments that did not interconvert on the ultrafast time scale.[136, 138]

We note that the off-diagonal amplitude at longer T_ws is at least a factor of 50 smaller that the on-diagonal amplitude at short T_ws. In 2D-IR spectra, mode coupling is observed directly in the off-diagonal region as the energy difference between a positive and negative going peak pair.[31, 81, 141] When coupling is very weak, these peaks are coincident leading to cancellation. We interpret the weak off-diagonal peak amplitudes in our spectra to mean that many of the monohydride modes are decoupled from polyhydride

modes; only a small number of modes remain sufficiently coupled to give measurable off-diagonal amplitude. This further supports a model of the heterogeneous SiNP surface as being composed of domains that are enriched in a particular hydride mode type, where VET occurs only at the boundaries between domains that are enriched in a particular mode type.

Although the FTIR spectra of 0.05% B-SiNPs and intrinsic SiNPs are quite similar in Figure 20, the effect of dopant atoms on VET is dramatic. With the inclusion of only about ten boron atoms per nanoparticle, there is notably less energy transferred (Figures 21c and 21d). By the inclusion of 0.25% boron atoms (~50 atoms per particle), VET becomes so weak that it is difficult (but still possible) to characterize; about 500 phosphorus atoms turns it off completely! The τ_{VET} values from SiH_1 to SiH_3 modes decrease from 62 ± 21 ps for intrinsic Si to 19 ± 9 ps for 0.05% B doping and down to 8 ± 4 ps for 0.25 % B doping (Table 3). Exchange from SiH_1 to SiH_2 shows a similar trend. Since only the amorphous shell of the particles is hydrogenated, localization of dopant atoms to the outer 1 nm region would amplify their impact on VET. This effect would be further amplified by the SiNP surface model described above with domains enriched with a particular type of SiH_x vibration, leaving only the boundaries between these domains as sites for exchange. A small number of dopant atoms could preferentially occupy the inter-domain sites in the amorphous shell of the SiNPs and disrupt vibrational coupling.

It remains to be explained how the surviving VET in B-SiNP samples is statistically faster than for intrinsic particles. The coupling constant for two transition dipoles scales as the inverse distance to the 3rd power, making the coupling between SiH_x modes highly sensitive to their separation. It is known that Si—Si bonds are 2.3 whereas Å B—Si bonds

are 2.1 Å, which would bring adjacent hydride vibrations into closer proximity.[148] At the same time, it is known that boron forms only three bonds while silicon forms four, therefore we expect that there will be a decrease in lattice connectivity by the inclusion of B dopants. The data in Figure 21 indicate that the structural disruption of including boron dopants shuts down communication between a large fraction of the coupled surface modes, consistent with a dramatic reordering of the surface morphology. Yet, for a small number of modes that are adjacent to the dopant site, a higher rate of VET results from closer proximity and therefore stronger coupling. If VET occurs by through-bond and through-space pathways, then it is conceivable that the introduction of dopants at inter-domain regions disrupt through-bond VET. But the decrease in distance between dipoles would increase the rate of through-space transfer allowing the surviving VET to appear faster.

The vibrational lifetimes (T_1) for different hydride modes are readily obtained by fitting separate regions of the on-diagonal 2D-IR peak volumes to exponential decays. Figure 23 shows that all mono- and polyhydrides have T_1 values of ~7 ps for intrinsic SiNPs. This lifetime is two orders of magnitude faster than the T_1 reported for SiH_1 of 500-800 ps on single crystals at room temperature,[130, 149] and one order of magnitude faster than the dihydride T_1 on single crystals at room temperature.[133] Vibrational relaxation dynamics are faster in amorphous silicon, but have been reported to be non-exponential with an average T_1 of 60 ps in one case,[135] and biexponential in another giving $T_1 = 20$ and 100 ps for the SiH and $T_1 = 13$ and 50 ps for the SiH_2 vibrations.[137] Porous silicon dynamics were reportedly single exponential and intermediate to this latter report at 22 and 83 ps for the SiH and SiH_2 modes, respectively.[134] In our measurements, extraction of T_1 from on-diagonal 2D-IR peak volumes reveals the population relaxation for different hydride states

free of convolution with exchange and intramolecular vibrational redistribution.
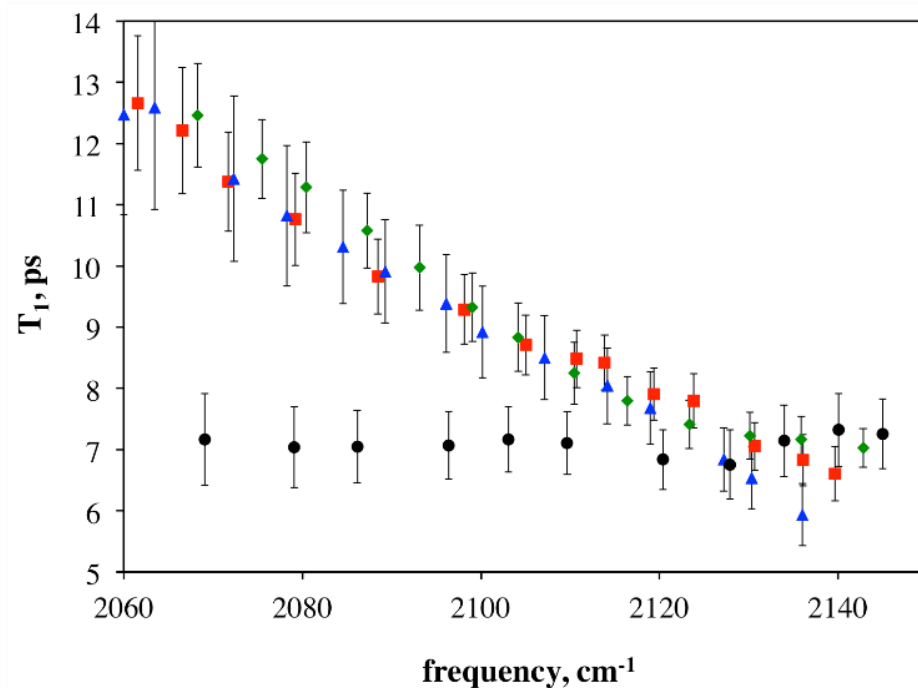
Figure 23: Vibrational lifetimes (T₁) as a function of frequency across the silicon hydride stretching region for intrinsic SiNPs (black circles), 0.05% B-SiNPs (red squares), 0.25% B-SiNPs (blue triangles), and 2.5% P-SiNPs (green diamonds). Error bars represent 95% confidence interval.

Therefore, the population dynamics (7 ps) and exchange dynamics (60 ps) for intrinsic SiNPs would give biexponential behavior in the pump-probe projection but with time constants that would be difficult to differentiate due to their similar time scales and population relaxation occurring on a shorter time scale than exchange. This behavior is most consistent with vibrational dynamics for amorphous silicon.

Interestingly, all doped SiNPs in Figure 23 show that T_1 decreases with increasing wavenumber. The SiH and SiH$_2$ modes relax more slowly while the SiH$_3$ mode remains the fastest. The τ_{VET} values in Table 3 are too slow to be competitive with VER, therefore we cannot conclude that the decrease in intermode communication with doping enables relaxation to be independent. Instead, the frequency dependence in Figure 23 must be due to structural perturbations that affect the density of states or coupling to lower energy

74

modes and phonons in different ways for the different enriched domains on the SiNP surface. The fact that doping affects different domains differently was also reflected in the disproportionate changes observed in the mono- and polyhydride modes in the FTIR spectra in Figure 20.

The frequency independence of T_1 for intrinsic SiNPs is surprising. Jobson reported that the 2114 cm^{-1} mode in porous silicon relaxed four times faster than the mode at 2083 cm^{-1}.[134] Likewise, several groups have shown a decrease in T_1 with increasing wavenumber for amorphous silicon.[136, 137] Figure 23 shows that doping with boron or phosphorus revives the frequency dependent behavior observed in porous and amorphous silicon. This highlights the fact that, despite some dynamic similarities to amorphous and porous silicon, structural differences exist in the amorphous shell of intrinsic SiNPs that lead to unique relaxation behavior of their hydride modes. From the perspective of controlling surface reactivity in silicon-based electronics by controlling vibrational relaxation,[129] the results show that measurements on bulk silicon materials are not readily extrapolated to nanoparticles.

4.4 Silicon Nanoparticles Conclusion

2D-IR spectroscopy provides the first measurement of VET between hydride modes in the amorphous coating on SiNPs. Despite the increase in heterogeneity that is inherent in amorphous silicon, we find that the rates of VET are consistent with those measured on homogeneous single crystal facets and step-edges. Although the FTIR spectra of the nanoparticle films show only minor changes, we find that the vibrational dynamics are exceedingly sensitive to doping by boron and phosphorus atoms. Intrinsic SiNPs show weak VET between mono- and polyhydride modes as well as frequency independent

vibrational relaxation. Incorporation of dopants eliminates off-diagonal exchange, isolating the respective hydride stretching modes and rendering T_1 frequency dependent. The effects of doping on T_1 and exchange kinetics can be explained by structural disruptions caused by dopant localization at boundaries between domains that are enriched with mono- or polyhydride modes. The sensitivity of vibrational dynamics to small amounts of dopants explains why the electronic behavior of these materials may be highly variable even when steady-state characterization methods show that they are uniform.

Chapter 5 2D-IR of gas phase carbon dioxide

5.1 Introduction

Before the final chapter investigating gas adsorption and doping in nanoparticle thin films, it behooved us to measure a gas phase species. Thus 2D-IR was applied to carbon dioxide in a dilute gaseous state under ambient pressure and temperature. Interestingly there is strong correlation of quantum mechanical states during the vibrationally excited state period with minimal J-state scrambling. This is consistent with the relative infrequency of collisions under these conditions. Fitting the peak positions of the off-diagonal features in the 2D-IR spectra enables one to determine the rotational and rotation-vibration interaction constants with high fidelity by matching the curvature of these features rather than spectrally resolving the individual peaks. The predicted off-diagonal peak splitting is also confirmed in higher resolution 2D-IR spectra, which provides an alternate route to obtaining rotational constants of gas-phase species, albeit slightly less accurate.

The role of CO_2 in the atmosphere and industrial processes has motivated a plethora of experimental and computational studies aimed at understanding its behavior under a wide-range of conditions.[150-154] Despite the depth of literature that already exists, many properties of CO_2 are not yet fully understood, specifically its behavior at high temperatures and pressures when confined to the nanoscopic volumes of a storage medium. A number of spectroscopic methods can be used to address these questions, most of which determine the average structures of molecules and molecular clusters.[155-158] The ensemble averaging inherent to these approaches makes it challenging to extract the time scales on which individual structural configurations interconvert; gas-phase dynamics are typically

obtained by lineshape analysis.[159] Recently, Mandal and coworkers demonstrated that 2D-IR could be used to monitor dynamic processes in the asymmetric stretching vibration of N_2O under 17 and 25 atm of sulfur hexafluoride (SF_6).[160] In this moderately dense medium, the peculiar 2D-IR spectra showed interconversion of P- and R-branch species with rotational quantum numbers conserved. Within ten picoseconds, the J-quantum numbers became scrambled by just a few molecular collisions causing the 2D-IR spectra to resemble those of the condensed phase. This level of detail about the molecular dynamics was not otherwise attainable by linear spectroscopic methods.

In the current work, we contribute to this body of knowledge by reporting the 2D-IR spectra of CO_2 under ambient pressure (1 atm) and temperature (294 K). We show that rotational quantum numbers are also conserved for this system for over 100 ps with minimal scrambling of J-states. We further demonstrate that the curvature of off-diagonal peaks in the 2D-IR spectrum can be used to obtain reasonable rotational constants and anharmonic correction terms without the need for a high-resolution IR instrument. This study highlights the applicability of 2D-IR spectroscopy to gas phase molecules and clusters, and, perhaps more importantly, provides a baseline for future multidimensional IR studies of CO_2 at higher pressures and temperatures, and in more complex environments.

5.2 Experimental

The sample cell consisted of two 3 mm CaF_2 windows separated by a 1 mm spacer. CO_2 was diluted in high purity N_2 and flowed continuously through the cell during the measurements. The typical optical density for samples studied was 1.5 mOD at the peak of the P(2) rotational-vibrational band in the CO_2 asymmetric stretching band. Using the

absorption coefficient for CO_2 at 300 K of 0.025 $Pa^{-1}m^{-1}$ (or 2.53 $atm^{-1}mm^{-1}$),[161] we can estimate that the partial pressure of CO_2 is 0.0006 atm. The total cell pressure was approximately 1 atm as the output flow was only resisted by an oil bubbler indicator.

The 2D-IR instrument in this instance had mid-IR pulses tuned to the CO_2 asymmetric stretching region of ~ 2340 cm^{-1}.[41, 80] The generated vibrational echo signal coaligned with the LO was resolved on a 75 or 150 line/mm grating for ~ 4 cm^{-1} and 2 cm^{-1} respectively. The entire instrument was sealed and purged with dry N_2 to eliminate absorbance of IR beams by atmospheric CO_2. Without purging at these frequencies, 90% of the incident beams was absorbed causing complete loss of signal.

5.3 Results and Discussion

Figure 24 shows the 2D-IR spectra of CO_2 at short (1 ps) and long (100 ps) Tw's. The FTIR spectrum of CO_2 is also shown at the top of each 2D-IR plot to connect to the familiar rotational-vibrational P- and R-branches resulting from $J - 1$ and $J + 1$ transitions during a $v \pm 1$ transition.[159] Due to molecular symmetry ($D_{\infty h}$) and spin statistics,[159] only rotational transitions from even J states are allowed for CO_2, causing the P- and R-branches to only show every other transition starting with P(2) and R(0), respectively. Similarly, the peak spacing within each branch is given by 4B instead of the typical 2B, where B is the rotational constant, and the P(2) and R(0) peaks are separated by 6B instead of the usual 4B due to the absence of the P(1) peak.[159, 162]
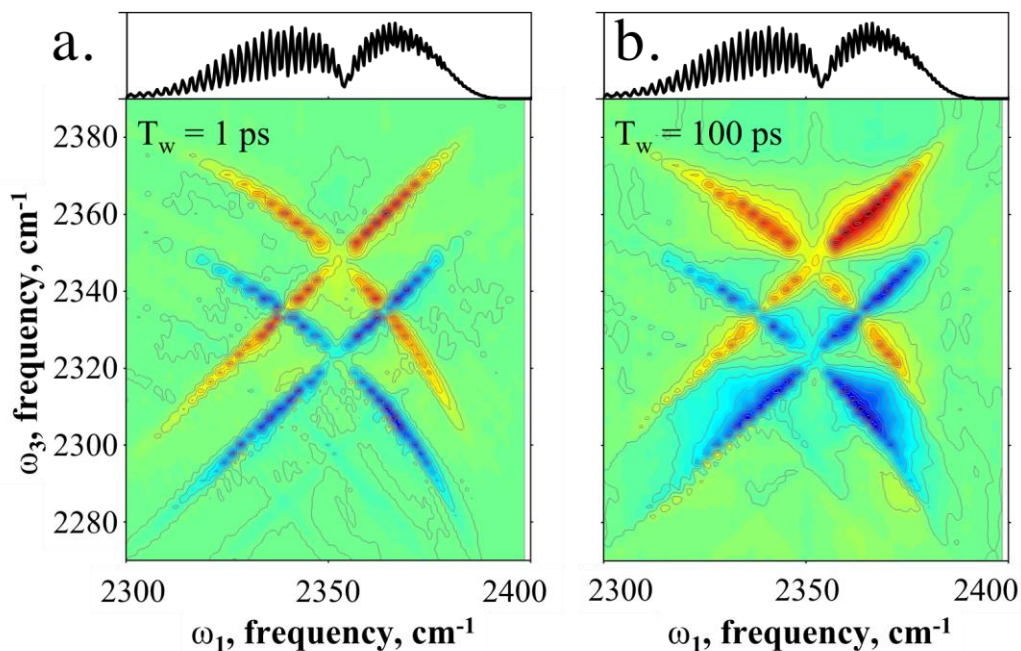
Figure 24: 2D-IR spectra of CO_2 at 6×10^{-4} atm diluted in N_2 to 1 atm at a) T_w = 1 ps and b) T_w = 100 ps. Above each frame is the FTIR spectrum of CO_2 for reference.

The 2D-IR spectra exhibit a series of positive-going (red) peaks aligned with the plot diagonal at the P- and R-branch frequencies, corresponding to ground state bleach pathways in which molecules are excited and emit in the same branch. These pathways are shown diagrammatically in Figures 25a and 25b. Also visible in Figure 24 is a series of negative-going (blue) peaks arising from excited state absorption that are diagonally-aligned but shifted to lower ω_3 frequencies by the vibrational anharmonicity of 24 cm^{-1}. Due to the limited spectral resolution of the 2D-IR spectrometer, not all of the vibrational ground state bleach and excited state absorption peaks predicted by the FTIR are resolved.
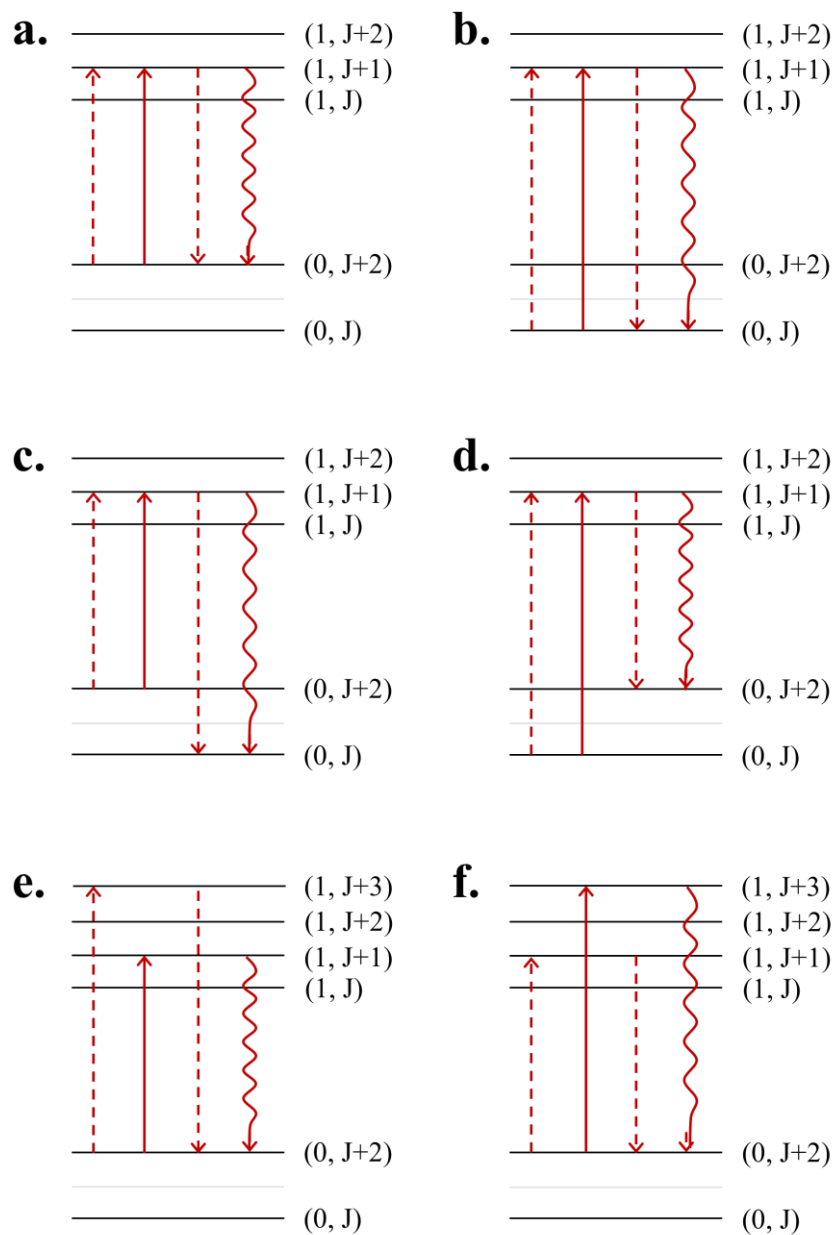
Figure 25: Six selected density matrix pathways (of 36 total) leading to 2D-IR signals for (a and b) P- and R-branch ground state bleach, (c and d) P- and R-branch population exchange, and (e and f) P- and R-branch coherence exchange. Straight arrows indicate an interaction of the system with an IR pulse on either the bra or ket side of the density matrix (solid and dashed arrows); wavy lines indicate vibrational echo emission from the system.

In the antidiagonal direction, the characteristic "x" pattern is observed, as reported by Mandal and coworkers for N_2O indicating J-state conservation.[160] One process that can lead to off-diagonal peaks is excited state population exchange during T_w (shown diagrammatically in Figures 25c and 25d). The same rotational-vibrational state $|v, J\rangle$ can

81

be reached by two pathways defined by the P- and R-branches when the system interacts with the first two pulses in the 2D-IR pulse sequence. Assuming this state is preserved during the T_w period, the $|v, J\rangle$ state can likewise be stimulated to emit a vibrational echo by two pathways back to the ground vibrational state. For example, the system can be excited from $|0, 0\rangle$ or $|0, 2\rangle$ to $|1, 1\rangle$ via the R(0) and P(2) transitions, and then emit from that state back to the two starting states. In this case, excitation to $|1, 1\rangle$ via the P-branch followed by emission from $|1, 1\rangle$ in the R-branch results in an off-diagonal peak.

In a moderately dense medium, the initially prepared state can experience changes in J by molecular collisions that result in lineshape coalescence.[160] However, the current study is carried out at ambient pressure and temperature where the average collision time is ~200 ps. There is weak evidence of this broadening after 100 ps in the first few contours of the 2D-IR plot (Figure 24b). Figure 26 shows that summing the intensity in these off-diagonal contours and normalizing by the on-diagonal intensity[31, 81] over a range of T_ws reveals a monotonic increase due to J-scrambling. The plot lacks sufficient curvature to determine the time constant for this process with any reasonable precision, but we note that given the exceedingly long vibrational relaxation times in the gas-phase one could directly measure these dynamics using an instrument with longer delay times. Overall, we find that quantum states are preserved for the majority of the oscillators on our time scale in this diffuse gas mixture over the first 100 ps.
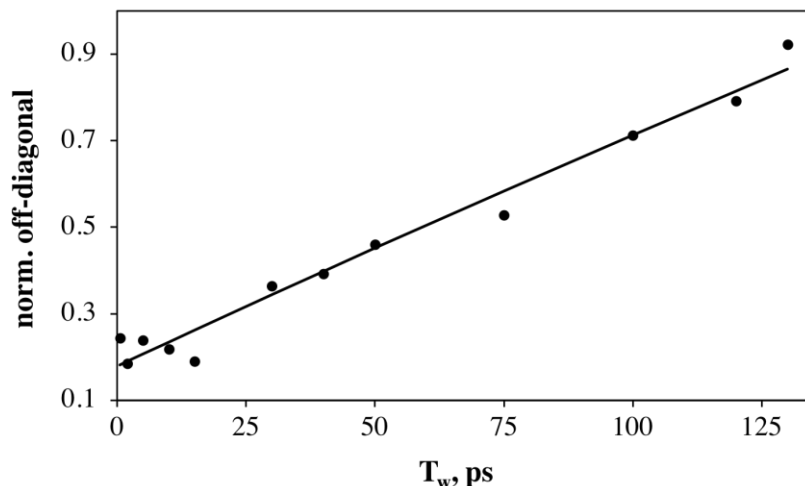
Figure 26: Off-diagonal intensity for the v=0-1 transition normalized by on-diagonal intensity at the emission frequency as a function of T_w.

Unlike the diagonally-aligned peaks that form straight ridges, the antidiagonally-aligned peaks in Figure 24 arrange with a downward curvature. Equations 29 and 30 show the well-known equations predicting peak frequencies in the P- and R-branches:[159]

$$\nu_P(J) = \nu_0 - 2J\, B_e - J\,(J - 2)\alpha_e \qquad (29)$$

$$\nu_R(J) = \nu_0 + 2(J + 1)B_e - (J + 1)(J + 3)\alpha_e \qquad (30)$$

These equations are written in terms of an the equilibrium rotational constant, B_e, adjusted by the rotation-vibration interaction constant, α_e, that adjusts the rotational constant, B_v, for each vibrational quantum state, v:

$$B_v = B_e - \alpha_e\left(v + \frac{1}{2}\right) \qquad (31)$$

The α_e-dependence causes the peak frequencies to get closer as J increases in the R-branch and to get farther apart as J increases in the P-branch. However, since J increases toward negative and positive frequencies in the P- and R-branches, respectively, both branches exhibit peaks that get closer as you move to higher frequency. Figure 27 shows a simple schematic of a spectrum with P- and R-branch peaks getting closer from left to

83

right and the 2D-IR peak positions that would result on- and off-diagonal. The trend of peak spacing in the two branches with increasing frequency leads to the downward curvature that is observed in Figure 24. This is a direct result of the influence of vibrational
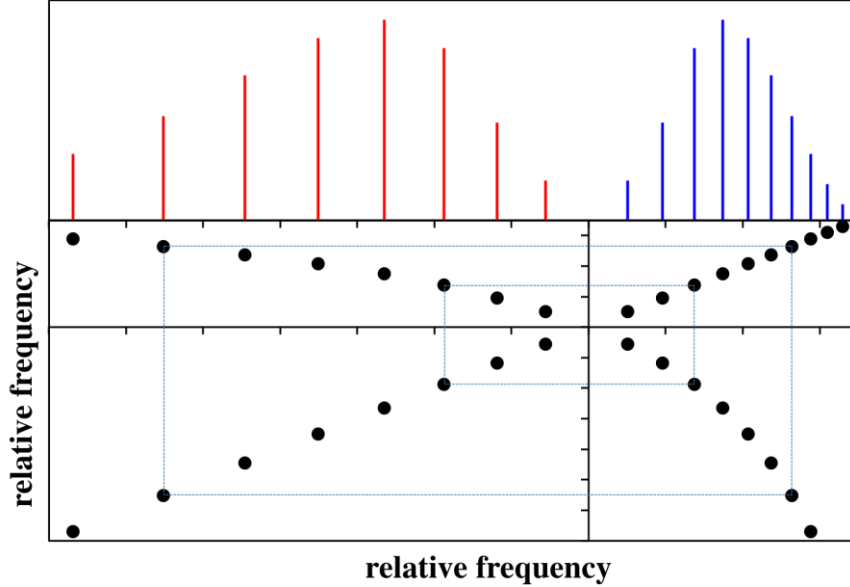
Figure 27: Schematic of a typical rotational-vibrational spectrum in which the transition spacing decreases in both P- and R-branches toward higher frequencies. The lower frame shows the resulting off-diagonal peaks that occur with downward curvature, as seen in experimentally in Figure 24.

excitation on the rotational constant.

The off-diagonal peaks in the 2D-IR plot appear at the (ω_1, ω_3) coordinates, where the x- and y-axis values in quadrant II (upper left) are given by Equations 29 and 30, respectively; the x- and y-axis values in quadrant IV (lower right) are given by Equations 30 and 29, respectively, each for a particular rotational quantum number. One can construct Equation 32 that gives the y-coordinate as a function of an x-coordinate in these off-diagonal quadrants, thereby defining a curve that can be used to fit experimental 2D-IR data.

$$\omega_3 = \nu_0 + 10B_e + 4CB_e - 6\alpha_e C - \frac{3B_e^2}{\alpha_e} - 8\alpha_e - \alpha_e C^2 \qquad (32)$$

where:

$$C = \sqrt{\left(1 - \frac{B_e}{\alpha_e}\right)^2 - \left(\frac{\omega_1 - \nu_0}{\alpha_e}\right)} \qquad (33)$$

Equation 32 gives the off-diagonal values for ω_3 as a function of ω_1 on the 2D-IR axes. The peak positions in these coordinates were determined by fitting vertical slices across the data at $T_w = 1$ to Gaussian curves to identify the maxima, which are plotted in Figure 28. Equation 32 was then fitted to these data using ν_0, B_e, and α_e as adjustable parameters. The largest uncertainty in the fits came from the calibration of the y-axis values in the 2D-IR instrument, which are typically accurate to within a 1-2 cm^{-1}. Therefore we used the crossing point of the on- and off-diagonal ridges (2351 cm^{-1}) as ν_0 and allowed B_e and α_e to float in the fitting procedure, giving $B_e = 0.39$ cm^{-1}, $\alpha_e = 0.0029$ cm^{-1}. These are within 0.1% and 7% of the literature values for B_e and α_e, respectively.[163, 164] In the absence of α_e there is no curvature in the off-diagonal regions. However, the effect of this anharmonic correction term is amplified by terms in which it is a product with B_e. The important aspect of this analysis is that these rotational-vibrational parameters can be determined with reasonable accuracy from a 2D-IR plot without the spectral resolution to resolve the rotational-vibrational peaks by simply fitting the curvature of the off-diagonal peaks.
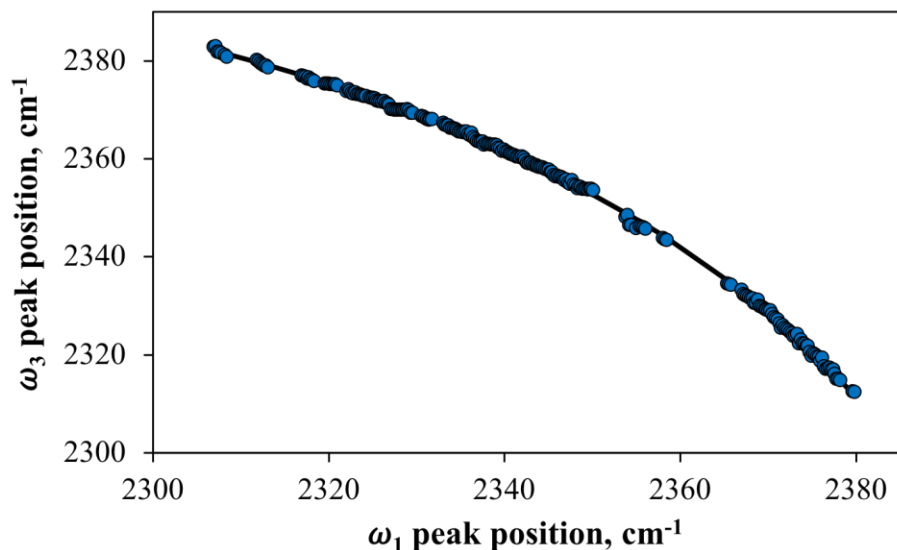
Figure 28: Off-diagonal peak positions extracted from the 2D-IR spectrum at Tw = 1 ps overlaid with Equation 4 (solid black line) using the best fit parameters: ν_0 = 2351 cm^{-1}, B_e = 0.39 cm^{-1}, α_e = 0.0029 cm^{-1}.

The 36 quantum pathways that are possible in a four wave mixing experiment were reported previously.[160] The four pathways that lead to positive-going on- and off-diagonal signals were reproduced in Figure 25a-25d above. In addition to the vibrationally excited state populations that can be prepared, 2D-IR is also sensitive to the rotational-vibrational coherences that can be prepared (i.e. Figures 25e and 25f) that are not observed by FTIR spectroscopy. After the T_w period, the P/R coherences can be stimulated to emit at either a P- or R-branch frequency, producing a new pair of off-diagonal peaks in quadrants II and IV. For example, excitation by the first interaction at the P(2) transition frequency could lead to echo emission at R(0) (Figure 25c) or R(2) (Figure 25f). To a first approximation assuming B_e is orders of magnitude larger than α_e, these off-diagonal peaks are separated by $4B_e$. Figure 29 shows that we can in fact resolve these peak pairs using a higher resolution grating at the detection side of the 2D-IR instrument. The peak separation here is 2.24 cm^{-1} on average, corresponding to B_e = 0.56 cm^{-1}; not as precise as the value

obtained by fitting the curvature of the full off-diagonal dataset but still within a factor of two.
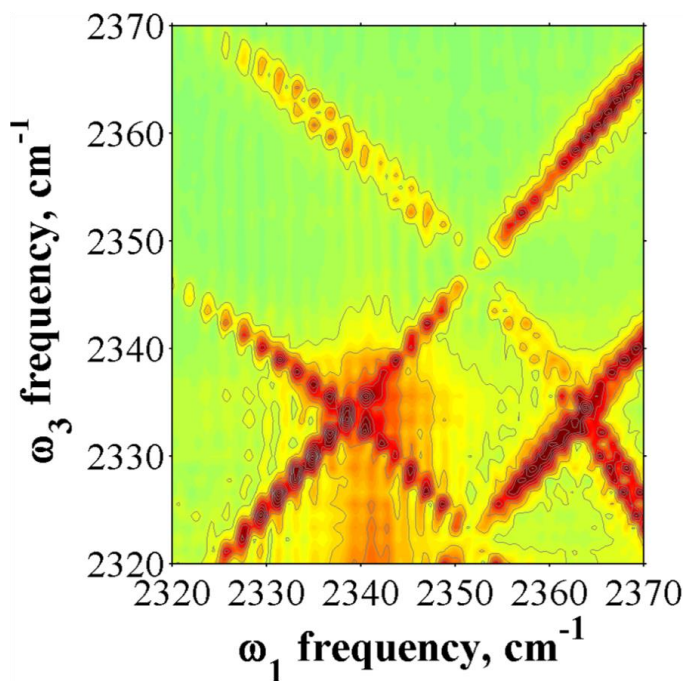
Figure 29: Absolute value 2D-IR spectrum at $T_w = 1$ ps for CO_2 gas measured with a higher resolution diffraction grating to identify peak twinning in the off-diagonal quadrants

5.4 Gas Phase CO_2 Conclusions

Studying the structure and dynamics of small molecules such as CO_2 in the gas phase provides the requisite details to model and predict chemical separations in industrial processes and reactivity in the Earth's atmosphere. Measuring dynamics on the ultrafast time scale that governs collisions in dense media and nanoscopic environments poses a unique challenge that can be met by 2D-IR spectroscopy. Herein, we have demonstrated the 2D-IR spectra of CO_2 under ambient temperature and pressure, highlighting the unique spectral features that result from conservation of quantum mechanical states. The loss of coherent states by collisions is nearly inaccessible due to the long time between molecular collisions, however, data analyses shows that rotational constants for gas phase species can

be obtained with high fidelity without a high resolution instrument. The results presented in this study highlight the utility of the multidimensional approach and provide a baseline for future work on gas-phase molecules in more complex environments.

This work was performed as a basis for CO_2 gas in nanoscopic films. At this point given the exchange, nanoparticles, and gas phasye studies by 2D-IR we were well equipped for the work presented in the final chapter. This work involves gaseous iodine which is not IR active but all components of the final system have been studied even if they do not directly give rise to 2D-IR signal.

Chapter 6 Bridging the Gap Between the Molecular and Thermodynamic.

6.1 Introduction

Preliminary work on cis-diisothiocyanato-bis(2,2'-bipyridyl-4,4'-dicarboxylic acid) ruthenium(II) (N3) was aimed at measuring ground state CT through a self-assembed monolayer (SAM) of the well-known dye molecule. Subsequent measurements of the N3 analogue, cis-diisothiocyanato-(2,2'-bipyridyl-4,4'-dicarboxylic acid)-(2,2'-bipyridyl-4,4'-dinonyl) ruthenium(II) (Z907), were meant to be a comparative study allowing observation of the effects that variation in vibrational environment has on CT. The electronic and vibrational environment perturbations affecting potential CT were assumed to be decoupled as the NCS ligands were hypothesized to be the sites of somewhat localized hole transfer.[165] This was true for a variety of ruthenium dyes on the surface of a TiO_2 nanoparticle film and reasonable conductivity meant CT might be measurable for our purposes.[165] This project's ultimate goal was to find general principles that would govern rational design of organic conductors with respect to their vibrational environment and dynamics. Though CT was not ultimately measured, its pursuit led to work presented in this chapter. Theory relating to CT is presented in Appendix A.

The system proposed for research is a Graetzel type system, which is a SAM of molecules bound to the surfaces of TiO_2 nanoparticles in a sintered film; a dye-sensitized solar cell (DSSC).[165-168] This system was chosen for a variety of reasons beyond potential CT measurements. First and foremost is the heterogeneity of the films, based on the motivation to study commercially and industrially viable films that are often associated with heterogeneity. The second reason is that the platform lends itself to comparative

studies by means of attaching different molecules to the surface. Molecules bind to TiO_2 easily in solution via carboxylate moieties. Titanium dioxide is also a common substance utilized in many applications.[169] Substrates other than TiO_2 have been studied in Graetzel type systems but the focus here was versatility of the adsorbents in the SAMS and the potential of eventual study of TiO_2 properties in concert with this.[170] Adsorbents or "dyes" of many varieties have SCN ligands which interact strongly with iodine. This made possible the measurement of gas adsorption and exchange.

Previous experiments used computation to verify results. In the case of Shvo it was most useful for comparing the FTIR spectra of the variety of analogues. Explaining the 2D-IR results would have been extremely difficult without computation. Chapter 4 mentioned calculations of FTIR modes carried out on a series of molecules containing SiH_x moieties for the SiNP work. In this chapter the use of MD calculations and the resultant structures with their vibrational frequencies are used to explain more of the observations in 2D-IR spectra in greater detail and to connect these observations to calculated molecular fluctuations. Molecular fluctuations refer to the atomic displacements during MD calculations. A variety of experimental results for N3 (Figure 30, right) and Z907 (Figure 30, left) are included. Computational and experimental results are in excellent agreement for N3@TiO_2 and beckon for an expanded computational approach.

6.2 Experimental Details

All experiments were performed with molecules chemisorbed to TiO_2 nanoparticle films. Nanoparticle suspensions containing 10 nm particles were used as purchased from

Dyesol. Films were doctor bladed onto CaF_2 windows which are inert and transparent to IR light. Doctor blading means spreading thin and smooth using a flat instrument. Dyes (Figure 30) were used as purchased from Solaronix. The films were sintered using a Corning PC420D hotplate by heating at temperatures from 358 K to 773 K in 35 K increments for 20 min at each temperature. A stream of N_2 was maintained over the sample during the process. Films were sintered for uniformity and to burn away the organic surfactants in which the nanoparticles are suspended. Afterwards the films were soaked in a solution of approximately 0.6 mM dye in 1:1 tert-butanol:acetonitrile for 24 hrs. After soaking, copious amounts of acetonitrile were used to wash the film to ensure only chemisorbed N3 or Z907 was present. Films without dye were characterized by AFM at the UMN Characterization Facility on an Agilent 5500 environmental Scanning Probe Microscope and compared to similar films in the literature as a sanity check. The data shows the agglomeration of nanoparticles (Figure 32). This film morphology is comparable to literature reports (Figure 31). [171]
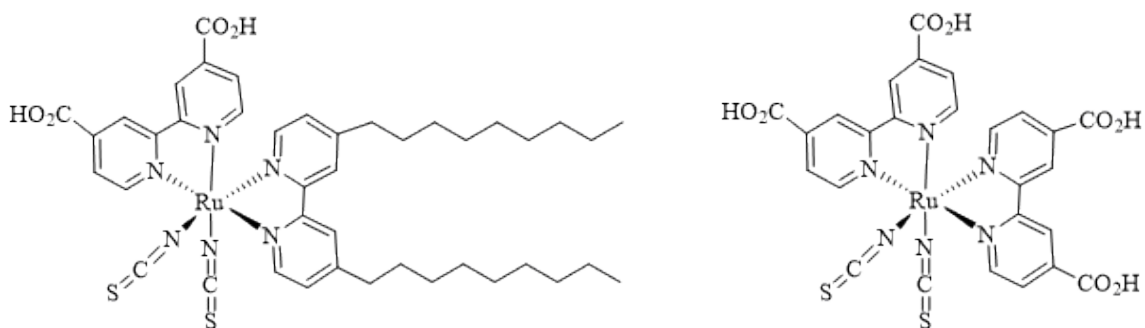
Figure 30: Ruthenium dyes from Solaronix shown with Z907 on the left and N3 on the right.

From film images it is clear that a distribution of void spaces exists giving a distribution of intermolecular distance for molecules on the surfaces of adjacent nanoparticles. The previous nanoparticle surface studies on SiNPs elucidated the amorphous nature of the surfaces of NPs. Even on a crystalline rutile TiO_2 surface there are more than 10 binding configurations for a Ru molecule with four carboxylate groups.[172] This means that there is likely a plethora of nearest neighbor binding types, intermolecular separations, relative molecular orientations, and therefore the chemical environment about
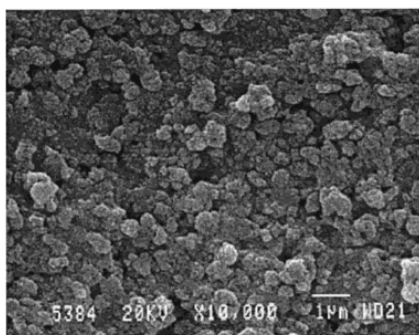
C: AK1 particles of 15 nm diameter

Figure 31: An SEM image from reference 149 in agreement with AFM images of films used.
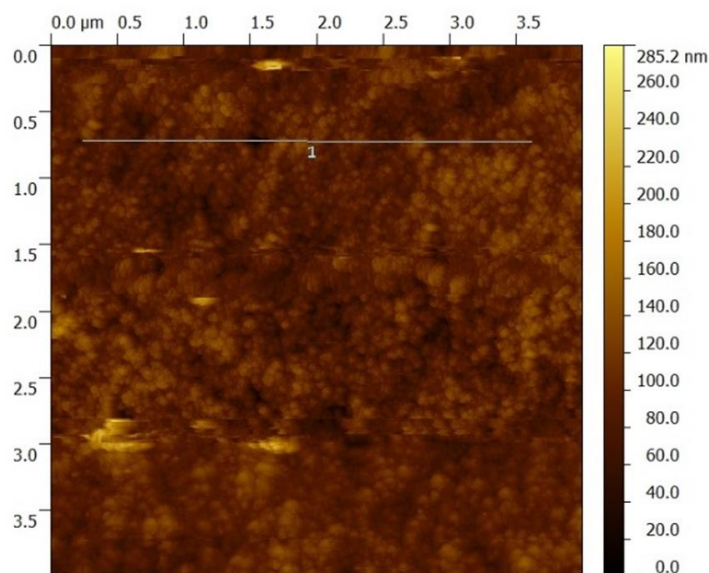
Figure 32: An AFM image of a TiO2 film. Domains or aggregates appear to me terminated by 100 nm diameter aggregates.

92

the SCN ligands observed using 2D-IR. Completely modeling the entire system with a level of detail that captures the heterogeneous effects is an intractable computational task and so computations in the following pages reflect an approach enough to explain 2D-IR observations but are by no means complete.

6.3 Computational Details

Gas phase calculations of N3 were performed at a variety of levels of theory (table 4). Benchmark calculations were carried out on N3 at the B3LYP, PBE, and MO6l levels of theory. Basis sets were varied to investigate their effect on vibrational frequencies. While the level of theory changes the IR frequency of the SCN stretch, it did not appear to be affected by basis set on either metal or nonmetal atoms. Molecular dynamics calculations were carried out on N3 and Z907 at the MO6l level of theory with a 6-31g(d) basis set on all atoms except Ru which had a LANL2DZ basis set and core potential. Molecular dynamics calculations were carried out with a solvent (ethanol) included as a dielectric continuum. A solvent was included as the stability of the Z907 calculations was poor without it. A variety of calculations carried out on Z907 without a solvent failed to converge and resulted in unrealistic geometries in which the coordination geometry was very far from octahedral. In addition to difficulty optimizing structures there was also dissociation of NCS ligands in gas phase MD calculations. To make results comparable both N3 and Z907 were modeled in the presence of ethanol.

For interactions of iodine with N3, a number of configurations were carried with the addition of an iodine molecule. Calculations on N3 in various ionization states were also carried out to determine if charge injection to TiO2 was occurring or if the iodine was undergoing a redox reaction with N3. The only configuration that reflects the blue-shift of

N3 upon iodine addition (Figure 33) is when I$_2$ is associated between a carboxyl proton and the sulfur atom of the NCS ligand. All other configurations resulted in red shifts. These calculations give us some confidence that the iodine interacts with the carboxyl region of N3.

Following completion of MD calculations, the total energy as a function of time was used to select certain structures (Figure 34, Table 5). Table 5 indicates the time steps that were chosen. Molecular dynamics calculations were carried out for 0.88 ps for N3 and 1 ps for Z907. Structures were chosen from total energy local minima, local maxima, and the average or center of these. The assumption is that sampling minima, maxima, and center points would sample the range of atomic displacements. These structures then had only the NCS ligand atom geometries optimized. This had to be done so that frequency calculations could be performed. If the atomic geometry of these ligands had not been optimized this would have resulted in them not being in the bottom of the parabolic potential and the frequencies would have been erroneous.

Finally, the initially and fully optimized structures had frequencies recalculated in the range of solvents that Gaussian has to offer. These were all included as dielectric continuums with each having its own dielectric constant. What was expected is that the MD calculations would result in a frequency spread that would mimic the antidiagonal or homogeneous line width of the 2D-IR spectra. This assumes MD calculation geometries reflect the natural environments that a large ensemble of molecules would exist in. The range of dielectric constants are meant to simulate the range of film environments due to heterogeneity and should result in a range of IR frequencies that account for the additional diagonal linewidth in the 2D-IR spectra.

6.4 N3 FTIR and Comparative Computation

Below are the two FTIR spectra of N3 that dictated the first computational pursuits. When N3 is chemisorbed to TiO_2 nanoparticle films in air the absorbance maximum is at 2112.7 cm^{-1} and when gaseous iodine is introduced to saturate the film the absorbance maximum is at 2132.0 cm^{-1}. Ideally computations would reproduce the observed frequency shifts in the FTIR upon I_2 addition. Thus N3 was optimized at a variety of levels of theory and basis sets. Below is a table of the results (Table 4). Scale factors applied to IR frequencies are taken from Donald Truhlar's website.[173]
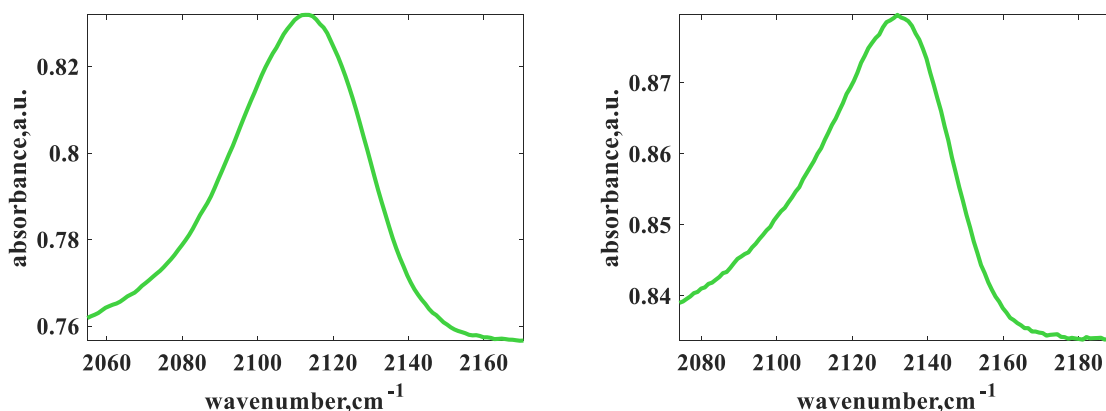
Figure 33: Left is an FTIR spectrum of N3@TiO2 taken June 10th 2013 prior to submerging in DCM and DCM with I2. The max absorbance is at 2112.7 cm-1. Right is N3 saturated with gaseous I2 taken June 7th 2013. The max absorbance is at 2132.0 cm-1.

Benchmark calculations

Below shows the benchmark calculations for vibrational frequency. From Table 4 there is not a clear choice as to which functional is best. All functionals use a 6-31G(d) basis set for nonmetal atoms. Including more basis functions did not change the NCS ligand frequencies so the smallest reasonable basis set was used in anticipation of further and more expensive calculations. Though B3LYP is the only functional that has a known scaling factor for the basis set used, it is

Molecule	Environment	Method	Mode	Intensity	Wavenumber	Scaled
N3 Neutral	Gas Phase	B3LYP	NC asym	1543.4	2162.08	2058.3
			NC sym	1062.8	2170.87	2066.7
N3 Neutral	Ethanol (cont)	B3LYP	NC asym	1301.5	2184.58	2079.7
			NC sym	1369.5	2190.87	2085.7
N3 Neutral	Gas Phase	M06L	NC asym	1824.8	2105.69	2004.6
			NC sym	374.9298	2111.67	2010.3
N3 Neutral	Ethanol (cont)	M06L	NC asym	1559.5	2171.38	2067.2
			NC sym	1636.9	2178.5	2073.9
N3 Neutral	Gas Phase	PBE	NC asym	1413.7	2046.87	2020.3
			NC sym	774.2324	2054.71	2028.0
N3 Neutral	Ethanol (cont)	PBE	NC asym	1762.89	2107.81	2080.4
			NC sym	1639.2	2116.19	2088.7
N3 Cation	Gas Phase	PBE	NC asym	905.2	1999.71	1973.7
			NC sym	175.4	2001.56	1975.5
N3 Cation	Ethanol (cont)	PBE	NC asym	3817.02	2038.45	2012.0
			NC sym	494.86	2058.26	2031.5

Table 4: Computations carried out to minimize structure and calculate infrared frequencies.

known to have inaccuracies for metal center geometries.[174-176] For this reason, it was not used in further calculations despite having scaled gas-phase frequencies closest to N3@TiO$_2$ in air. The actual environment of N3@TiO2 in air was unknown. Thus, there was no way to gauge accuracy of the vibrational frequency calculations based on comparing gas phase frequencies to ethanol. There is a lack of frequency shift when calculating frequencies using B3LYP with ethanol as a PCM solvent. Not only does the IR frequency of N3@TiO$_2$ blue shifts from gas phase to solvent according to MO6L and PBE levels of theory but it is also expected to shift in solvent. The reason for this concern will be clearer after MD calculations are discussed, but essentially the spectra cannot be explained by calculations that do not shift the frequencies of the ligands more than 30 cm$^-$

[1]. Thus the blue shifts in M06L and PBE are preferable to B3LYP. There are not literature scaling factors for the PBE functional with the 6-31G(d) basis set. Scaling factors for different basis sets with the PBE functional were used in lieu of this and the scaled frequencies are very close to the M06l functional. Thus, there was no clear advantage from one functional to the next and so the M06l functional was chosen due to the existence of scaling factors. There was also anticipation of reactions occurring on the surface as well as iodine addition. The M06L functional also has good replication of geometry and was created for transition metal chemistry and noncovalent interactions.

Initially it was thought that iodine oxidizes N3 causing a blue shift due to less electron density donating to the pi back-bonding orbitals of the NCS ligands. To investigate this, calculations were carried out on N3 under different ionic and spin states as well as with iodine binding geometries. It is known that at the NCS ligands can decompose and so calculations with a CN ligand were carried out as well.[177] These results resulted in only one interaction of iodine with N3 results in a blue shift. Neither redox nor decomposition reflected a blue shift according to calculations.

6.5 MD Results

Molecular dynamics calculations were carried out for 0.88 ps for N3 and 1 ps for Z907. The span of total energy for the MD calculations was ~0.5 kJ/mol. Steps of 0.1 fs were taken because this should be much faster than the 4000 cm^{-1} period of ~8 fs for the highest frequency vibrations in the FTIR spectra.

Time points in femtoseconds for geometries partially minimized.

0.40	25.70	56.00	94.10	124.50	133	133.00	141.80	191.50
200.00	258.70	299.10	300.90	303.50	303.70	304.40	307.10	307.20
308.10	308.20	308.50	317.20	318.60	353.00	367.80	385.60	390.50
411.50	424.20	441.70	515.30	518.70	533.10	556.90	562.30	580.50
708.30	726.20	727.10	728.00	752.30	755.60	756.90	758.20	766.60
768.10	774.20	859.30	860.90	862.40	864.00	865.70	873.60	875.50

Table 5: Time points in MD calculations used to compare structural fluctuations affecting NCS vibrational frequency.
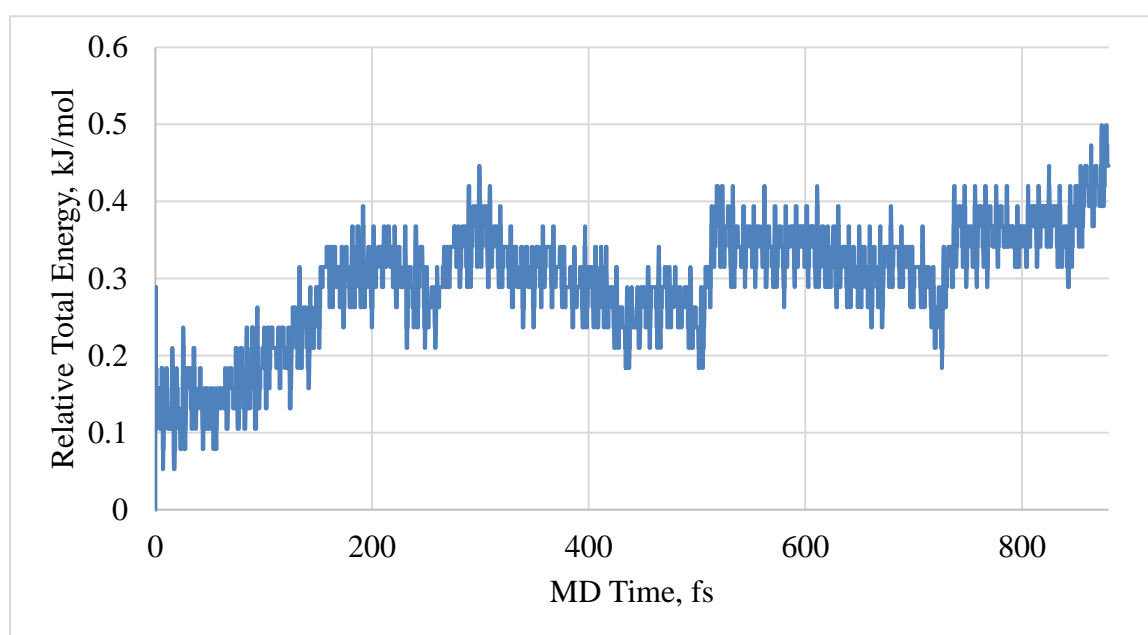
Figure 34: Relative total energy as a function of MD time step. The minimized structure energy is zero.

There is a possibility that the calculation would continue to rise in energy indicating instability but for the purposes here is a satisfactory result. Structures were more heavily chosen from the initial 300 fs (Table 5) while energy was on the rise and from the final 100 fs where things may have continued to trend out of control. The reasoning for this is that the maxima and minima between 200 and 400 fs reflect an equilibrated structure that is undergoing thermal fluctuations. The final 100 fs were near the highest energy points and so should cover the gambit of energies. Geometries were sampled from local maxima,

minima, and points in between where energy went unchanged for a series of structures. The notion was that this would capture the breadth of interplay between nuclear kinetic and potential energies. Then these structures were optimized with frequency calculations with all atoms frozen except for the NCS ligand atoms using the same functional, basis set, and solvent model mentioned above. Shown below in Figure 35 is a histogram of frequency points with 2 cm^{-1} bin width. The points between 2062 cm^{-1} and 2080 cm^{-1} approximate the homogeneous linewidth. There is an unexpected peak in points around 2042 cm^{-1} that is not apparent in the 2D-IR spectra. If the collection of molecular configurations due to solely to intramolecular motion were spanned by the results shown
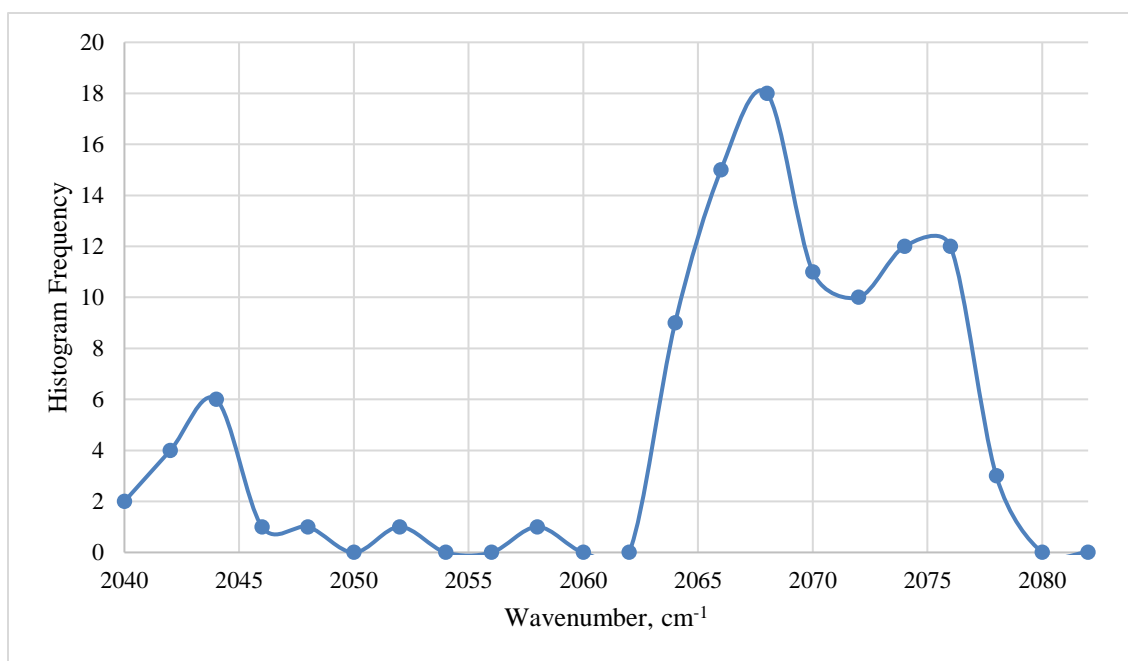
Figure 35: A histogram of frequencies calculated using partially frozen geometries of N3 selected from MD calculations. Bin widths are 2 cm^{-1}.

here, there would be an antidiagonal linewidth of 40 cm^{-1} in the 2D-IR spectra. This is not observed (Figure 37)

The red shifted frequencies may be anomalous or real. When the structures giving rise to them were visualized along with the atomic displacements associated with those

normal mode vibrations; they all reflected structures were the vibration was less delocalized over the two NCS ligands. The calculations reflect a correlation between increased Ru-N bond distance and redshifted frequency (Figure 36). If they are not erroneous frequencies, they would appear as cross-peaks over time in 2D-IR spectra. At early times they would overlap with the 1-2 transition and cancel out for frequencies pumped at higher wavenumbers and transferring to lower wavenumbers. There is no cross-peak above the diagonal that would represent energy transfer from low to high wavenumber. This indicates the isolated frequencies are erroneous or exist in low enough populations to be undetectable in the 2D-IR spectra. Also several computed geometries from the MD calculations did not converge and resulted in dissociation of S atoms from
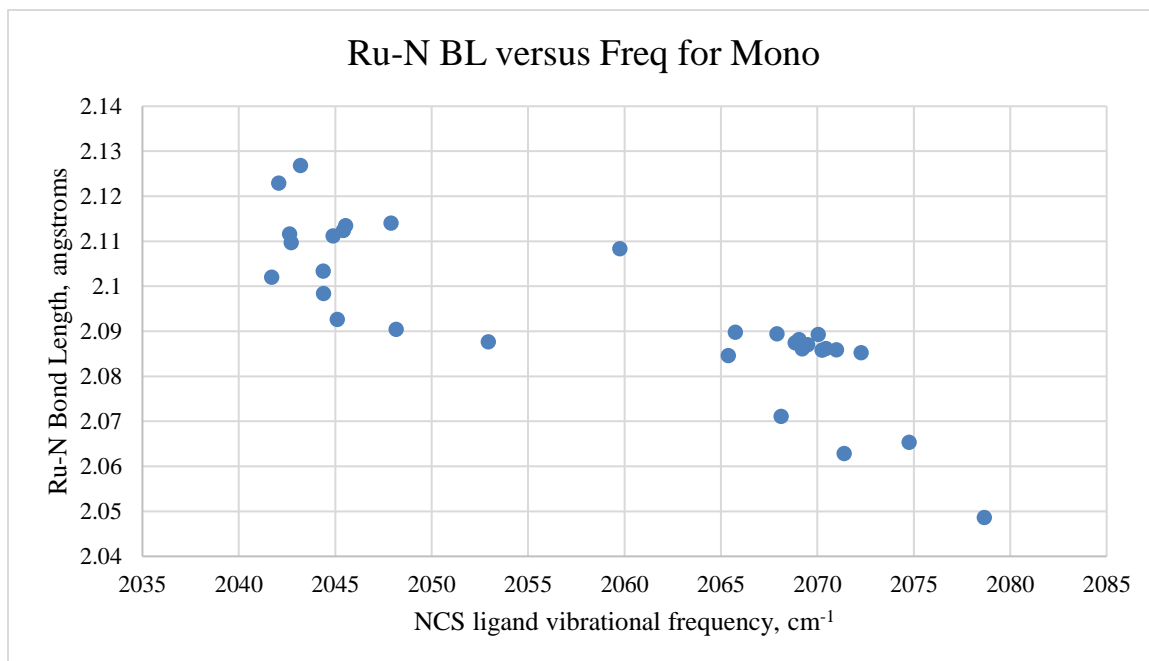
Figure 36: Ru-N bond length versus NCS vibrational frequency. Visualization of atomic displacements indicate the red-shifted frequencies are stretches almost entirely localized one NCS ligand, as opposed to the blue-shifted frequencies which are delocalized over both ligands.

the NCS ligands. This indicates that in the range of MD calculation geometries there may be unphysical local minima. There is not necessarily a suggestion of this in the calculation

itself but only when comparing to the experimental data and noting the two separate distributions of frequencies.

This is trending toward a calculation that reflects the homogeneous line width aside from the peak at 2042 cm^{-1}. This is what was expected as the antidiagonal linewidth in the 2D-IR spectra of N3 must reflect the instantaneous collection of molecular configurations which should be the ensemble average of structures that are obtained from MD calculations. This is true in this case as the peak does not evolve with time. Figure 37 below shows a 2D-IR spectrum of N3@TiO$_2$ in air. The 2 labeled data points give an antidiagonal width of 12.8 cm^{-1} at ~10% of the signal strength. The histogram above
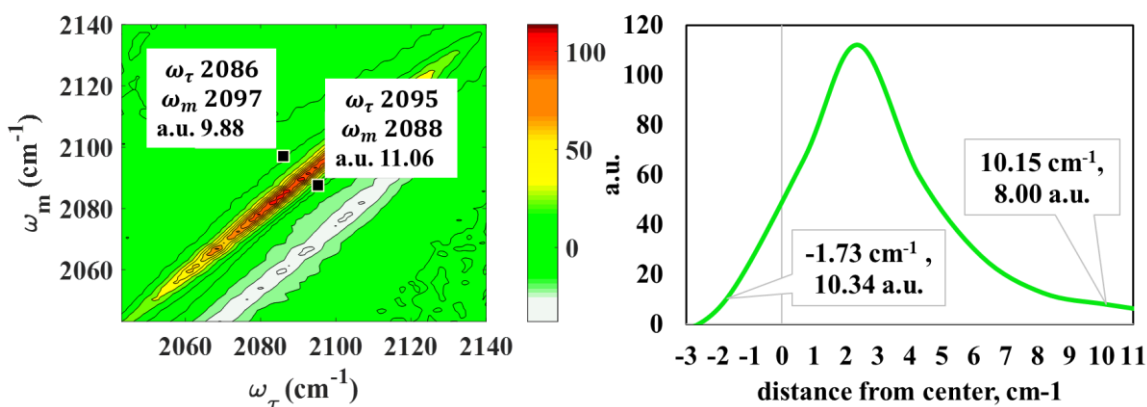
Figure 37: Left is a 2D-IR spectra of N3 with two points labeled. Right is an antidiagonal slice of spectra. The points are at 10% maximum intensity. The asymmetry is due to interference with the 1-2 transtion.
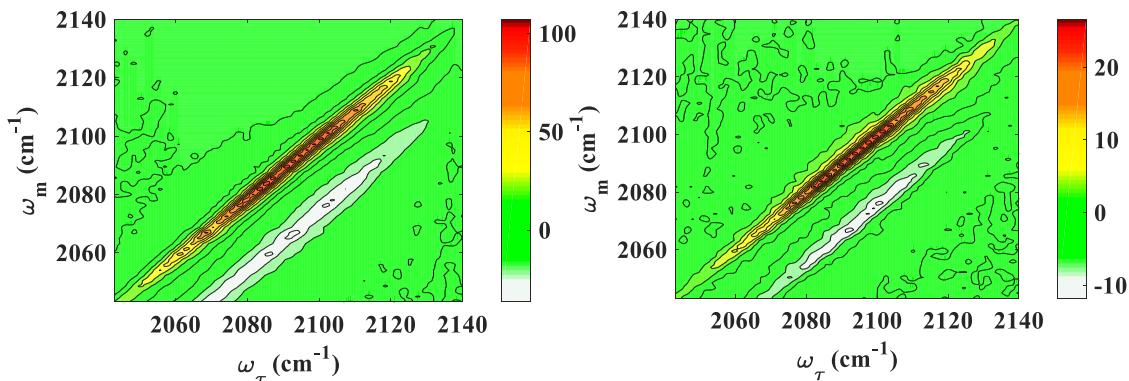
Figure 38 Spectra of N3 chemisorbed to TiO$_2$ nanoparticle films. T$_w$'s are 1 ps on the left, and 16 ps on the right. The absorbance maximum is approximately 2113 cm^{-1}. No dynamics are apparent from the spectra.

101

reflects this between 2168 and 2182 wavenumbers. The anti-diagonal slice shown to the right reflects this with ~11.9 cm⁻¹.

Referring to the Table 5 time points sampled, Figure 39 shows a plot of frequency versus MD time steps from which geometries were sampled. Figure 40 follows showing nuclear kinetic energy and potential energy versus MD time in fs. It is immediately apparent from figure 39 that the frequencies do not trend with time and that the transition from delocalized to localized vibrations is near instantaneous. The lower frequency vibrations were isolated to a single NCS ligand on N3 when atomic displacements were visualized using the modeling software (Gaussian). This suggests there is not a chemical conversion or a continuous part of the potential energy surface that results in the erroneous
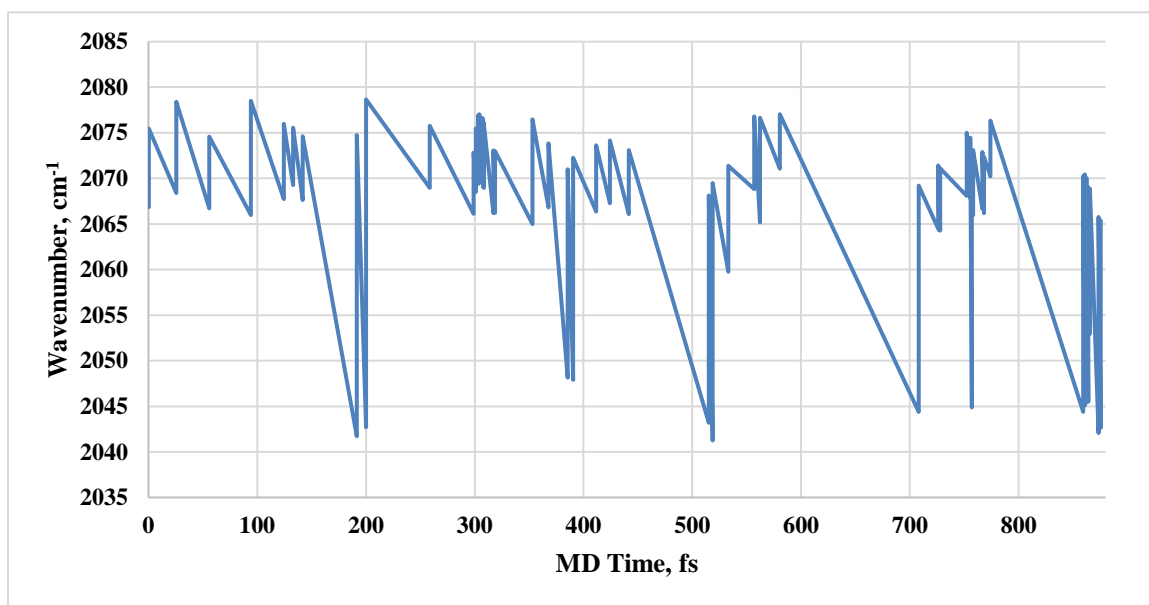
Figure 39: Calculated vibrational frequency for partially frozen N3 molecules at the selected MD time points.

red shifted peak in figure 37. Other quantities like nuclear kinetic energy, potential energy, or free energy do not correlate with frequency either.

Clearly the nuclear kinetic energy mirrors the potential energy (Figure 40). Energy conservation is in place and there doesn't appear to be anything anomalous in the

102
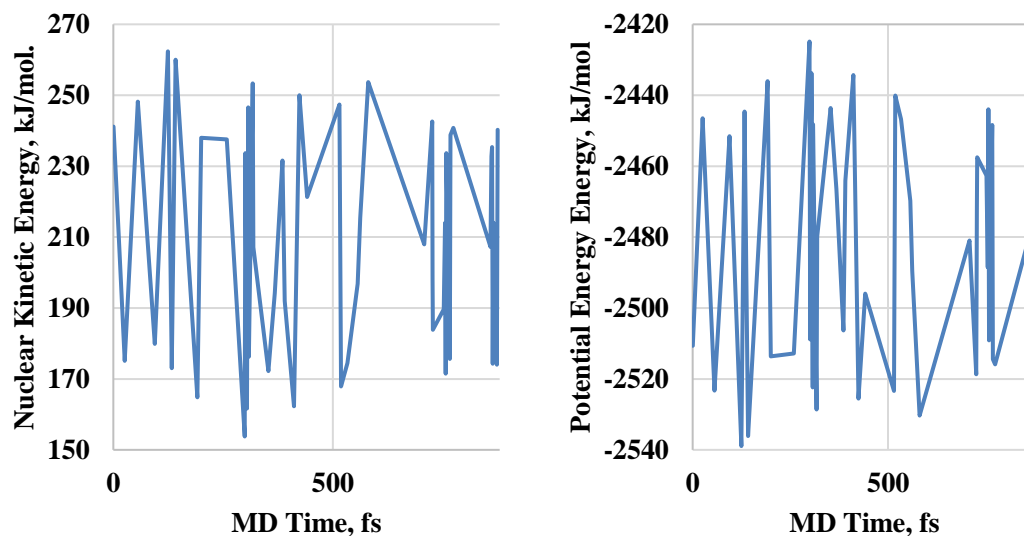
Figure 40: Left is nuclear kinetic energy versus MD time step of sampled geometries. Right is potential energy for the same. These energies are from the MD calculation itself and not partially frozen structures.

calculations giving rise to spurious vibrational frequencies. There are low frequency partially optimized structures with a range of potential energies. A trend was not found that connected high potential energy states to lower frequency vibrations. The next implication is that the partially (only NCS) minimized structure free energies might correlate with frequency. Figure 41 shows a plot of free energy versus vibrational frequency and that there is no correlation between vibrational frequency and free energy. There is a 12-15 cm^{-1} wide density of data points centered around 2072 cm^{-1}, a small population of red shifted data points, but no correlation with free energy. All energy quantities calculated and mapped to frequency result in almost identical plots. This all then leads to the conclusion that in the process of partially optimizing structures forom the N3 MD calculations there are erroneous frequencies and their only indication is the localization of the vibration to a single NCS ligand.

At this point calculations only roughly agree with the "true" frequencies.[178] The shifts in frequency over the MD calculations do not correlate with energy, and span the observed antidiagonal linewidth in close agreement (with the caveat of the erroneous frequencies). This is positive as it suggests that the calculations reflect the structural fluctuations that would occur near room temperature and those structural fluctuations acting as a perturbation to the NCS ligand frequency. A similar method can be applied to the Z907 dye. However, there is still the matter of the on-diagonal 2D-IR linewidth that should approximate the FTIR spectra.
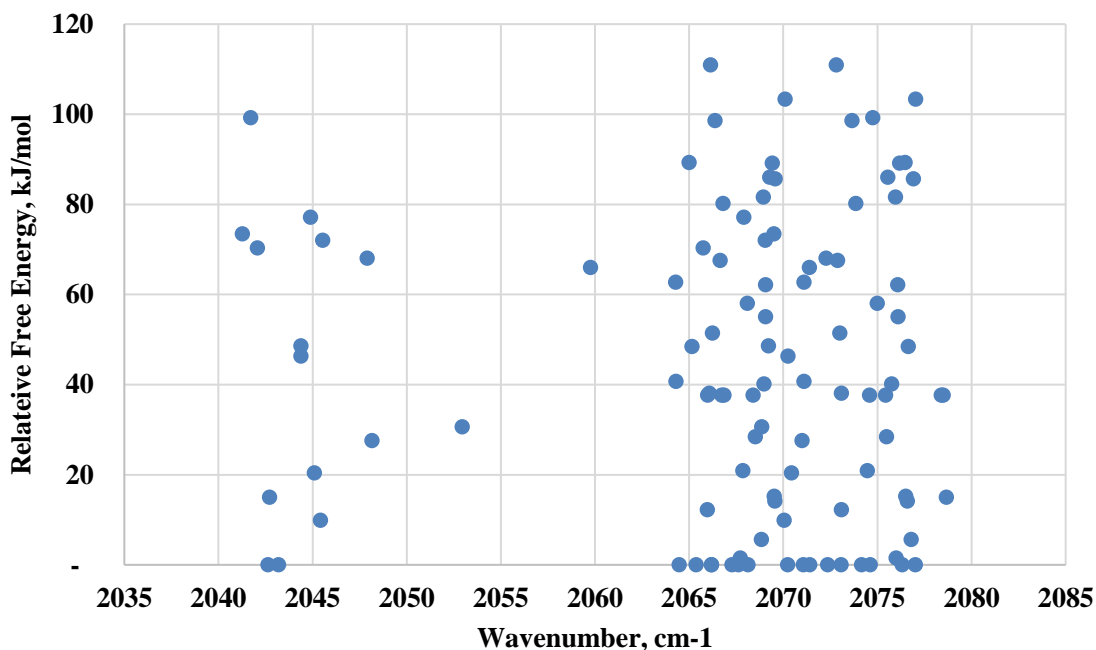
Figure 41: Relative free energy of selected MD geometries versus wavenumber of the partially optimized structures.

The N3 molecules in the film experience a variety of environments. For a crystalline anatase nanoparticle face there are many binding configurations for the molecule.[172] The N3 dye binds the surface of the nanoparticle via the carboxylate moieties on the bipyridine ligands. Calculations were carried out with the carboxylate moieties of

the bipyridine ligands deprotonated and this did not produce a frequency shift, likely due to the distance from the SCN ligands and the number of bonds between them. The surface of the nanoparticle with respect to geometry and defects will affect the intermolecular distance and relative orientation on a single nanoparticle as well as between different nanoparticles. Therefore, there must be ensembles in the film in the entire gambit of environments. This was addressed again using a PCM solvent model.

Solvents capturing the entire range of dielectric constants available were modeled using Gaussian. Figure 42 shows plots of NCS vibrational frequencies versus dielectric
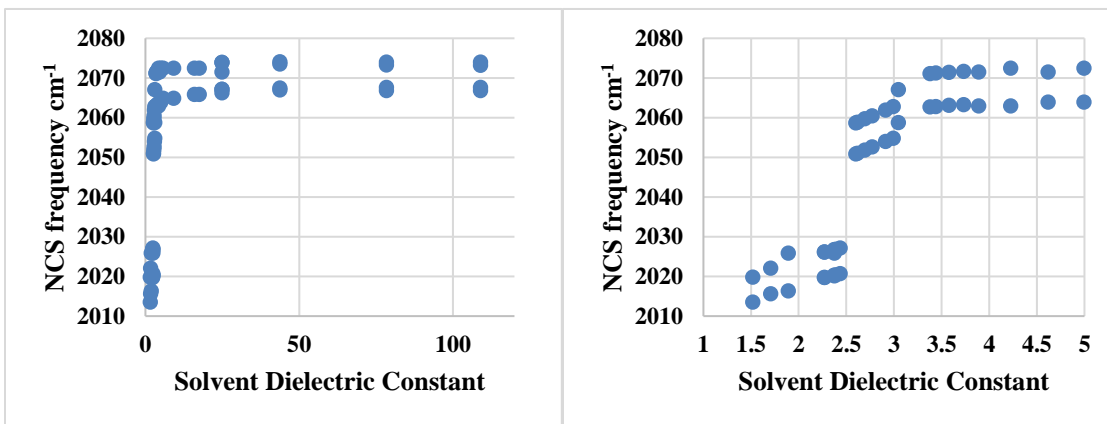
Figure 42: Left is a plot of the vibrational frequencies for the asymmetric and symmetric NCS vibrations on an optimized structure of N3 versus dielectric constant. Right is the same with a reduced axis scale.

constant. In the range of 0 to 120 there is a 50 cm^{-1} shift. For all calculations the entire geometry was optimized in the presence of solvent. The slightly lower frequencies are the antisymmetric stretch of the NCS ligands, and the higher frequencies are the symmetric stretch of the ligands. In all cases the vibrational modes involved equal displacements of both ligands. The antisymmetric stretch was higher in intensity in the calculations.

The symmetric and antisymmetric stretches are consistently separated by ~10 cm^{-1}. This would not be enough to resolve them in 2D-IR and any exchange would appear in

a 10 cm^{-1} x 10 cm^{-1} square region in the 2D-IR spectra. This is less than the area spanned

by molecules undergoing thermal stochastic fluctuations according to the MD calculations.

Therefore, computation again supports observations. The frequency shift due to solvent

occurs rapidly in the range of a dielectric constant of 2.5. This is slightly higher than that

of benzene. If the calculations are correct, then most of the N3 molecules are in an

environment similar to air with enough "solvation" due to the system to spread the

frequencies out. In fact, the on-diagonal intensity spans from ~2055 cm^{-1} 2125 cm^{-1} ($\omega_\tau =$

ω_m) This gives a span of:

$$99 \ cm^{-1} = \sqrt[2]{(\omega_{\tau_2} - \omega_{\tau_1})^2 + (\omega_m - \omega_m)^2} \qquad (34)$$

$$= \sqrt[2]{2 * (2125 \ cm^{-1} - 2055 \ cm^{-1})^2}$$

This is in agreement with a 50 cm^{-1} span due to the heterogeneous environmnet inducing a

variety of evnvironments about N3 and an additional 12 cm^{-1} span due to the intramolecular

stochastic fluctuations. Pythagoreams therom is then used to calculate diagonal width

where 12 cm^{-1} has been added twice for each end of the peak width predicted by implicit

solvent modeling.

$$105 \ cm^{-1} = \sqrt[2]{(2 * 12 \ cm^{-1} + 50 \ cm^{-1})^2} \qquad (35)$$

6.6 Z907 Comparison

In the case of Z907 there are two nonyl in the place of to carboxyl groups on the

bipyridine ligands (Figure 30). This should add to the antidiagonal linewidth due to

additional atoms that would contribute to more structural variation due to stochastic fluctuations. The nonyl chains have enough confomations accessible that they could solvate the NCS ligands inter or intramolecularly. A larger variety of accessble environments in this way may also expalain the boradening of the FTIR upon iodine addtion in contrast to N3 (Figure 43). Molecules in air for Z907 have a slightly narrower FTIR that broadens when exposed to gaseous iodine. There is a slight narrowing of N3 when exposed to iodine (Figure 33). However in both cases there is increased peak assymetry when exposed to gasesous iodine evinced by the sharper decrease in absorbance on the blue side of the peak.
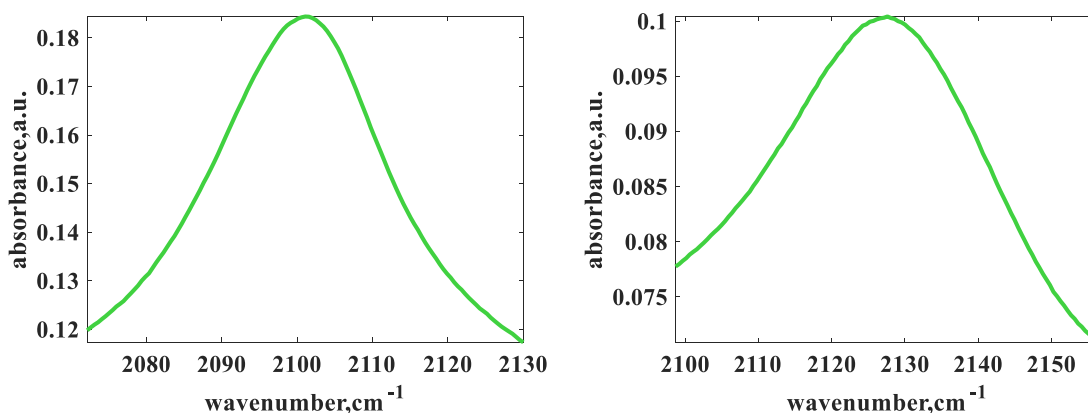
Figure 43: FTIR of the NCS stretches in Z907@TiO$_2$. Left is in air with an absorbance maximum of 2101.1 cm^{-1} and right is saturated with gaseous iodine with an absorbance maximum of 2127.6 cm^{-1}.

Before the iodine adsorption experimental data is discussed there are comparative comptations for Z907@TiO$_2$. When carrying out MD calculations in a similar manner the frequencies are more evenly distributed (figure 44), specifically in the red-shifted modes between 2050 cm^{-1} and 2055 cm^{-1}. The MD time steps from which geometries were chosen were different for Z907 than for N3 but followed the same reasoning. There are again lower frequency vibrations that are separated from the main peak in the histogram of vibratioanl frequencies calculated from patially frozen geometries. When similarly visualizing the atomic displacements for these freuqencies there was less less localization of the red shifted modes. The vibrations for the red-shifted frequencies are also not isolated to a single ligand but reflect more of the symmetric and assymetric stretches of the blue-shifted N3 frequencies. This maximum frequency differnce for a localized red-shfited NCS stretch on a single moleucle is 27.2 cm^{-1} for Z907 and 37.8 cm^{-1} for N3. There may be two populations of vibrational modes but are less distinct when histogrammed. In this case there is less reason to believe the red-shifted frequencies are erroneous. There is less flip-
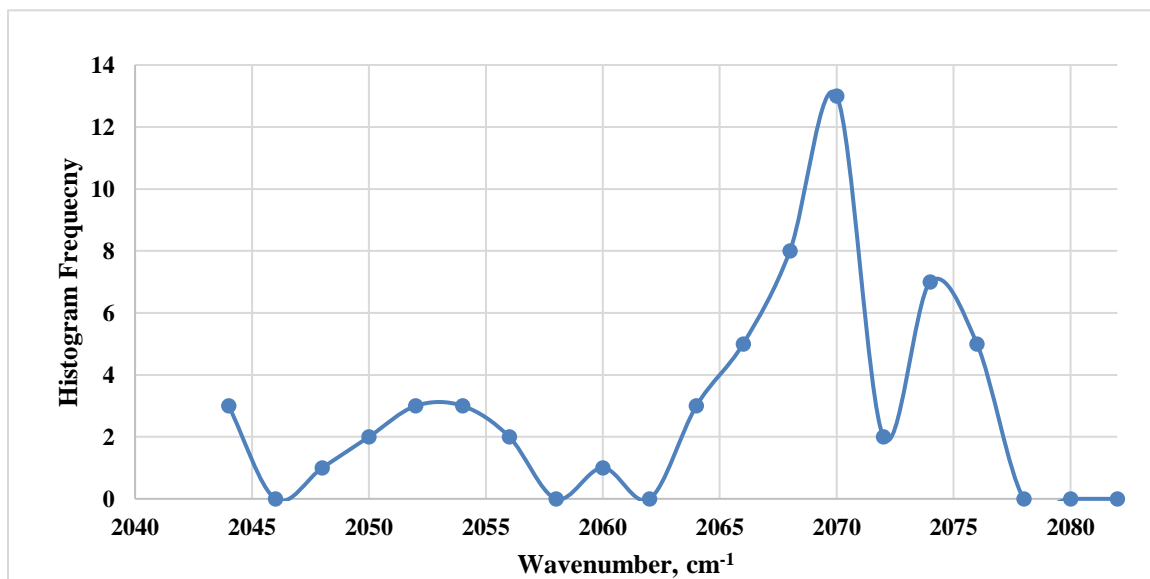
Figure 44: A histogram of frequencies calculated using partially frozen geometries of Z907 selected from MD calculations. Bin widths are 2 cm^{-1}.

flopping between red and blue modes as a function of MD time (Figure 45). This is qualitatively reflected in the MD calculations displaying a broader and more uniform distribution of frequencies. The frequency distribution at various MD time steps and Free Energy versus wavenumber plots do not exhibit the same discrete populations as N3 (Figure 45).
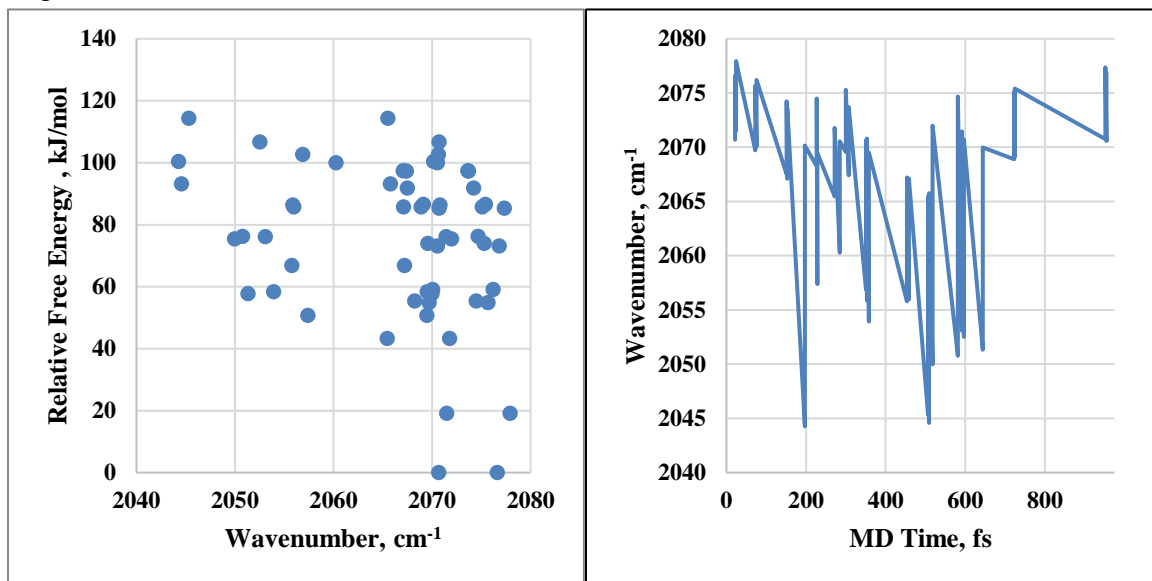
Figure 45: Left is relative free energy versus vibrational frequency for Z907 similar to figure 41 for N3. Right is vibrational frequency for Z907 versus MD time step similar to figure 39 for N3.

Two-dimensional infrared spectra of Z907 at same T_w's for N3 in Figure 38 are shown in figure 46. Z907 displays significant spectral diffusion as opposed to the case for
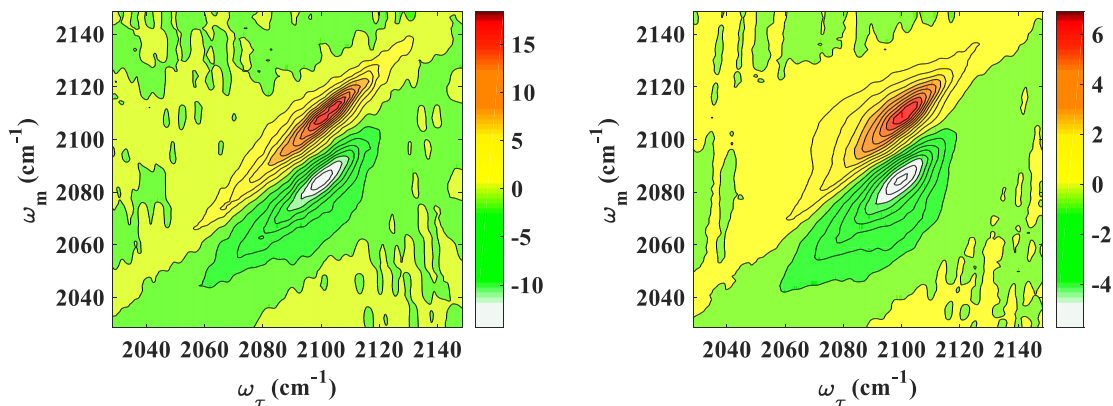
Figure 46: Spectra of Z907 chemisorbed to TiO$_2$ nanoparticle films. T_w's are 1 ps on the left, and 16 ps on the right. The absorbance maximum is approximately 2113 cm^{-1}. Spectral diffusion is apparent in the spectra.

N3. This spectral diffusion is not complete as there is still a large amount of static heterogeneity in the film. The spectral diffusion due to the greater breadth of environmental accessiblity for a given molecule or subensemble is assumed to be due to the nonyl chains. This is what was expected from the MD calculations. This forms a basis for further calculations that could include explicit solvent moleucles or adsorbed species. An automated approach to sampling MD structures is necessary to confirm the accuracy of this approach.

6.7 2D-IR Spectra of N3 and Z907

Two-dimensional infrared spectra were collected from films with varying solution concentrations of I_2 in chloroform, I_2 in hexane, and gaseous I_2. These experiments were aimed at fundamentally connecting solvent dynamics, gas adsorption, redox couple charge transfer rates, and specific redox couple dynamics to the well-studied DSSC properties that popularized N3 and Z907. DSSC systems with N3 use an I^-/I_3^- redox couple in solution to complete the redox cycle and rates of reduction of oxidized ruthenium dyes by the electrolyte are known to be on the order of 10^9 s^{-1}.[177] The solvent dynamics induced by I_2 are of interest because they may connect to high rates of reduction which may speed the ability of dyes to be photoexcited and inject electrons into TiO_2. This was the reason for I_2 experiments.

The N3 dye undergoes loss of sulfur in prolonged exposure to light without the electrolyte.[177] This might have been reflected in the failed frozen atom optimizations from the MD calculations in which S dissociated from the rest of the ligand. The resulting cyanide species is clear experimentally from a CN$^-$ stretch of 2084 cm^{-1}. Measurements have been carried out on this analogue in air, but the spectra are similar to those in Figure

38 but with a red shifted peak center. Further 2D-IR experiments have not been carried out on the cyanide analogue at this time.

Beginning with the representative FITR spectra of N3 in chloroform, figure 47 shows N3 in pure chloroform, 0.8 mg/ml iodine in chloroform, and 1.7 mg/ml iodine in chloroform. The 2D-IR spectra for these solutions are shown in figures 48, 49, and 50
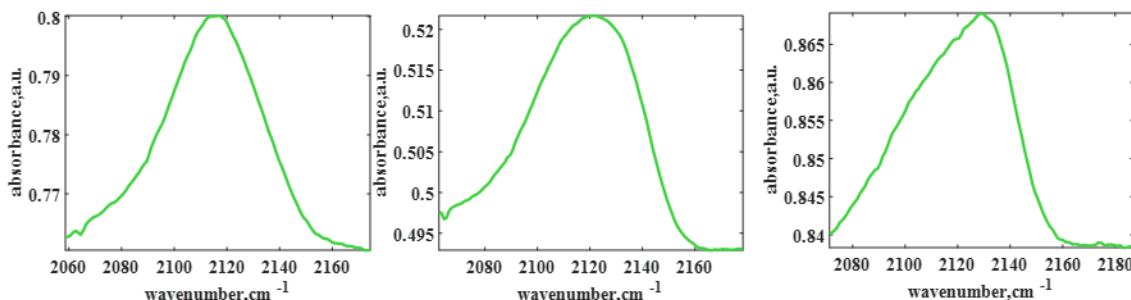
Figure 47: Spectra of N3@TiO$_2$ in chloroform, 0.8 mg/ml I$_2$ in chloroform, 1.6 mg/ml I$_2$ in chloroform from left to right respectively. The peak maximum gradually shifts from 2120 cm^{-1} to 2130 cm^{-1}.

respectively. A notable difference from the gas phase iodine addition is that there is not the same magnitude of peak blue shifts in the FTIR spectra. Chloroform has a relatively low dielectric constant, however the calculations performed suggest this is enough to blue shift the peak. In chloroform solvent, the species that have iodine bound have a longer lifetime as indicated by the increase in relative intensity of the higher wavenumber region of the spectra.

The FTIR spectra compared to the 2D-IR spectra show a more pronounced blue shift and peak shape evolution with increasing iodine concentration. The increased off-diagonal intensity in the 2D-IR spectra is only prominent at higher iodine concentrations. If there were an exchange signal due to iodine leaving an N3 molecule, decomplexing, or terminating interaction in whatever form this takes; then this signal would show up below the 0-1 peak. This would overlap with the 1-2 peak and be difficult to see. The cross

peak above the 0-1 peak would indicate N3 molecules undergoing iodine complexation or

potentially VET.
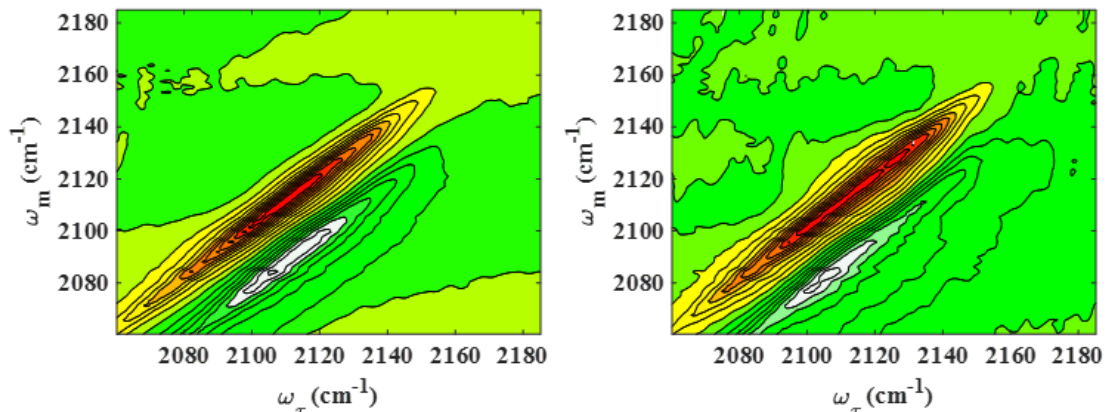
Figure 48 ; 2D-IR spectra of N3 in Chloroform at T_w's 1.0 ps (left) and 20.0 ps (right). The appearance of broadening is an artifact of the plotting. Both 0 to 1 peaks have the same FWHM along the antidiagonal. The FWHM is ~6 cm^{-1} while N3@TiO$_2$ is ~3 cm^{-1}
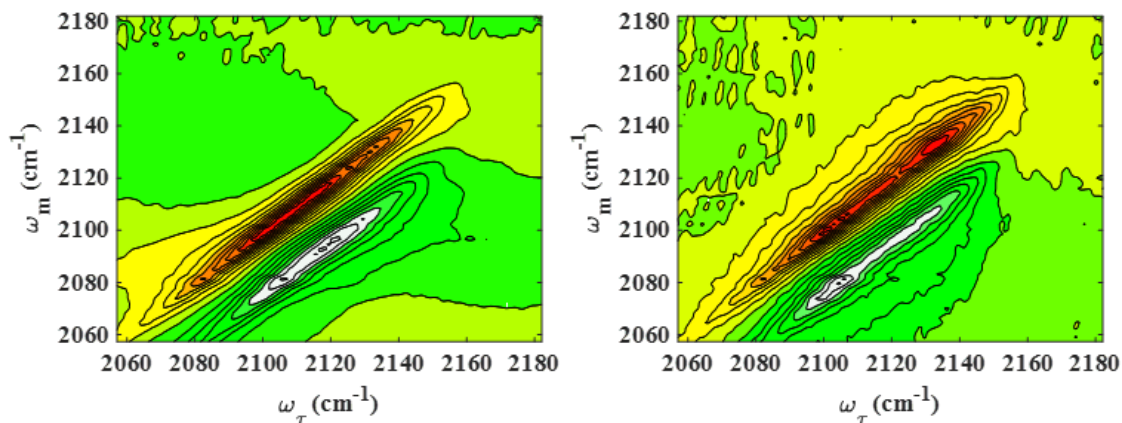
Figure 49: 2D-IR spectra of N3 in Chloroform with 0.8 mg/ml I$_2$ at T_w's 1.0 ps (left) and 20.0 ps (right). The increase in relative intensity of the iodized species at 2137 cm^{-1} relative to the non-iodized reflects a difference in vibrational lifetime
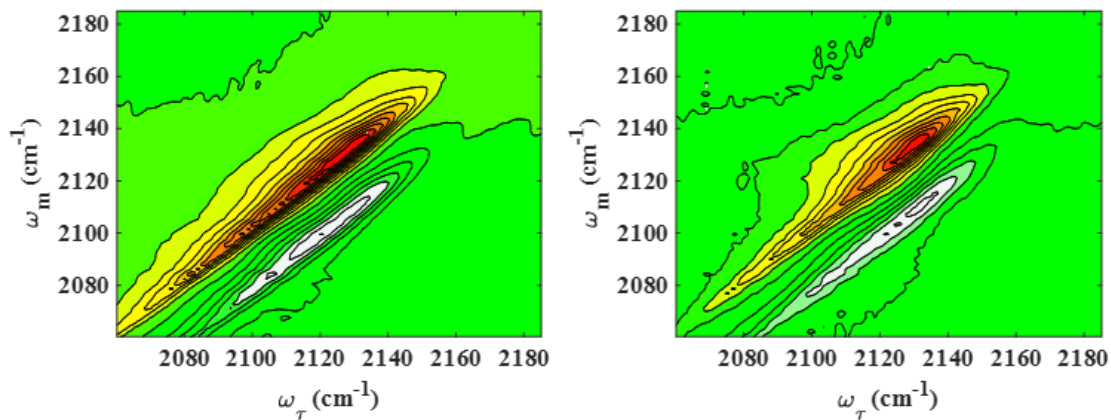
Figure 50: 2D-IR spectra of N3 in Chloroform with 1.7 mg/ml I$_2$ at T_w's 1.0 ps (left) and 20.0 ps (right). The increase in relative intensity of the iodized species at 2137 cm^{-1} relative to the non-iodized reflects a difference in vibrational lifetime. There is also an indication of possible exchange from the non-iodized to the iodized species reflected in the intensity above the diagonal.

Interestingly this is only visible at higher concentrations. The signal intensity of exchange peaks scales with the intensity of both populations, the lifetimes of the species, and the reaction rate constant. This is captured in the case with equivalent vibrational lifetimes in the work of Peter Ham and Martin Zanni as well as other kinetics texts.[31, 179] With two species having different vibrational lifetimes the solution must be pieced together as discussed later in this section.
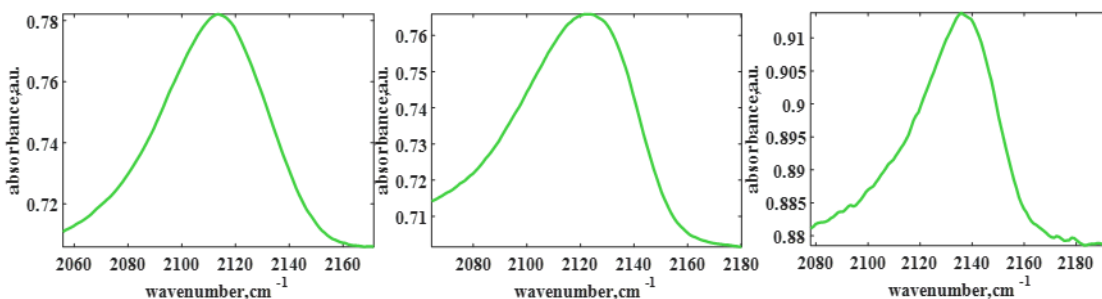
Figure 51: From left to right: N3@TiO$_2$ in air, partially doped with I$_{2(g)}$, and fully doped with I$_{2(g)}$.

Similar to the N3@TiO$_2$ in chloroform data, there is another data set to review. This FITR spectra for N3@TiO$_2$ in the presence of gaseous iodine are shown in Figure 51. The data are similar to the chloroform data with undoped, partially doped, and fully doped N3. The FTIR spectra for N3 shift further by a few cm^{-1} which is attributed to the lack of solvent causing the gaseous iodine blue shift to be more pronounced.

There are many closed form kinetic solutions in the case of two species interconverting in concert with irreversible reactions for both species. This is provided the rate constants are equivalent. Even in the case of different vibrational lifetimes this situation has a closed form solution. If T$_1$ is equal to T$_2$ then the solution is simpler. However, in the case of unequal reaction rates and vibrational lifetimes the solution is more complicated. Two basic kinetic schemes are depicted below (figure 54).
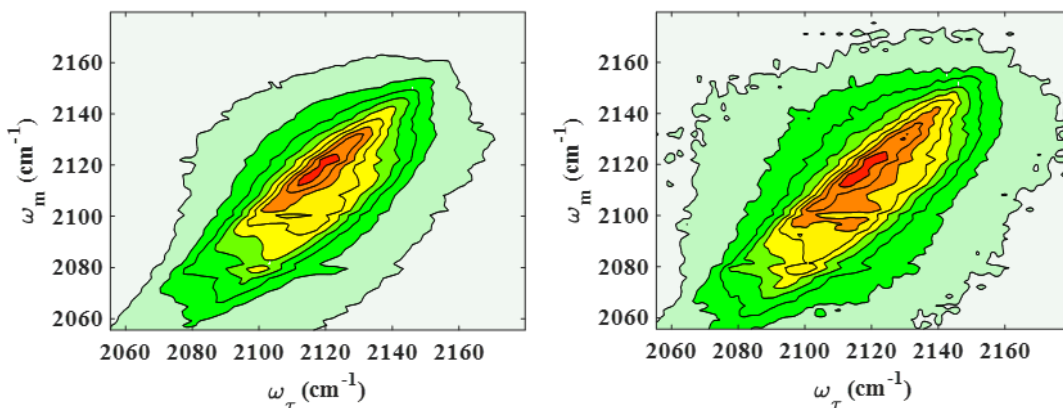
Figure 52: Partially doped I₂ at Tw = 1.0 ps (left) and 16.0 ps (right).
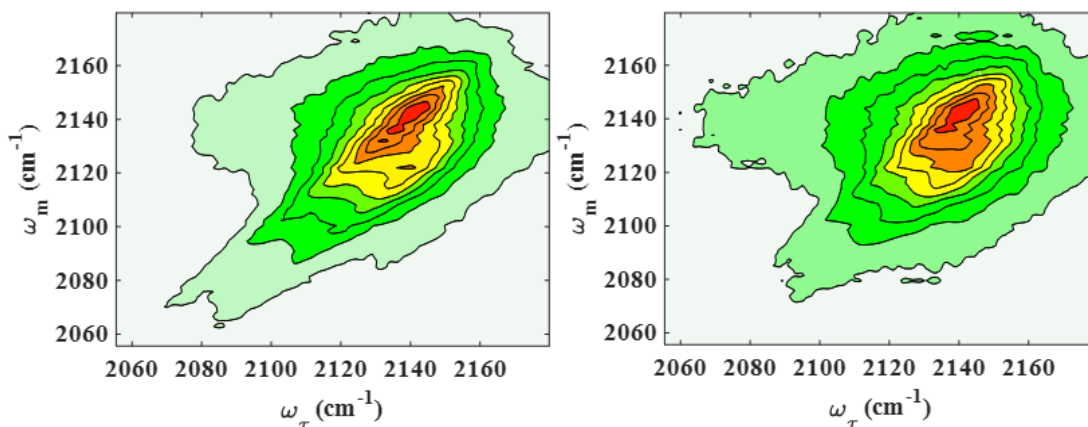
Figure 53: N3@Ti)₂ saturated with I₂(g) at Tw = 1.0 ps (left) and 16.0 ps (right).

When doping either Z907 or N3 with gaseous iodine there are different vibrational lifetimes and only one rate can be observed as one of the cross peaks falls on top of the 1-2 peak. The 2D-IR spectra of N3 partially and fully doped with gaseous iodine are shown in Figures 52 and 53 respectively. Comparing these to Figure 38 spectra of N3 in air, there is clearly off-diagonal intensity. It appears in both partially doped and fully doped spectra. Comparing this to figure 50 for fully iodine-doped N3 in chloroform there also appears to be off-diagonal intensity. If there is exchange that occurs at different levels of doping. Determining this can be done by kinetic analysis. There are two main schemes that can be

used to accomplish this (Figure 54). There is an analytical solution scheme 1 in figure 54

and for Scheme 2 there is a published solution that breaks the system into separate

equations for A and C, and B and D.[141] The solution for species C is as follows:

$$B(t) \cos^2(\theta, t) \tag{36}$$

$$= \frac{4}{5} * \left(A e^{t*k_1} + B * e^{-t*\left(k_{-1}+\frac{1}{T_2}+6*D_B\right)} \right) + \frac{1}{3}$$

$$* \left(A e^{t*k_1} + B * e^{-t*\left(k_{-1}+\frac{1}{T_2}\right)} \right)$$

Here the cosine and D_B represent rotational diffusion constants for a solution sample. In

the case of a SAM on a nanoparticle film these terms do not apply as there isn't molecular

rotation. This formulation treats the cross-peak as its own species which is done by only

treating half of Scheme 2. This treatment also assumes that the rates ($A*k_1$ and $B*k_{-1}$) are

equal as the species are in equilibrium. This assumption is correct as the samples must be

stable for the long periods of time it takes to generate the 2D-IR data abd so in this case

chemical equilibrium these assumptions are valid.
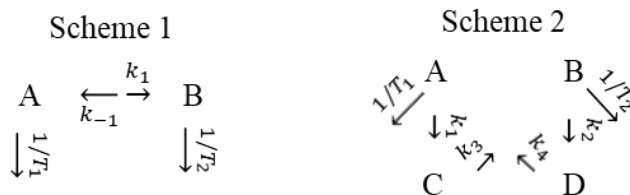
Figure 54: Kinetic schemes depicting an equilibrium between A and B with irreversible pathways (Scheme 1, left) and the same scheme with "artificial" species C and D representing A going to B and B to A respectively (Scheme 2, right).

In 2D-IR the signal of the cross-peak is scaled by the on-diagonal peak at the same

probe frequency. In the case of chemical kinetics, it is a moot point with respect to

explaining exchange in "fully doped" samples because increasing the on-diagonal signal

by increasing its relative population decreases the population that could transfer into it. There is no possibility of increasing signal of a cross-peak while simultaneously decreasing the population it is transferring from unless it is a weak cross-peak that requires on-diagonal intensity to be visible at all. In the N3 and Z907 samples the fact that the 1-2 peaks are not far enough apart to resolve the cross-peak below the diagonal opens the question of whether this is the case in the chloroform data in Figure 50. Can exchange be enhanced while doping decrease the reactant species? If the exchange peak lying on the 1-2 2D-IR peak were resolvable then any assumptions about equilibrium and the mechanism of the underlying cross-peak would be addressed. Meaning, if it were chemical exchange, then an equilibrium with both corresponding cross-peaks would be observed and the partially doped and fully doped concentrations would tease out the actual rate constants beyond the observed overall rate of number or molecules per time.

In the case of VET though, is it necessarily required to be symmetric and do the same assumptions apply? Equal rates? Vibrational energy transfer is governed by quantum mechanics with creation and annihilation operators. In the simplest sense, the transition between two states is as follows:[180]

$$\langle Finish | \widehat{Through} | Start \rangle \qquad (37)$$

It is not guaranteed that the transition probability is equal in the reverse direction. However, in the case of the 2D-IR experiments the BOXCARS geometry is used to select certain response functions (Equation 18). The real and complex response functions are collected simultaneously. This means that for all intents and purposes the following

relationship dictates that signal discrimination results in A to B and B to A being equivalent.

$$\langle A|\hat{O}|B\rangle = \langle A|\hat{O}|B\rangle^*$$ (38)

Even if this were not the case, Fermi's golden rule states that as long as the light is broad relative to the transition frequency then the probability of A going to B and B going to A are equivalent.[181]   Therefore the Fayer treatment is valid even outside of chemical exchange. A situation in which it is not valid is where the difference in energy between two states is greater than k_bT at room temperature and one state is excited due to absorption and the other state decays due to spontaneous emission. Even in this case though, the pathways involving coupled oscillators depend on the transition dipole of each oscillator.[31] The Feynman diagrams in Figure 4 can be used to represent the pathways of excitation and emission. Coupled oscillator states are represented by a state with two indices ($|i,j>$) instead of one ($|i>$). Inherent in the two indices is that the states of individual oscillators are coupled.[31, 81]

Signals for a single oscillator scale as the transition dipole to the 4th power.   For any pathway resultant in a cross-peak the intensity depends on both oscillators' transitions dipoles squared ($|\mu_1|^2|\mu_2|^2$). This means there is no possibility to have cross-peak intensity if there is no population of one oscillator. So, the kinetic equations depending on concentration are completely valid though they do not capture the mechanism that results in cross-peaks. This can be arrived at by comparative experiments like the case of Shvo in Chapter 4 where temperature dependence differentiated proton exchange from VET. Then

the only explanation for the appearance of a cross-peak only at full doping in the chloroform data is from phasing errors or there is only exchange between a small area of subensembles that becomes apparent when the intensity of the undoped N3 is diminished by saturating the film and having all or almost all of the doped species. Absolute value spectra do not require phasing and can be used to analyze the kinetics to answer these questions.

Representative absolute value spectra for N3@TiO$_2$ in an I$_2$ in chloroform solution at a concentration of 1.7 mg/ml are shown in figure 55. Even though there is signal intensity in the cross-peak area it does not increase relative to the on-diagonal intensity nor does it have a longer vibrational lifetime which indicates that there is no exchange. This
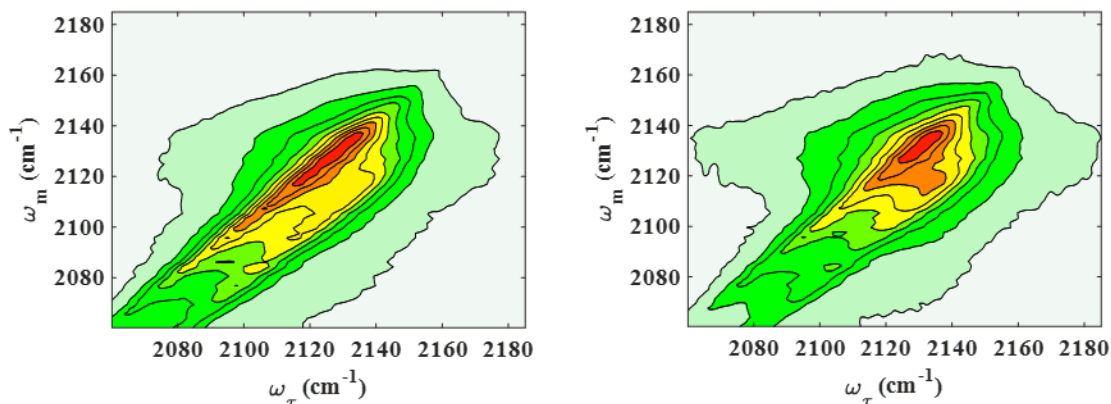
Figure 55: Absolute value 2D-IR spectra of N3 in Chloroform with 1.7 mg/ml I$_2$ at T$_w$'s 1.0 ps (left) and 20.0 ps (right). Kinetics analysis of spectral regions do not suggest exchange.

signal then could only indicate anharmonic coupling between the doped and undoped N3 molecules. The appearance of this at higher concentrations then could indicate iodine bridging two adjacent molecules or forcing them into closer proximity.
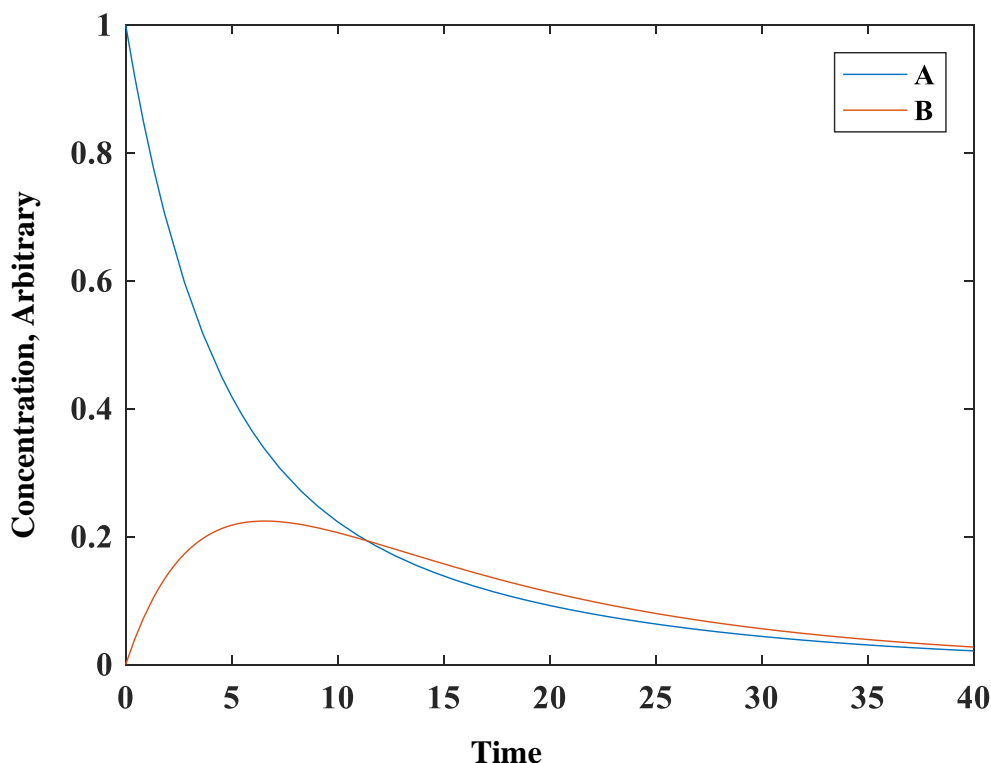
Figure 56: Blue is species 'A' representing the on-diagonal and orange is species 'B' representing the cross peak from scheme 1. Arbitrary rate constants of 1/10 and vibrational lifetimes of 10 and 20 for A and B respectively.

This is all to say that a simple kinetic model like Scheme 1 in Figure 54 can be used to treat any nature of exchange. Figure 56 shows results from this kinetic model. This certainly reproduces a rising signal that decays with vibrational lifetime. However, there is one downfall of this approach. There can be no concentration dependence on species 'B'. Its initial concentration is always 0 which is true for a cross-peak that is not anharmonically coupled. The cross-peak signal at the same monochromator frequency (ω_m) is scaled by the on-diagonal peak intensity. The exponential growth is typically arrived at by dividing the cross-peak intensity by the on-diagonal peak intensity at the corresponding probe intensity. This requires either a system of equations or a second set of equations depicted in Scheme 2 for the second half of the 2D-IR spectra. This is what was done to investigate the N3 and Z907 systems studied that are suspected of having

exchange signals. Results show that exchange appears at partial doping but disappears for full doping.

The appearance of a cross-peak in the partially doped N3 film with gaseous iodine is consistent with are two relatively equal populations of the doped and undoped species maximizing signal per transition dipoles. The spectra are absolute value spectra which decrease resolution but avoid phasing errors and the kinetic analysis of the cross-peaks indicating exchange is reliable. Exchange is indicated by slower exponential decay or relative intensity growth in the off-diagonal region between the two peaks.
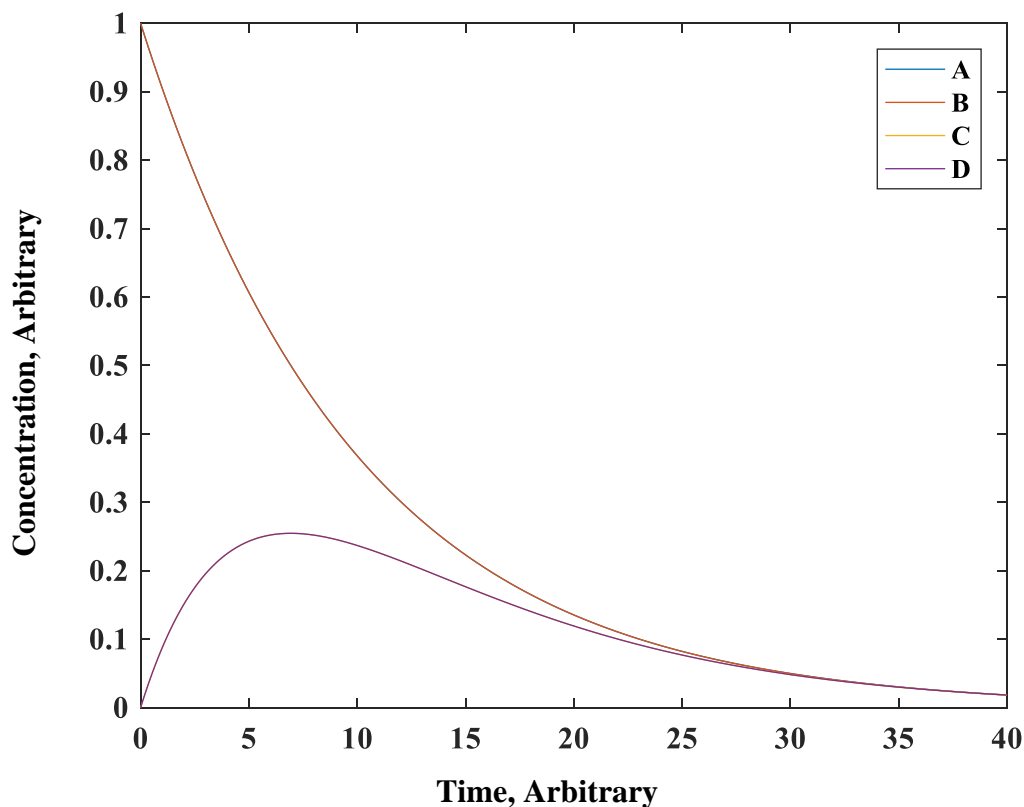
Figure 57: A and B are the on-diagonal which decay exponentially. C & D are their vector cumulative sums divided by their max and multiplied by their respective off-diagonal peak intensity. As all rate constants and lifetiems are equal, A and B and C and D fall on top of one another.

With regard to Scheme 2 in Figure 54 this can be solved numerically. If the rate constants k_3 and k_4 are extremely fast so that these populations never build up, then there is no change in the population of A and B. However, the cumulative sum of C or D which represent A going to B or B going A respectively, are not easily normalized. They depend on the numerical method. However, if we take the cumulative sum of these vectors, divide by their maximum, and multiply by their respective on-diagonal peak intensity (same ω_m); they qualitatively represent the same dynamics. Because a cross-peak is proportional to the transition dipole of the two involved species, a cross-peak can never be more intense than it's respective on-diagonal as they ultimately go to zero together despite decaying with
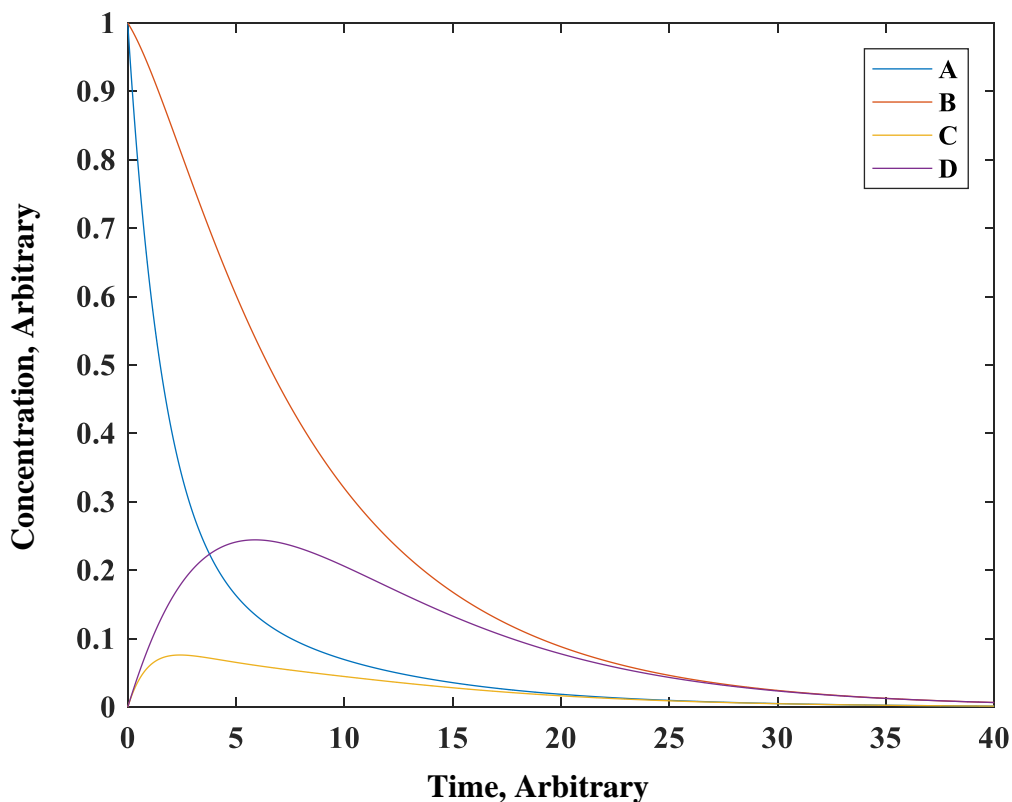
Figure 58: Similar to figure 23 except the vibrational lifetime of 'A' is 2 and 'B' is 20. C stops growing with the lifetime of A while D with the lifetime of B.

the different rates. In this respect the numerical model represents a somewhat more physical picture. Formally normalizing the signal intensity is not explored here.

Figure 57 shows kinetic model predictions when populations, rates, and lifetimes are equal. Figure 58 represents the same system as figure 58 except the lifetime of A is 2 while the lifetime of B is 20. This was done for illustrative purposes. The cross-peaks
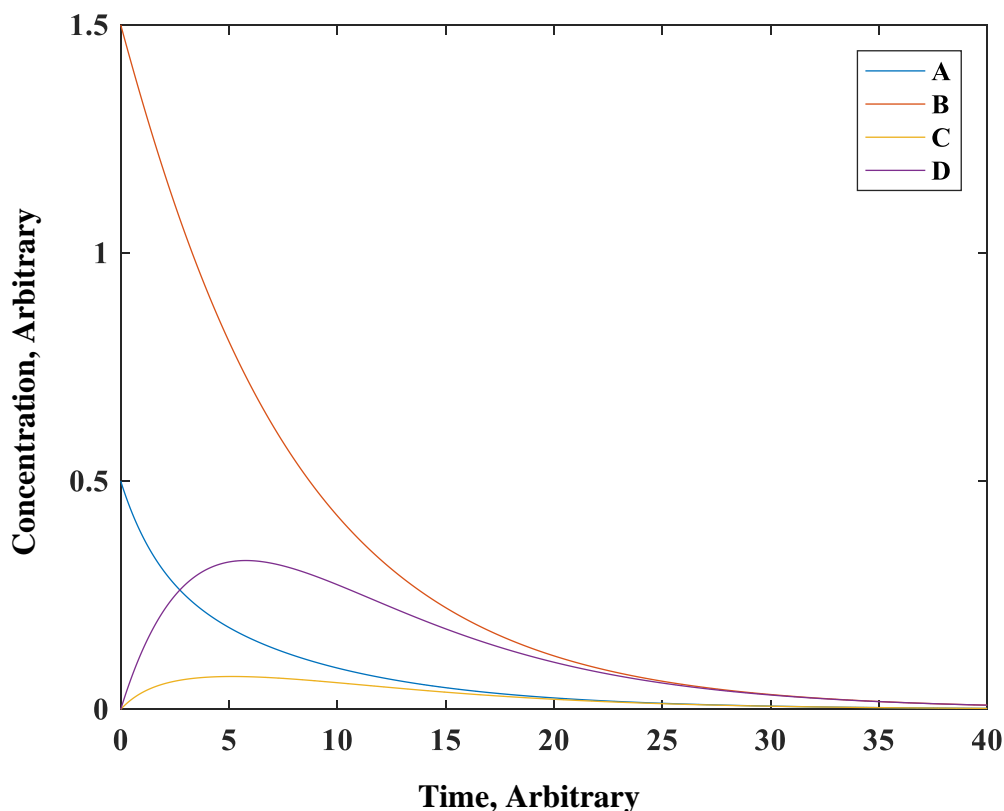
Figure 59: Similar to figure 24 except the respective populations of A and B are changed. A decrease in A does not result in an increased cross-peak of C relative to B. This again con firms previous analysis.

grow in continually until their respective sources decay. Figure 59 is the same model while the relative population of B is increased by an amount taken from A so that the total initial amount of species is constant. There is no increase in the C signal again confirming that it is impossible to decrease an on-diagonal population and increase the cross-peak intensity. This was confirmed with all iterations of rate constants.

In the case of iodine exchange the phenomenon being observed can be confirmed or discounted by comparative experiments and kinetic modeling. Phenomena include the mechanism by which exchange occurs leading to cross-peaks. In the case of fully doped
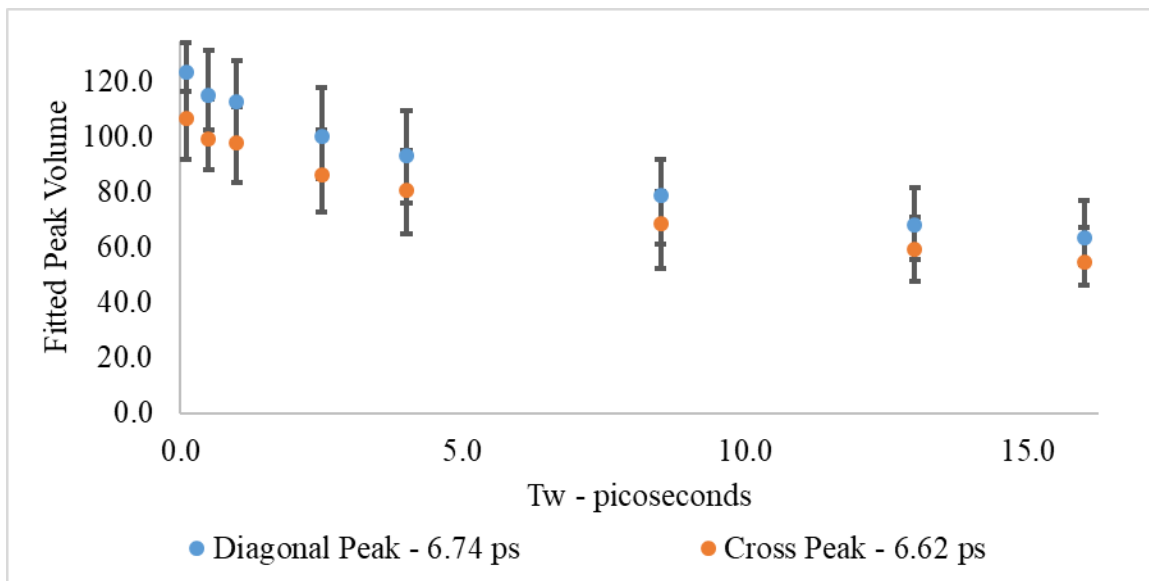
Figure 60: Analysis of on-diagonal, off-diagongal, and the off-diagonal peak volume divided by the on-diagonal peak volume for the N3 fully doped data resultant from fitting the spectra with 2 Gaussian peaks at a specific monochromator wavelength of 2140 cm $^{-1}$. Error bars indicate the 95% confidence interval calculated from fit errors and overlaid on data.
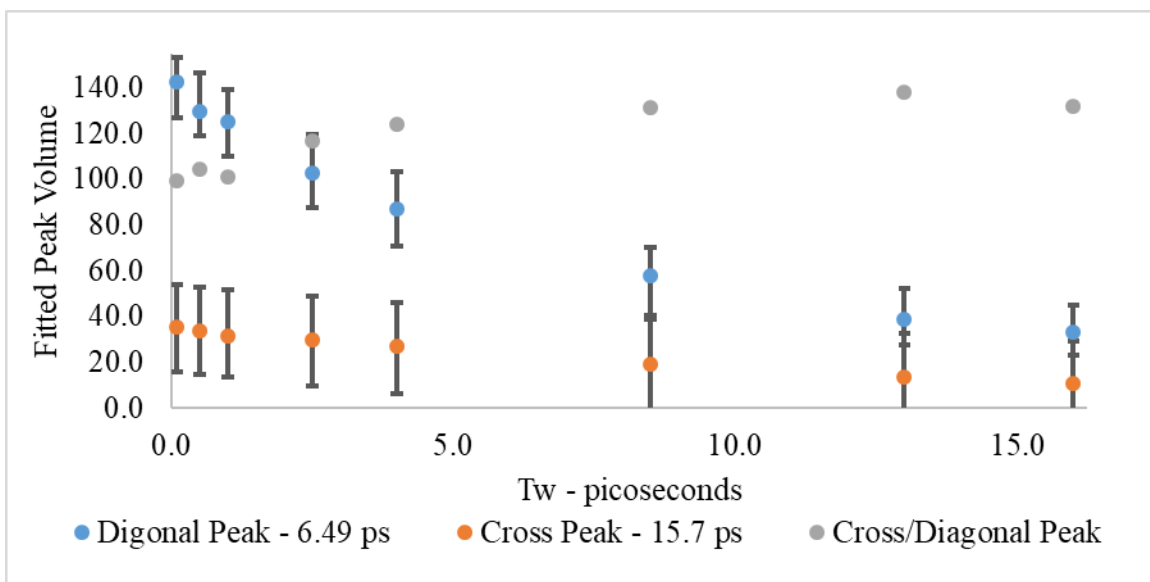
Figure 61: Analysis of on-diagonal, off-diagongal, and the off-diagonal peak volume divided by the on-diagonal peak volume for the N3 partially doped data resultant from fitting the spectra with 2 Gaussian peaks at a specific monochromator wavelength of 2140 cm^{-1}. Error bars indicate the 95% confidence interval calculated from fit errors and overlaid on data.

N3 in chloroform the off-diagonal region of the spectrum does not indicate exchange based on the signal decay (Figure 60). This agrees with kinetic modeling where a cross-peak treated as a species that is in equilibrium with either one or two species cannot increase while its reactant species decreases. This is also in agreement with exchange disappearing when N3 is fully doped with gaseous iodine in air. Figure 61 shows the peak volumes for the N3@TiO$_2$ partially doped with iodine along with their exponential decay constants. The cross-peak area decays more slowly than the on-diagonal indicating exchange. The cross-peak area to on-diagonal peak ratio is shown. Due to signal to noise and a vibrational lifetime that is significantly shorter than exchange time it was not possible to fit a reasonable time constant to cross peak data, though it qualitatively agrees with kinetic models.

6.8 Vibrational Lifetime Data and Fit Errors

We will summarize here by looking at vibrational lifetimes of N3 and Z907 for the on-diagonal peaks. Table 6 summarizes the vibrational lifetimes of the on-diagonal peaks for N3 and Z907 experiments. Fits were performed using single exponential decays, single exponential decays with a static offset, as well as double exponential decays. The thought was that the error would indicate whether multiple time scales were justified. This served to eliminate outliers such as the double exponential fit for Z907 doped with gaseous iodine where the error is one third of the longer time scale lifetime. Sorting through this table, there is one striking comparison. The lifetime of N3 increases (~2x) when doped with gaseous iodine while the lifetime of Z907 decreases (~2x).

There are no other clear trends. Data for all data sets were collected for 16 or 20 ps. This makes some of the longer time scales unreliable. The chloroform data for N3 has already been discussed and this data was not replicated with Z907. After analysis of the N3 in hexane with I_2 it was found that the peak had red-shifted along the diagonal over the course of the experiment indicating evaporation of hexane and a lack of I_2 dopant. Elucidating results would require significantly more experimental data.

Regarding the N3 and Z907 lifetime changes when doped with gaseous iodine, the double exponential fits have the highest error. Even in this case though one of the time constants is approximately the same while the other time constant increases for N3 and decreases for Z907. The replacement of two carboxylate moieties on a bipyridine ligand with nonyl chains are what defines Z907. One thing this does is limit the possible binding configurations to the TiO_2 nanoparticle surface. Based on Z907 having a longer lifetime in air this might indicate less efficient coupling with the phonon modes of the TiO_2 surface.

	Sinlge Exponential w/o Offset		Single Expoential w Offset		Double Exponential			
	Tau	2σ	Tau	2σ	Tau1	2σ	Tau2	2σ
N3	9.889	1.581	5.771	1.202	2.621	1.140	16.024	4.507
N3 wI2	21.202	4.413	8.746	3.391	1.718	1.018	31.553	7.371
N3 wHex	16.454	2.287	13.411	2.677	3.135	0.893	20.641	2.073
N3 wCHCl3	16.680	2.349	9.385	1.894	1.615	0.714	19.633	3.316
N3 wCHCl3 0.8 mg/ml I2	14.904	2.033	8.943	1.727	2.732	0.934	20.801	3.298
N3 wCHCl3 1.7 mg/ml I2	21.078	3.707	8.803	2.060	3.260	0.949	40.848	10.444
Z907	23.801	3.290	12.310	1.910	3.984	0.895	30.057	2.394
Z907 wI2	9.468	4.132	1.801	0.716	1.314	0.247	31.428	11.913
Z907 wHex	21.668	4.015	14.464	3.781	0.814	0.557	27.370	3.574
Z907 wHexI2	35.979	6.202	20.770	5.734	3.602	1.226	47.164	7.302

Table 6: Comparative fits for exponential decays on the given systems. Solvent and iodine amount were varied for N3 and Z907.

Since the nonyl changes would add a sort of bath of alkyl C-H stretches it would appear that these modes are not involved in vibrational relaxation as they would only make it faster. The distinct decrease in the vibrational lifetime of Z907 upon addition of gaseous iodine could be due to the Raman modes of iodine. Iodine has Raman modes at ~840 cm^{-1} and ~1040 cm^{-1}.[182] If the NCS stretch at ~2100 cm^{-1} relaxed into the alkyl C-H stretches or the aromatic C-H stretches between 2800 cm^{-1} and 3200 cm^{-1} this would be assisted by the iodine Raman modes. The alkyl C-H stretches are more likely as the lifetime of N3 gets longer upon the addition of gaseous iodine and N3 has the same aromatic C-H stretches as Z907.

The rationalization of the lengthening of lifetime in N3 upon iodine addition is more difficult. This is because the pathway is not known, and iodine must add additional modes. If this enabled relaxation of bath modes into the NCS vibrations then a similar effect would be expected in Z907. Another explanation of this would be a structural change in N3 upon interaction with iodine that prevented relaxation pathways for the NCS ligands. Indeed, the only calculation resulting in a blue-shift of the NCS ligands was when iodine molecules were polarized between the carboxyl hydrogen atom on the bipyridine ligand and the sulfur atom on the NCS stretch. This configuration was also more stable than any other iodine configurations by 10 kcal/mole. Eliminating two of these carboxyl moieties and instead having nonyl chains in these positions could certainly explain the stark difference in the vibrational lifetime changes due to iodine addition but detailed analysis, extensive computation, and further experimentation are necessary.

6.9 Future work On This System

These studies were initially aimed at measuring charge transfer in these films. This is discussed in appendix A. In pursuing this the comparative experiments outlined above were performed. The goal of this work was to highlight molecular structure and interactions based on the vibrational modes that were interrogated and connect these to other phenomena. While there are clear differences depending on solvent and molecular moieties, it is not straightforward to connect these to bulk phenomena. Molecular dynamics calculations were carried out to begin this exploration. This approach would be easily extended by automating the calculations of the vibrational frequencies for the individual MD structures. The results are suggestive that calculations using DFT can reproduce the 2D-IR spectra of a molecule. These systems were unique in their static heterogeneity which was explained using a continuum solvent model. Including explicit solvent would also be an improvement. Calculations also did not include the nanoparticle surface in any way.

Gaseous iodine has opposite effects on the vibrational lifetime of N3 and Z907. While interesting, it again is hard to connect to bulk phenomena without extensive analysis and further experiments. In the near term, the error in fits could be reduced by collecting more data. Every point lowers the calculated error and later T_w points would differentiate timescales.

6.10 Conclusions

These N3 and Z907 experimental results, though incomplete, lay a strong foundation for continuing experiments. The nature of the I_2 interaction, analogue study, as well as computational support are the immediate directions of future work. All other

chapters come from published works and form the foundation for exchange experiments in heterogeneous thin films. This document outlined the general theory behind the spectroscopy and the phenomenon studied. While 2D-IR rests on quantum mechanical theory, all the results are treated classically. This is true for electric fields and scatter, for the kinetics of exchange and the Arrhenius relationship, or exponential decays as a function of vibrational frequency in SiNPs. Though most analysis amounted to exponential fits, at least a firm qualitative grasp of the quantum mechanics must be in hand to rationalize results as was seen in N3 and Z907. This is enough to analyze data but to design new experiments and truly analyze molecular level phenomena a firm theoretical grasp is required. This work is a step towards connecting bulk behavior to molecular properties.

Bibliography

[1] S. Mukamel, *Principles of nonlinear optical spectroscopy* (New York ; Oxford : Oxford University Press, New York ; Oxford, 1995), Book, Whole

[2] D. A. Skoog, *Principles of instrumental analysis* (Belmont, Calif. : Thomson Brooks/Cole, Belmont, Calif.

Belmont, CA, 2007), 6th ed. / Douglas A. Skoog, F. James Holler, Stanley R. Crouch.. edn., 116.

[3] P. Hamm *et al.*, Proceedings of the National Academy of Sciences of the United States of America **96** (1999) 2036.

[4] P. Hamm, M. Lim, and R. M. Hochstrasser, Physical Review Letters **81** (1998) 5326.

[5] P. Hamm, M. H. Lim, and R. M. Hochstrasser, Journal of Physical Chemistry B **102** (1998) 6123.

[6] A. L. Le Sueur, R. E. Horness, and M. C. Thielges, Analyst **140** (2015) 4336.

[7] S. T. van der Post *et al.*, Nature Communications **6**, 8384 (2015)

[8] L. De Marco *et al.*, The Journal of chemical physics **145** (2016) 094501.

[9] A. D. Hill *et al.*, Journal of Physical Chemistry B **117** (2013) 15346.

[10] M. B. Ji, M. Odelius, and K. J. Gaffney, Science **328** (2010) 1003.

[11] K. W. Kwak, S. Park, and M. D. Fayer, Proceedings of the National Academy of Sciences of the United States of America **104** (2007) 14221.

[12] I. A. Nilsen *et al.*, Journal of Chemical Physics **141**, 134313 (2014)

[13] M. T. Zanni *et al.*, Proceedings of the National Academy of Sciences of the United States of America **98** (2001) 11265.

[14] F. Bloch, Physical Review **70** (1946) 460.

[15] U. Fano, Reviews of Modern Physics **29** (1957) 74.

[16] P. Hamm, *Concepts and methods of 2D infrared spectroscopy* (Cambridge ; New York : Cambridge University Pres, Cambridge ; New York, 2011), Book, Whole

[17] J. Von Neumann, *Mathematical foundations of quantum mechanics* (Princeton N.J.] Princeton University Press, Princeton N.J., 1955), Book, Whole

[18] V. M. Kenkre, A. Tokmakoff, and M. D. Fayer, Journal of Chemical Physics **101** (1994) 10618.

[19] A. Tokmakoff, B. Sauter, and M. D. Fayer, Journal of Chemical Physics **100** (1994) 9035.

[20] D. Q. Xiao *et al.*, Nano Letters **9** (2009) 1818.

[21] I. V. Rubtsov, Accounts of Chemical Research **42** (2009) 1385.

[22] A. A. Eigner, T. C. Anglin, and A. M. Massari, Journal of Physical Chemistry C **114** (2010) 12308.

[23] B. H. Jones *et al.*, Journal of Chemical Physics **142** (2015) 212441.

[24] K. M. Slenkamp *et al.*, Journal of Chemical Physics **140**, 084505 (2014)

[25] C. R. Baiz *et al.*, Accounts of Chemical Research **42** (2009) 1395.

[26] I. C. Spector *et al.*, Journal of physical chemistry. C **122** (2018) 8693.

[27] D. M. Jonas, Annual Review of Physical Chemistry **54** (2003) 425.

[28] S. M. G. Faeder, and D. M. Jonas, Journal of Physical Chemistry a **103** (1999) 10489.

[29] K. Kwak, D. E. Rosenfeld, and M. D. Fayer, Journal of Chemical Physics **128** (2008) 204505.

[30] M. Volk *et al.*, The journal of physical chemistry. B **101** (1997) 8607.

[31] P. Hamm, and M. T. Zanni, *Concepts and Methods of 2D Infrared Spectroscopy* (Cambridge University Press, Cambridge, 2011),

[32] S. Park, K. Kwak, and M. D. Fayer, Laser Physics Letters **4** (2007) 704.

[33] D. A. McQuarrie, *Statistical mechanics* (New York : Harper & Row, New York, 1976), Book, Whole

[34] R. Freeman, *Spin choreography : basic steps in high resolution NMR* (Oxford : Oxford University Press, Oxford, 1997), Book, Whole

[35] C. Cohen-Tannoudji, *Quantum mechanics* (New York : Wiley, New York, 1977), Book, Whole

[36] M. D. Fayer, *Elements of quantum mechanics* (New York : Oxford University Press, New York, 2001), Book, Whole

[37] K. Blum, *Density matrix theory and applications* (Berlin ; New York : Springer, Berlin ; New York, 2012), Book, Whole

[38] A. Tokmakoff, 2013).

[39] D. J. Griffiths, *Introduction to electrodynamics* (Upper Saddle River, N.J. : Prentice Hall, Upper Saddle River, N.J., 1999), Book, Whole

[40] F. Ding, E. C. Fulmer, and M. T. Zanni, Journal of Chemical Physics **123** (2005) 094502.

[41] B. H. Jones, C. J. Huber, and A. M. Massari, J. Phys. Chem. C **115** (2011) 24813.

[42] A. C. Eckbreth, Applied Physics Letters **32** (1978) 421.

[43] M. Khalil, N. Demirdoven, and A. Tokmakoff, Journal of Physical Chemistry A **107** (2003) 5258.

[44] J. T. King, J. M. Anna, and K. J. Kubarych, Phys. Chem. Chem. Phys. **13** (2011) 5579.

[45] C. J. Fecko *et al.*, Science **301** (2003) 1698.

[46] M. D. Fayer *et al.*, Accounts of Chemical Research **42** (2009) 1210.

[47] M. Ji, and K. J. Gaffney, Journal of Chemical Physics **134** (2011)

[48] S. H. Shim *et al.*, Proceedings of the National Academy of Sciences of the United States of America **106** (2009) 6614.

[49] C. Kolano *et al.*, Nature **444** (2006) 469.

[50] M. Lim, P. Hamm, and R. M. Hochstrasser, Proc. Natl. Acad. Sci. USA **95** (1998) 15315.

[51] W. Xiong *et al.*, Journal of the American Chemical Society **131** (2009) 18040.

[52] C. J. Huber, and A. M. Massari, Journal of Physical Chemistry C **118** (2014) 25567.

[53] A. A. Eigner *et al.*, Journal of Physical Chemistry B **115** (2011) 8686.

[54] F. Perakis, and P. Hamm, Physical Chemistry Chemical Physics **14** (2012) 6250.

[55] M. Khalil, N. Demirdoven, and A. Tokmakoff, Physical Review Letters **90** (2003) 047401.

[56] B. L. McClain, I. J. Finkelstein, and M. D. Fayer, Chem. Phys. Lett. **392** (2004) 324.

[57] R. Bloem *et al.*, Optics express **18** (2010) 27067.

[58] N. Demirdoven *et al.*, Optics Letters **27** (2002) 433.

[59] S. H. Shim *et al.*, Proceedings of the National Academy of Sciences of the United States of America **104** (2007) 14197.

[60] B. H. Jones, and A. M. Massari, Journal of Physical Chemistry B **117** (2013) 15741.

[61] L. P. DeFlores, R. A. Nicodemus, and A. Tokmakoff, Optics Letters **32** (2007) 2966.

[62] E. R. Nelsen, A. C. Brezny, and C. R. Landis, Journal of the American Chemical Society **137** (2015) 14208.

[63] N. A. Anderson, J. J. Shiang, and R. J. Sension, Journal of Physical Chemistry A **103** (1999) 10730.

[64] R. B. Dyer *et al.*, Journal of the American Chemical Society **113** (1991) 6276.

[65] Z. D. Pardo *et al.*, Journal of the American Chemical Society **134** (2012) 2706.

[66] D. Stoner-Ma *et al.*, Journal of the American Chemical Society **127** (2005) 2864.

[67] D. T. Valley, D. P. Hoffman, and R. A. Mathies, Physical Chemistry Chemical Physics **17** (2015) 9231.

[68] D. P. Zhong, Current Opinion in Chemical Biology **11** (2007) 174.

[69] Y. Shvo *et al.*, Journal of the American Chemical Society **108** (1986) 7400.

[70] Y. Shvo *et al.*, Organometallics **16** (1997) 133.

[71] B. L. Conley *et al.*, Chemical reviews **110** (2010) 2294.

[72] Z. Y. Lu, B. L. Conley, and T. J. Williams, Organometallics **31** (2012) 6705.

[73] M. C. Warner, C. P. Casey, and J. E. Backvall, in *Bifunctional Molecular Catalysis*, edited by T. Ikariya, and M. Shibasaki2011), pp. 85.

[74] C. P. Casey, and J. B. Johnson, Journal of the American Chemical Society **127** (2005) 1883.

[75] C. P. Casey, S. E. Beetner, and J. B. Johnson, Journal of the American Chemical Society **130** (2008) 2285.

[76] M. D. Fayer, Annual Review of Physical Chemistry **60** (2009) 21.

[77] C. P. Casey *et al.*, Journal of the American Chemical Society **123** (2001) 1090.

[78] M. J. T. Frisch, G. W.; Schlegel, H. B.; Scuseria, G. E.; Robb, M. A.; Cheeseman, J. R.; Scalmani, G.; Barone, V.; Mennucci, B.; Petersson, G. A.; Nakatsuji, H.; Caricato, M.; Li, X.; Hratchian, H. P.; Izmaylov, A. F.; Bloino, J.; Zheng, G.; Sonnenberg, J. L.; Hada, M.; Ehara, M.; Toyota, K.; Fukuda, R.; Hasegawa, J.; Ishida, M.; Nakajima, T.; Honda, Y.; Kitao, O.; Nakai, H.; Vreven, T.; Montgomery, J. A., Jr.; Peralta, J. E.; Ogliaro, F.; Bearpark, M.; Heyd, J. J.; Brothers, E.; Kudin, K. N.; Staroverov, V. N.; Kobayashi, R.; Normand, J.; Raghavachari, K.; Rendell, A.; Burant, J. C.; Iyengar, S. S.; Tomasi, J.; Cossi, M.; Rega, N.; Millam, N. J.; Klene, M.; Knox, J. E.; Cross, J. B.; Bakken, V.; Adamo, C.; Jaramillo, J.; Gomperts, R.; Stratmann, R. E.; Yazyev, O.; Austin, A. J.; Cammi, R.; Pomelli, C.; Ochterski, J. W.; Martin, R. L.; Morokuma, K.; Zakrzewski, V. G.; Voth, G. A.; Salvador, P.; Dannenberg, J. J.; Dapprich, S.; Daniels, A. D.; Farkas, Ö.; Foresman, J. B.; Ortiz, J. V.; Cioslowski, J.; Fox, D. J. , *Gaussian 09, revision A.02* Wallington, CT, 2009),

[79] M. L. Laury, M. J. Carlson, and A. K. Wilson, Journal of Computational Chemistry **33** (2012) 2380.

[80] B. H. Jones, C. J. Huber, and A. M. Massari, Journal of Physical Chemistry A **117** (2013) 6150.

[81] Y. Kwon, C. Lee, and S. Park, Chemical Physics **445** (2014) 38.

[82] Y. Ahn *et al.*, Coordination Chemistry Reviews **252** (2008) 647.

[83] C. P. Casey, and H. R. Guan, Organometallics **31** (2012) 2631.

[84] R. Karvembu, R. Prabhakaran, and K. Natarajan, Coordination Chemistry Reviews **249** (2005) 911.

[85] L. De Marco *et al.*, Journal of Chemical Physics **141**, 034502 (2014) 034502.

[86] M. Khalil, N. Demirdoven, and A. Tokmakoff, Journal of Chemical Physics **121** (2004) 362.

[87] K. J. Gaffney *et al.*, Chemical Physics Letters **504** (2011) 1.

[88] T. L. C. Jansen, and J. Knoester, Accounts of Chemical Research **42** (2009) 1405.

[89] J. King, M. Ross, and K. Kubarych, Journal of Physical Chemistry B **116** (2012) 3754.

[90] P. Hamm, M. Lim, and R. M. Hochstrasser, Journal of Chemical Physics **107** (1997) 10523.

[91] H. G. Schuster-Woldan, and F. Basolo, J. Am. Chem. Soc **88** (1966) 1657.

[92] D. E. Moilanen *et al.*, Proceedings of the National Academy of Sciences of the United States of America **106** (2009) 375.

[93] S. Park, M. Odelius, and K. J. Gaffney, Journal of Physical Chemistry B **113** (2009) 7825.

[94] H. J. Bakker, Journal of Chemical Physics **98** (1993) 8496.

[95] Z. Luz, and S. Meiboom, J. Am. Chem. Soc **86** (1964) 4768.

[96] U. R. Kortshagen *et al.*, Chemical Reviews **116** (2016) 11061.

[97] K. A. Perrine, and A. V. Teplyakov, Chemical Society Reviews **39** (2010) 3256.

[98] M. A. Boles *et al.*, Nature Materials **15** (2016) 141.

[99] Z. Guo, and L. Tan, *Fundamentals and Applications of Nanomaterials* (Artech House, Norwood, 2009), Fundamentals and Applications of Nanomaterials,

[100] M. Garin *et al.*, Nature Communications **5**, 3440 (2014)

[101] M. Garin *et al.*, Journal of Applied Physics **119**, 033101 (2016) 033101.

[102] J. S. Biteen *et al.*, Nano Letters **5** (2005) 1768.

[103] A. G. Cullis, and L. T. Canham, Nature **353** (1991) 335.

[104] A. G. Cullis, L. T. Canham, and P. D. J. Calcott, Journal of Applied Physics **82** (1997) 909.

[105] D. J. Rowe *et al.*, Nano Letters **13** (2013) 1317.

[106] B. Z. Tian *et al.*, Nature **449** (2007) 885.

[107] J. J. Wu, and U. R. Kortshagen, RSC Advances **5** (2015) 103822.

[108] R. M. Rioux *et al.*, Topics in Catalysis **39** (2006) 167.

[109] E. Hao, G. C. Schatz, and J. T. Hupp, Journal of Fluorescence **14** (2004) 331.

[110] A. R. Tao, S. Habas, and P. D. Yang, Small **4** (2008) 310.

[111] J. H. Yu *et al.*, Journal of the American Chemical Society **127** (2005) 5662.

[112] Y. N. Xia *et al.*, Angewandte Chemie-International Edition **48** (2009) 60.

[113] C. B. Murray, D. J. Norris, and M. G. Bawendi, Journal of the American Chemical Society **115** (1993) 8706.

[114] X. G. Peng *et al.*, Nature **404** (2000) 59.

[115] H. F. Wilson, and A. S. Barnard, Journal Of Physical Chemistry C **118** (2014) 2580.

[116] X. Sun *et al.*, Inorganic Chemistry **42** (2003) 2398.

[117] X. Zhang *et al.*, Applied Physics Letters **79** (2001) 4051.

[118] X. Li, Y. He, and M. T. Swihart, Langmuir **20** (2004) 4720.

[119] B. Teo, Coordination Chemistry Reviews **246** (2003) 229.

[120] H. Touir, K. Zellama, and J. F. Morhange, Physical Review B - Condensed Matter and Materials Physics **59** (1999) 10076.

[121] M. Hines *et al.*, Physical Review Letters **71** (1993) 2280.

[122] B. Sun *et al.*, Physical Review Letters **96** (2006) 035501.

[123] C. J. Huber *et al.*, Journal of Physical Chemistry C **119** (2015) 25135.

[124] C. J. Huber, R. L. Butler, and A. M. Massari, The Journal of Physical Chemistry C **121** (2017) 2933.

[125] G. Lucovsky, Solid State Communications **29** (1979) 571.

[126] G. Lucovsky, R. J. Nemanich, and J. C. Knights, Physical Review B **19** (1979) 2064.

[127] Y. J. Chabal, A. L. Harris, and K. Raghavachari, International Journal of Modern Physics B **7** (1993) 1031.

[128] P. Guyot Sionnest, P. Lin, and E. Hiller, The Journal of Chemical Physics **102** (1995) 4269.

[129] J. W. Lyding, K. Hess, and I. C. Kizilyalli, Applied Physics Letters **68** (1996) 2526.

[130] P. Guyot-Sionnest *et al.*, Physical Review Letters **64** (1990) 2156.

[131] P. Guyot-Sionnest, P. Dumas, and Y. J. Chabal, Journal of Electron Spectroscopy and Related Phenomena **54-55** (1990) 27.

[132] P. Guyot-Sionnest, P.-H. Lin, and E. M. Hiller, The Journal of Chemical Physics **102** (1995) 4269.

[133] K. Kuhnke *et al.*, The Journal of Chemical Physics **99** (1993) 6114.

[134] K. Jobson *et al.*, Physical Review B **74** (2006) 165205.

[135] v. D. V. M *et al.*, Physical Review Letters **84** (2000) 1236.

[136] C. W. Rella *et al.*, Applied Physics Letters **75** (1999) 2945.

[137] Z. Xu *et al.*, Journal of Non- … (1996)

[138] G. Lüpke, N. H. Tolk, and L. C. Feldman, Journal Of Applied Physics **93** (2003) 2317.

[139] N. J. Kramer, K. S. Schramke, and U. R. Kortshagen, Nano Letters **15** (2015) 5597.

[140] I. C. Spector *et al.*, Optics Letters **40** (2015) 1850.

[141] J. R. Zheng *et al.*, Science **309** (2005) 1338.

[142] N. M. Park *et al.*, Chem. Vapor Depos. **8** (2002) 254.

[143] V. Burrows *et al.*, Applied Physics Letters **53** (1988) 998.

[144] Y. Chabal *et al.*, Journal of Vacuum Science & Technology A **7** (1989) 2104.

[145] Y. J. Chabal, Physica B: Condensed Matter (1991)

[146] P. Jakob, and Y. Chabal, The Journal of Chemical Physics **95** (1991) 2897.

[147] A. A. Langford *et al.*, Physical Review B **45** (1992) 13367.

[148] P. J. H. Denteneer, C. G. Van De Walle, and S. T. Pantelides, Physical Review B **39** (1989) 10809.

[149] P. Guyot-Sionnest, Physical Review Letters **66** (1991) 1489.

[150] X. P. Zhang *et al.*, Energy & Environmental Science **5** (2012) 6668.

[151] S. C. Roy *et al.*, Acs Nano **4** (2010) 1259.

[152] S. T. Munkejord, M. Hammer, and S. W. Lovseth, Applied Energy **169** (2016) 499.

[153] M. Mikkelsen, M. Jorgensen, and F. C. Krebs, Energy & Environmental Science **3** (2010) 43.

[154] S. N. Habisreutinger, L. Schmidt-Mende, and J. K. Stolarczyk, Angewandte Chemie-International Edition **52** (2013) 7372.

[155] T. Konno, and Y. Ozaki, Chem. Phys. Lett. **394** (2004) 198.

[156] J. A. Oneill *et al.*, J. Chem. Phys. **88** (1988) 6240.

[157] M. A. Walsh *et al.*, Chem. Phys. Lett. **142** (1987) 265.

[158] M. Morgen *et al.*, Chem. Phys. Lett. **209** (1993) 1.

[159] *Spectroscopy: Volume 2* (Chapman and Hall, London, 1976), Vol. 2, 184-187.

[160] A. Mandal *et al.*, Phys. Rev. Lett. **120**, 103401 (2018) 6.

[161] K. Wakatsuki *et al.*, Proceedings of the Combustion Institute **30** (2005) 1565.

[162] IUPAC, *Tables of wavenumbers for the calibration of infra-red spectrometers* (Butterworths, Washington, 1961),

[163] P. J. Ogren, J. Chem. Educ. **79** (2002) 117.

[164] G. Herzberg, *Molecular Spectra and Molecular Structure III. Electronic Spectra and Electronic Structure of Polyatomic Molecules* (Van Nostrand, New York, 1966), 598.

[165] Q. Wang *et al.*, Journal of the American Chemical Society **128** (2006) 4446.

[166] B. Oregan, and M. Gratzel, Nature **353** (1991) 737.

[167] P. Wang *et al.*, Journal of Physical Chemistry B **108** (2004) 17553.

[168] P. Wang *et al.*, Journal of Physical Chemistry B **107** (2003) 14336.

[169] A. Khataee, and G. A. Mansoori, *Nanostructured Titanium Dioxide Materials: Properties, Preparation And Applications* (Singapore: World Scientific Publishing Company, Singapore, 2011),

[170] G. Hashmi *et al.*, Renewable and Sustainable Energy Reviews **15** (2011) 3717.

[171] B. Van Der Zanden, and A. Goossens, Journal of Physical Chemistry B **104** (2000) 7171.

[172] N. Martsinovich, F. Ambrosio, and A. Troisi, Physical chemistry chemical physics : PCCP **14** (2012) 16668.

[173] D. G. Truhlar, https://comp.chem.umn.edu/freqscale/index.html, 2020).

[174] Y. Zhao, and D. G. Truhlar, Accounts of chemical research **41** (2008) 157.

[175] Y. Zhao, and D. G. Truhlar, Theoretical chemistry accounts **120** (2007) 215.

[176] Y. Zhao, and D. G. Truhlar, Journal of Chemical Physics **125** (2006) 194101.

[177] O. Kohle *et al.*, Advanced Materials **9** (1997) 904.

[178] I. M. Alecu *et al.*, Journal of chemical theory and computation **6** (2010) 2872.

[179] J. H. Espenson, *Chemical kinetics and reaction mechanisms* (New York : McGraw-Hill : Primis Custom, New York, 2002), 2nd ed.. edn.,

[180] R. P. Feynman, *The Feynman lectures on physics* (Reading, Mass., Addison-Wesley Pub. Co, Reading, Mass., 1963), Book, Whole

[181] D. J. Griffiths, *Introduction to quantum mechanics* (Englewood Cliffs, N.J. : Prentice Hall, Englewood Cliffs, N.J., 1995),

[182] W. Kiefer, and H. J. Bernstein, Journal of Raman spectroscopy **1** (1973) 417.

[183] A. Troisi, Chemical Society Reviews **40** (2011) 2347.

[184] J. Jortner, and M. Ratner, *Molecular electronics* (Osney Mead, Oxford England] ; Malden, MA, USA : Blackwell Science, Osney Mead, Oxford England] ; Malden, MA, USA, 1997), Book, Whole 5-28.

[185] V. Coropceanu *et al.*, Chemical reviews **107** (2007) 926.

[186] A. C. Arias *et al.*, Chemical reviews **110** (2010) 3.

[187] F. A. Hegmann *et al.*, Physical Review Letters **89** (2002) 2274031.

[188] C. J. Huber *et al.*, Journal of Physical Chemistry a **116** (2012) 9279.

[189] M. Bixon, and J. Jortner, Chemical Physics **176** (1993) 467.

[190] F. De Angelis, S. Fantacci, and A. Selloni, Nanotechnology **19** (2008)

[191] M. K. Nazeeruddin *et al.*, Langmuir **16** (2000) 8525.

[192] C. Klein *et al.*, Inorganic chemistry **43** (2004) 4216.

[193] Z. P. Zhang *et al.*, Journal of Physical Chemistry B **109** (2005) 21818.

[194] M. K. Nazeeruddin *et al.*, Coordination Chemistry Reviews **249** (2005) 1460.

[195] M. K. Nazeeruddin *et al.*, Journal of the American Chemical Society **127** (2005) 16835.

[196] Solaronix, 2013).

[197] H. Powell, E. Fergusson, and M. Bryant, Australian Journal of Chemistry **24** (1971) 257.

[198] J. Stephan, S. Schrader, and L. Brehmer, Synthetic Metals **111** (2000) 353.

[199] R. J. Chesterfield *et al.*, Journal of Physical Chemistry B **108** (2004) 19281.

[200] J. Larmor, Proceedings of the Physical Society of London **14** (1895) 303.

[201] A. H. Wilson, Proceedings of the Royal Society of London **134** (1931) 277.

[202] Y. Takahashi, Proceedings of the Physico-Mathematical Society of Japan **3** (1921) 20.

[203] Y. Li, V. Coropceanu, and J.-L. Bredas, Journal of Physical Chemistry Letters **3** (2012) 3325.

[204] M. Ohno, Journal of Electron Spectroscopy and Related Phenomena **154** (2007) 101.

[205] J. S. Kang *et al.*, Physical Review B **56** (1997) 10605.

[206] A. Saeki *et al.*, Accounts of Chemical Research **45** (2012) 1193.

[207] A. R. Brown *et al.*, Synthetic Metals **88** (1997) 37.

[208] Thorton, Stephen et al., Modern Physics for Scientists and Engineers, (Thomson Brooks/Cole, 2006), Book, Whole

[209] S. I. Kubarev, Teoreticheskaya i Eksperimental'naya Khimiya **2** (1966) 486.

[210] R. A. Marcus, Angewandte Chemie (International Edition in English) **32** (1993) 1111.

[211] R. A. Marcus, The Journal of Chemical Physics **24** (1956) 966.

[212] J. L. Bredas *et al.*, Chemical reviews **104** (2004) 4971.

[213] N. Sutin, Progress in Inorganic Chemistry **30** (1983) 441.

[214] J. Hubbard, Proceedings of the Royal Society of London, Series A (Mathematical and Physical Sciences) **276** (1963) 238.

[215] J. Hubbard, Proceedings of the Royal Society of London, Series A (Mathematical and Physical Sciences) **277** (1964) 237.

[216] J. Hubbard, Proceedings of the Royal Society of London, Series A (Mathematical and Physical Sciences) **281** (1964) 401.

[217] H. Sirringhaus, Advanced Materials **17** (2005) 2411.

[218] R. H. Goldsmith *et al.*, Journal of Physical Chemistry a **112** (2008) 4410.

[219] M. Bixon, and J. Jortner, Journal of Physical Chemistry **97** (1993) 13061.

[220] R. A. Marcus, and N. Sutin, Biochimica et Biophysica Acta (BBA) - Reviews on Bioenergetics **811** (1985) 265.

[221] R. A. Marcus, The Journal of Chemical Physics **24** (1956) 979.

[222] M. Pope, *Electronic processes in organic crystals and polymers* (New York : Oxford University Press, New York, 1999), Book, Whole

[223] S. I. Kubarev, and I. D. Mikhailov, Theoretical and Experimental Chemistry **1** (1965) 148.

[224] M. Lax, Physical Review **109** (1958) 1921.

[225] H. A. v. Laarhoven *et al.*, Journal of Chemical Physics **129** (2008) 044704.

[226] A. Troisi, G. Orlandi, and J. E. Anthony, Chemistry of Materials **17** (2005) 5024.

[227] A. Troisi, D. L. Cheung, and D. Andrienko, Physical Review Letters **102** (2009)

[228] B. C. O'Regan *et al.*, Journal of Physical Chemistry B **110** (2006) 17155.

[229] L. Q. Jing *et al.*, Journal of Physics and Chemistry of Solids **64** (2003) 615.

[230] V. Mankad, S. K. Gupta, and P. K. Jha, Physica E-Low-Dimensional Systems & Nanostructures **44** (2011) 614.

[231] T. Holstein, Annals of Physics **8** (1959) 325.

[232] T. Holstein, Annals of Physics **8** (1959) 343.

[233] J. R. Bolton, N. Mataga, and G. McLendon, Advances in Chemistry Series (1991) 1.

[234] T. J. Meyer, Progress in Inorganic Chemistry **30** (1983) 389.

[235] Adv.chem.ser. (1950)

[236] T. Holstein, Annals of Physics **8** (1959) 325.

[237] T. Holstein, Annals of Physics **8** (1959) 343.

[238] J. M. Marshall, Philosophical Magazine Letters **80** (2000) 691.

[239] S. Stafstrom, Chemical Society Reviews **39** (2010) 2484.

[240] F. C. Grozema, and L. D. A. Siebbeles, International Reviews in Physical Chemistry **27** (2008) 87.

[241] Y. A. Berlin *et al.*, Journal of Physical Chemistry a **107** (2003) 3970.

[242] S. Ardo, and G. J. Meyer, Journal of the American Chemical Society **132** (2010) 9283.

[243] S. Ardo, and G. J. Meyer, Journal of the American Chemical Society **133** (2011) 15384.

[244] E. Siliņš, *Organic molecular crystals : interaction, localization, and transport phenomena* (New York : American Institute of Physics, New York, 1994), Book, Whole

[245] *The One-Dimensional Hubbard Model* (Cambridge : Cambridge University Press, Cambridge, 2005), Book, Whole

[246] S. Efrima, and H. Metiu, Chemical Physics Letters **60** (1979) 226.

[247] G. D. Scholes, and G. Rumbles, Nature Materials **5** (2006) 683.

[248] X. Li *et al.*, Physical Chemistry Chemical Physics **14** (2012) 15421.

Appendix A: Charge Transfer in Dye Sensitized Solar Cell Films

Two article databases (Scopus and Web of Science) located over 1,000 papers pertaining to CT in 1998 when the first vibrational echo experiments were performed. This is compared to dozens in the 1970's and hundreds through the 1980's. Papers on the topic of CT have tripled since 1993 but it is surprising how little is still known about CT in organic systems.[183] Charge transport in organic electronics (OEs) can include: redox reactions or charge hopping, conduction in organic electronic devices such as organic field effect transistors (OFETs), and conduction in molecular-size electronic devices and wires.[184] Improving CT would improve the cost and efficiency of OEs. One major obstacle to widespread application of OEs is the ability to process high mobility OE devices in solution.[22, 185, 186]

Charge mobility is an intrinsic material property that describes how fast charge carriers move for a given applied field. High mobility has been achieved in single crystals of a variety of OEs but solution processing does not typically lead to single crystals.[185] Ultra-pure single crystals of pentacene have mobilities on the order of 1 cm^2 V^{-1} s^{-1}.[187] Ballistic transport along the length of a single walled carbon nanotube corresponds to a charge mobility of 80000 cm^2 V^{-1} s^{-1}. Disordered organic materials often have charge mobilities that fall between 10^{-6} and 10^{-3} cm^2 V^{-1} s^{-1}.[185] Solution processed OEs appear to have a mobility ceiling of less than 1 cm^2 V^{-1} s^{-1}.[183, 185, 186]

There are two main reasons to utilize a vibrational spectroscopic technique to study CT in OEs. The first is that the ground electronic state can be observed which may not be the case for visible spectroscopies. Ground and excited electronic states will be affected

differently by vibrational dynamics. The second reason is to explore the effects of vibrational dynamics on CT.

It is difficult to perturb the vibrational environment without perturbing the electronic environment. One way to do this is through annealing where the off-diagonal, or between site coupling, is modulated by morphology.[22] Another way is to change the solution around a species of interest which has been shown to effect electron transfer.[41, 188, 189] In this system it is not clear what effect the TiO_2 nanoparticle low frequency vibrations play but there is no absorbance from 500 to 4000 cm^{-1} to interfere with chromophores being measured. Annealing is not likely to have an effect as the films are already sintered at 773 K but different nanoparticle diameters might have been a way to change the environment due to interparticle molecular distances. This should perturb static disorder. Though it would change the concentration another way is with an HDMA co-adsorbent with Z907.[168] Varying the ratio of HDMA to Z-907 was a third way to modulate the environment. Then to test perturbations to the ligand environment and the hypothesis that charge hopping occurs via the NCS^- ligands the CN^- analogue of N3 could be studied.[165] Even if CT would have been measured in analogues in which the electronic structure is not exactly the same it may still have been possible to draw general conclusions about how vibrational environment and dynamics affect CT. Ideally these conclusions would have pointed to how to tune vibrational environment for optimal charge transfer. It was intended to form a collaboration with a computational researcher to correlate frequency to vibrational environment. It was also hoped that a model can be formed using the general equations outlined above to complement experiment with theory.

A.1 DSSC Charge Transfer
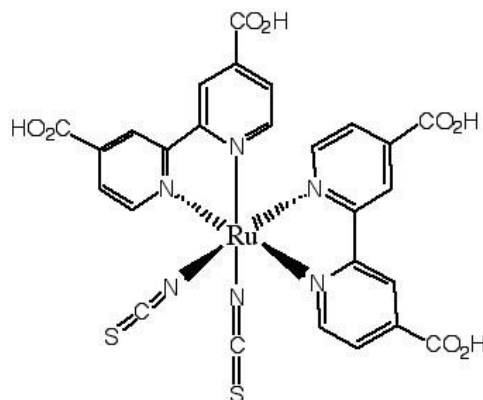
Figure 62: The ruthenium dye N3.

Research on DSSC films began as the pursuit of an observation through 2D-IR of CT between molecules of a popular dye. The system proposed for study was a self-assembled monolayer of the ruthenium dye N3 (figure 3), on a dye-sensitized solar cell (DSSC) platform because of reports of reasonably high surface charge transfer through a variety of SAMs of dyes including N3 (figure 3) and Z907 (figure 4)..[166, 190] [25] DSSC platforms involve a SAM of a strongly absorbing molecule bound to a metal oxide film. The most common systems utilize ruthenium dyes bound via carboxylate moieties to a titanium dioxide (TiO_2) nanoparticle film. These were popularized by Graetzel and coworkers because of their ease of preparation and high efficiency of photon conversion.[165-167, 191-195] This system was meant to enable convenient study of a series of analogues or coadsorbants because analytes need only possess a carboxylate group to be tethered to the TiO_2 nanoparticle substrate. The dye analogues possessing isothiocyanate (NCS⁻) ligands. Metal bound infrared chromophores such as carbonyl, cyanide, cyanate, or thiocyanate ligands usually have strong signal and long vibrational lifetimes making them ideal for 2D-IR. The N3 dye was particularly ideal to begin with because it is believed that charge hopping is facilitated directly through the NCS⁻ ligands which suggested a high

probability of observing CT.[165] Studies of CT through a SAM of N3 was meant to lay the groundwork for a comparative study.

Initial data collected from experiments on N3 was suggestive of measurable CT. so work began on Z907.[196] Alkyl chains away from the metal center would have hopefully perturbed vibrational dynamics with little other effect on the mechanism of CT.[167] After
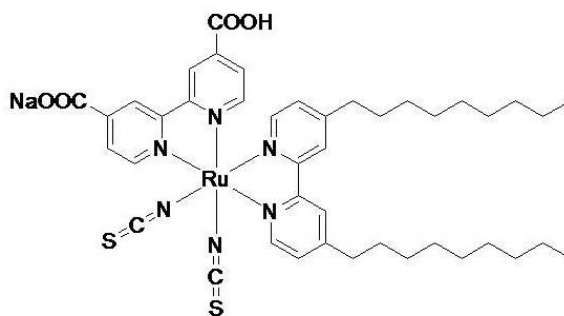
Figure 63: Z907 analogue

single component systems had been studied, coadsorption of other species such as hexadecyl-malonic acid (HDMA, figure 5) was planned along with cyanide and iron center analouges.[168] [197] Iron centers were aimed at investigating metal and ligand effects on CT.[197] Thus a comparative study through a variety of complexes, coadsorbants, and varying component compositions was proposed.
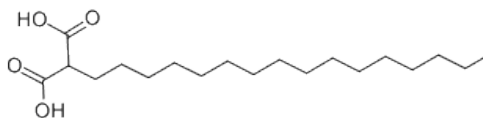
Figure 64: Hexadecyl malonic acid.

The Salient effects on charge mobility that are to be explored are modulation of wavefunction overlap by vibrational dynamics and the availability of low frequency vibrational modes giving rise to the dynamics of interest. This timescale measurable by 2D-IR of 100 fs to 200 picoseconds (ps) corresponds to the period of vibrations up to 200 cm^{-1}. This is what is meant by low frequency vibrational modes. The energy of a 200 cm^{-}

139

vibration is approximately 25 meV which is also approximately $k_B T$ at room temperature so temperature studies were also intended to illuminate some of the effects of vibrational Dynamics on CT.[198, 199]

A.2 Early Studies of CT

Study of CT predates discovery of the electron (the name 'electron' predates knowledge of its fundamental charge and mass).[200] One of the earliest theories describing CT is band theory which is still popular today.[201] Bands originally referred to continuous regions of absorption spectra.[201, 202] The density of states within a band as well as their occupation will affect charge mobility. Electronic energy bandwidth is proportional to the spatial extent and overlap of the wavefunctions composing a given sample.[183, 203-205] Metals have bandwidths greater than 1 eV, bands that are continuous, can be partially filled, and charge mobilities on the order of 1 cm^2 V^{-1} s^{-1} or greater. Highly conductive metals have charge mobilities on the order of 10^4 cm^2 V^{-1} s^{-1} while single crystal silicon has a mobility of roughly 10^3 cm^2 V^{-1} s^{-1}.[206-208] Pentacene single crystals have charge mobilities of 2.3 cm^2 V^{-1} s^{-1} and a bandwidth of roughly 0.5 meV.[203] Pentacene mobility is decreased substantially in solution processed films. For an isolated molecule its wavefunction is localized to itself and would be nearer a δ delta function. In this case the energy of states would be discrete. In perfect single crystals the wavefunction of an electron can extend over the entire crystal but the potential within the lattice as well as population of states determines conductivity. Localized wavefunctions, like those in amorphous OEs, imply discrete electronic states which charge carriers "hop" in and out of, thus charge hopping.[209]

Describing charge hopping usually includes components of Marcus' theory, the tight-binding approximation, and the Hubbard model.[185, 210-216] Reorganization energy is

the mainstay of Marcus's theory in most descriptions of charge hopping (figure 2, equations 2-5)[183, 185, 211-213, 217-221]. The Hubbard model is a tool linking the two electronic structure extremes of wide dense bands and wavefunction localization to a single molecule.[216] The Hubbard model appears in most CT theory as a charge transfer or hopping term in the Hamiltonian (equation 26) that acts on molecular states.[185, 214, 222] The tight-binding approximation includes only nearest neighbor interactions. In the narrowband regime where charge hopping occurs, vibrational dynamics play a larger role in modulating electronic overlap. Electron-phonon coupling is greatest when electronic bandwidths are on the order of $k_B T$ at 298 K ($\approx$25 meV).[223]

Early on it was suggested that charge mobility would be affected by electron-phonon coupling though electronic overlap is typically thought of as the main contribution to charge mobility.[224] In the charge hopping regime electron-phonon coupling and disorders can have an effect equal to or greater than electronic overlap. [185]Single crystals are more accurately modeled by a band transport type model.[225-227] In band transport electrons can be scattered by phonons but the effect is not nearly as significant as electron-phonon coupling in the hopping regime.[225-227] In amorphous systems in the charge hopping regime the electron-phonon coupling effects on charge mobility may differ between subensembles. This may result in preferential CT where certain configurations of molecules facilitate charge hopping better than other configurations. Electron-phonon coupling effects in SAMs or other layered systems may come from substrates as well.[228-230] TiO_2 nanoparticle film dynamics that affect CT could be an avenue of investigation.[94, 229, 230]

A.3 Marcus Theory Related to Charge Transfer

In typical solution-processable molecular OEs charge transfers to and from discrete sites where charge localization occurs. Charge localization, or polaron formation, is the result of nuclear rearrangement after a charge carrier moves to a molecule.[231, 232] Nuclear rearrangement includes effects from solvent or neighboring molecules. Polaron formation has an energy of stabilization. This energy of stabilization acts to bind a charge carrier to a site or molecule and is directly connected to CT rates via Marcus theory.[165, 183-185, 210-213, 222, 233, 234] The following equations illustrate the crux of Marcus theory:

$$CT: A_1^{\pm} + A_2 \underset{A^*}{\rightarrow} A_1 + A_2^{\pm} \tag{39}$$

$$Rate_{CT} = k[A^*] \tag{40}$$

$$k = Ce^{\left(-\frac{\Delta G^*}{k_B T}\right)} \tag{41}$$

$$\Delta G^* = \frac{\lambda}{4}\left(1 + \frac{\Delta G^o}{\lambda}\right)^2 \tag{42}$$

Here A^* is the transition state structure, k is the rate constant, C is a constant depending on the nature of CT[210], ΔG^* is the free energy change from the ground state to
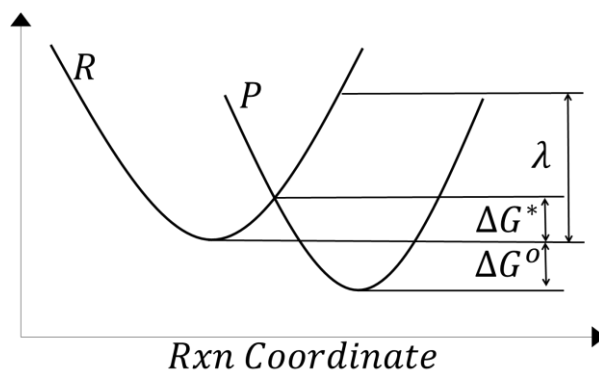
Figure 65: This is a graphical representation of reorganization energy. Change in free energy of reaction can be positive, negative, or zero. There is possibility that ΔG° is extremely large and negative such that the reactants must distort away from product geometry for surfaces to intersect and the reaction rate is low even with low transition state energy. This would mean that curve P above intersects curve R to the left of the minimum. Physically this means a much distorted product state is formed.

the transition state, k_B is Boltzmann's constant, T is temperature, ΔG^o is the free energy change of reaction, and λ is the reorganization energy. This is pictured in figure 2 where R is the reactant potential energy surface, P is the product potential energy surface, and λ is the energy required to distort the reactant state to the product state minimum without electron transfer.[235] ΔG^o for CT between identical species is zero.

Reorganizational energy which results from nuclear rearrangement can be written in terms of normal modes of vibration. Interaction between electronic energy and vibrational modes is called electron-phonon coupling.[185] There are two types of electron-phonon coupling: on-diagonal (intramolecular), and off-diagonal (intermolecular). On-diagonal coupling is the modulation of a site or molecular electronic energy by vibrational modes on that same site or molecule. Off-diagonal coupling is the modulation of a site or molecular electronic energy by vibrational modes of other sites or molecules. Room-temperature thermal activation of vibrational modes that modulate electron-phonon coupling contributes to dynamic disorder.[185] Structural motions due to this component of dynamic disorder will perturb the frequency of the chromophore being observed and this is how these particular vibrational dynamics are measured using 2D-IR.

There are also on and off-diagonal static disorders.[185, 222] Static disorder can be due to defects in OEs or their composition. Large static disorder or heterogeneity was indicated in 2D-IR spectra as a lack of complete spectral diffusion or broadening along the pump and probe axes. This indicated that the chromophore of interest did not experience all environments or configurations within an ensemble. This meant that FFCFs modeled as a sum of decaying exponentials would not decay to zero as long as the time required for an analyte to experience a configuration was much longer than the time of measurement or

dynamics.[32] The large amount of static heterogeneity in the TiO$_2$ films dictated the FFCF was not a primary means of analysis for the vibrational dynamics that might have related to CT.

Static inhomogeneity or heterogeneity in this study was referred to as vibrational environment. Marcus theory directly links vibrational environment and vibrational dynamics with the rate of CT and charge localization due to nuclear rearrangement. Environment dictates the free energy of reaction while the normal modes and structural fluctuations of a molecule are the mechanisms of reorganization of reactant and product states. Unique vibrational environment will result in unique IR frequency of a given chromophore. This frequency will be modulated by dynamics. Vibrational dynamics will likely be a function of species but it is not impossible that different vibrational environments will have different vibrational dynamics. Dynamics that reflect nuclear rearrangement of a given state with high CT could direct rational design of high mobility OEs. Connecting vibrational frequencies to distinct configurations or environments would ultimately have required a computational collaboration.

A.4 Charge Mobility Compared to Charge Hopping

This fundamental description of the relation between dynamics, environment, and CT in OEs remains largely unchanged since the 1950's. Advances in research capability continually improve accessibility and accuracy of results for more complex systems.[183, 185, 213, 221, 236-238]Modeling of materials like pentacene and oligothiophenes by Brédas and coworkers has outlined some of the factors affecting mobility: pressure, density, packing, wavefunction overlap, temperature, carrier density, electric field, disorder, and

impurities.[185] Despite progress, neither modeling nor experiment has resulted in usable high mobility molecular semiconductors in spite of the thousands synthesized and tested.[183]

Charge mobility is an intrinsic material property often used to describe charge transport in OEs. Charge mobility (μ) is related to drift velocity and diffusion by the following:[239-241]

$$\mu = \frac{v_d}{E} = \frac{eD}{k_b T} \tag{43}$$

Large mobilities mean higher drift velocities (v_d) for a given applied field (E) and are directly proportional to high diffusion coefficients (D). Drift velocity is proportional to current so large mobilities mean reasonable conduction for typical device operating voltage (V). Charge (e) carrier diffusion is the bulk system property that is proportional to mobility.

Diffusion of N3 holes due to photoexcitation has been measured to be approximately 10^{-9} mol cm^{-2}.[242, 243] This corresponds to a mobility of approximately $4*10^{-7}$ cm^2 V^{-1} s^{-1} by the Einstein relation (equation 27).[185] The relation between current and mobility is the following:[240]

$$I = \mu EnAe = \frac{eD}{k_b T} \frac{V}{cm} nAq \tag{44}$$

Where I is current, n is charge carrier density per unit volume, A is cross sectional area of the conductor, E is the field ($\frac{V}{cm}$), and e is the charge of the charge carrier. For a given system of a known geometry the diffusion can be inferred from voltage and current if the

carrier density is known. Diffusion coefficients and mobilities are bulk properties as opposed to mechanical properties such as charge hopping rates from molecule to molecule. In a heterogeneous system there is an ensemble of charge mobilities just as there is an ensemble of configurations. Decomposition of the ensemble CT rates would indicate if charge mobility reflected the mean CT rate in the system or if a broad distribution of rates gave rise to a specious mobility.

Factors that affect mobility are crystal packing, molecular weight or size, orbital wavefunction overlap, pressure, temperature, density, and vibrational environment.[185] The salient factors will depend on the system. For instance, SAMs of N3 on TiO_2 nanoparticle would depend on packing due to surface binding environment, wavefunction overlap, and vibrational dynamics. Each specific environment corresponds to a unique state. If one knew all the states, the Hamiltonian corresponding to a property of interest could be used to perate on all states. Summing the contributions of each state connects quantum mechanical to bulk properties and measurements.

Richard Feynman framed the relationship between operators and state or wavefunction transitions in a very simple way:[180]

$$\langle Finish|Through|Start \rangle = \langle Final\ State|Operator|Initial\ State \rangle \qquad (45)$$

The simplicity of this equation clarifies the connection of reorganization energy and vibrational dynamics to charge hopping through the system Hamiltonian:[185, 222, 244]

$$\hat{H}_{total} = \hat{H}_o + \hat{H}_1 + \hat{H}_2 + \hat{H}_3 + \hat{H}_4 \qquad (46)$$

146

$$\hat{H}_o = \sum_n \varepsilon_n \hat{a}_n^+ \hat{a}_n + \sum_{n'} \hbar\omega_{n'} (\hat{b}_{n'}^+ \hat{b}_{n'} + \frac{1}{2}) \qquad (47)$$

$$\hat{H}_1 = \sum_{mn} J_{mn} \hat{a}_m^+ \hat{a}_n = \sum_{mn} t_{mn} \hat{a}_m^+ \hat{a}_n = \sum_{mn} \langle m|\hat{H}_{electronic}|n\rangle \qquad (48)$$

$$\hat{H}_2 = \sum_{n'n} g_{n'n}^2 \hbar\omega_{n'} \hat{a}_n^+ \hat{a}_n (\hat{b}_{n'} + \hat{b}_{n'}^+) \qquad (49)$$

$$\hat{H}_3 = \sum_{mnn', m\neq n} f_{mnn', m\neq n}^2 \hbar\omega_{n'} \hat{a}_m^+ \hat{a}_n (\hat{b}_{n'} + \hat{b}_{n'}^+) \qquad (50)$$

$$\hat{H}_4 = \sum_n \delta\varepsilon_n \hat{a}_n^+ \hat{a}_n + \sum_{mn, m\neq n} \delta J_{mn} \hat{a}_m^+ \hat{a}_n \qquad (51)$$

Electronic creation and annihilation operators for a charge carrier at site n are $\hat{a}_n^+$ and $\hat{a}_n$ respectively. The same for vibrational quanta of normal mode n' are $\hat{b}_{n'}^+$ and $\hat{b}_{n'}$. Electronic site energy is ε_n. Variation in site energy due to static disorder is denoted by $\delta\varepsilon_n$. The transfer integral or interaction energy J_{mn} describes charge transfer from site m to n per equation 29. Variation in transfer integrals due to static disorder is denoted δJ_{mn}. The strength of coupling between electronic energy on site n and a normal mode of vibration n' is described by a dimensionless constant $g_{n'n}^2$. A similar constant for coupling between a normal vibrational mode n' on site n with the electronic energy on site m is given by $f_{mnn', m\neq n}^2$. These Hamiltonians describe site energy ($\hat{H}_o$), charge transfer ($\hat{H}_1$), coupling between vibrational quanta and site energy ($\hat{H}_2$), coupling between vibrational quanta of one site with energy of a different site ($\hat{H}_3$), and variation from a perfect system or solid periodic lattice with no phonons ($\hat{H}_4$). Vibrational-electronic couplings could also be nonlinear (i.e. $(\hat{b}_{n'} + \hat{b}_{n'}^+)^2$). Under the tight binding approximation the summations

over m and n are only for nearest neighbors.[245] This approximation is made when it is assumed that electrons are highly localized to a given site.

Connecting Experiment to Theory via Marcus Theory Treatment

The terms most relevant to the connection between vibrational dynamics and charge transfer are the second and third Hamiltonians:

$$\hat{H}_2 = \sum_{n'n} g_{n'n}^2 \hbar\omega_{n'} \hat{a}_n^+ \hat{a}_n (\hat{b}_{n'} + \hat{b}_{n'}^+) \tag{52}$$

$$\hat{H}_3 = \sum_{mnn',m\neq n} f_{mnn',m\neq n}^2 \hbar\omega_{n'} \hat{a}_m^+ \hat{a}_n (\hat{b}_{n'} + \hat{b}_{n'}^+) \tag{53}$$

Coropceanu and coworkers showed that the coupling parameters are related to the relaxation or reorganization energies. Reorganization energies are the mainstay of Marcus theory in the majority electron transfer theory papers.[183, 185, 212, 219, 222, 233, 244, 246] Localization of charge carriers to form polarons occurs through nuclear rearrangement.[185, 231, 232, 247]

$$E_{pol} = \lambda_{relax} = \sum_{n'} \lambda_{n'} = \sum_{n'} \frac{g^2(n')}{\hbar\omega_{n'}} = \sum_{n'} \frac{V(n')^2}{2M_{n'}\hbar\omega_{n'}^3} \tag{54}$$

Here $V(n')$ is the derivative of electronic energy with respect nuclear displacement along a normal mode of vibration. The reduced mass for a vibration is $M_{n'}$, E_{pol} is polaron binding energy, $\lambda_{n'}$ is the reorganization energy due to vibrational mode n', and λ_{relax} is the on site relaxation energy. This assumes all modes are harmonic.[185] For charge transfer between the same species the reorganizational energy from equation 5 is twice the onsite relaxation energy.[185, 212]

$$k = Ce^{\left(-\frac{\Delta G^*}{k_b T}\right)} = Ce^{\left(-\frac{\frac{\lambda}{4}\left(1+\frac{\Delta G^o}{\lambda}\right)^2}{k_b T}\right)} = Ce^{\left(-\frac{\frac{2\lambda_{relax}}{4}\left(1+\frac{\Delta G^o}{2\lambda_{relax}}\right)^2}{k_b T}\right)} \tag{55}$$

$$= Ce^{\left(-\frac{\frac{2E_{pol}}{4}\left(1+\frac{\Delta G^o}{2E_{pol}}\right)^2}{k_b T}\right)}$$

Equation 36 is an approximate case where λ does not include solvent, off-diagonal coupling ($\hat{H}_3$), or on and off diagonal disorder ($\delta\varepsilon_n$ and δJ_{mn} respectively). These ignored terms are also the most difficult to calculate. Modeling of rigid bodies with fixed orientations and the potential energy surface of a single molecule in relation to its own normal vibrational modes can be done.[212] Some Monte Carlo simulations of the static disorder terms have been performed using a Gaussian disorder model.[198] This describes site energy in terms of a Gaussian distribution. It is clear that the ignored terms are computationally intractable when considering specifically every molecule of an ensemble, pair-types of neighboring molecules, and configurations in heterogeneous morphology. Heterogeneous systems typically result from solution processing of OEs. Computation of these systems could be accomplished by approximation, but it is not clear if current computational capacity can manage simulations at the level of accuracy needed for predicting OE design. CT study involves quantum descriptions and ensemble observations.

A.5 I$_2$ with 100V experiment

Meaurements of ground state conduction with experiments performed in the dark to avoid electronic excitation were carried out. To achieve highly conductive samples the N3 SAMS were doped with iodine. This induces a reversible shift in the NCS$^-$ stretch from 2113 cm^{-1} to 2138 cm^{-1}. Doping was accomplished by trapping iodine between two

windows with an O-ring spacer (figure 8). The O-ring spacer also served to hold electrical
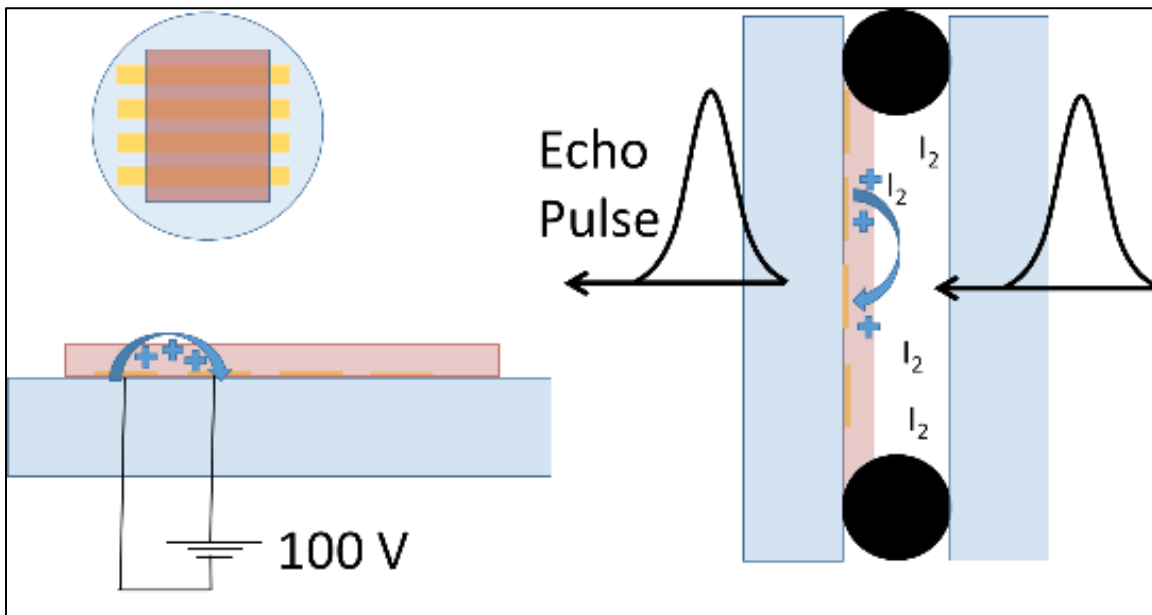
contacts onto the sample window.

Figure 66: Schematic of experimental sample. Black circles in the right image represent an o-ring cross section. The yellow strips in the upper left image represent gold contacts underneath the film represented by the larger rectangle.

To apply voltage across the films 300 nm thick gold contacts were deposited using

the CHA Evaporator at the University of Minnesota Nanofabrication Center. Gold was

chosen because it withstands iodine exposure reasonably well and is very conductive.

Contacts were deposited at a rate of 0.1 nm per second for 5 nm followed 0.5 nm per second

for the remaining 295 nm. Deposition occurred at room temperature under a pressure of

less than 1.6 microTorr. Contacts were patterned using 120 micron thick stainless steel

shadow masks. Five contacts per window enabling four regions for laser light had spacing

of 0.75 mm and 1 mm (2 each). Contacts were 3.1 mm wide. The different spacing of the

contacts was intended for future four point probe measurements to determine charge

mobility.

The TiO$_2$ films themselves without iodine are not excessively conductive. When applying 100 V using a Keithley model 617, current continues to rise slowly to only tenths of nanoamps and drops off slowly to hundredths of nanoamps. This appears to be TiO$_2$ film capacitance. When films are trapped in a chamber with I$_2$ vapor that completely dopes the films, 100 V induces .5 to 1 microamps and current response to voltage is virtually instantaneous. The Keithley is attached to external stainless steel foil contacts that were sandwiched against the deposited gold contacts by the O-ring used to trap iodine vapor with the sample. Resistance between the stainless foil and gold was less than 2 Ω. 2D-IR spectra were collected on this system with no voltage and 100 V applied.
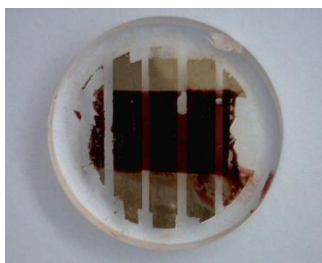

Figure 67: Sample of N3 adsorbed to TiO$_2$ over gold contacts.

Figure __ shows the 2D-IR spectra of N3 collected under a variety of conditions. Listed on each spectra are the time (T$_w$) relative to zero that the spectra were collected at (0.1, 2.5, 8.0, and 16.0 ps). Figure 13 displays data collected from an iodine doped SAM of N3 with and without voltage applied at T$_w$'s 0.1, 2.5, 8.0, and 16.0 ps.[248] The difference in peak shape evolution with volatage applies is very suggestive of charge transfer being evinced by off-diagonal peak intensity. In this case the small difference makes this impossible to assess by absolute value spectra. The off-diagonal peak intensity is extremely sensitive to phasing parameters. To confirm whether or not this was charge transfer an experiment was carried out where voltage was turned on and off at each data

151

point. That is, while scanning τ voltage was turned on and a data point was collected followed by turning voltage off and collecting a data point at the same τ time point. This way the voltage on and voltage off spectra should have identical phasing parameters. This way even if they were poorly phased they should indicate a difference. Then the no-voltage spectra were subtracted from voltage spectra to obtain the difference that would be charge transfer. The resulting difference was nothing. There was no observable charge transfer.

It would have been very exciting to publish charge transfer measurements. It was an arduous amount of work to negate this exciting but specious observation. The work with N3 and Z907 remains the longest standing project aimed at the initial motivation of this thesis. After disproving charge transfer a back of the envelope calculation using the TiO_2 NP diameter, film thickness, and N3 Van der Waals radius revealed that approximately one molecule in one million could explain the current that was measured. Even if void spaces were high it is unlikely that this ratio would increase to one in one hundred. Measuring ground state charge transfer would require a molecule in which the charge localized directly on the chromophore being observed. The peak width and resolution between the neutral and charged species would then determine sensitivity.
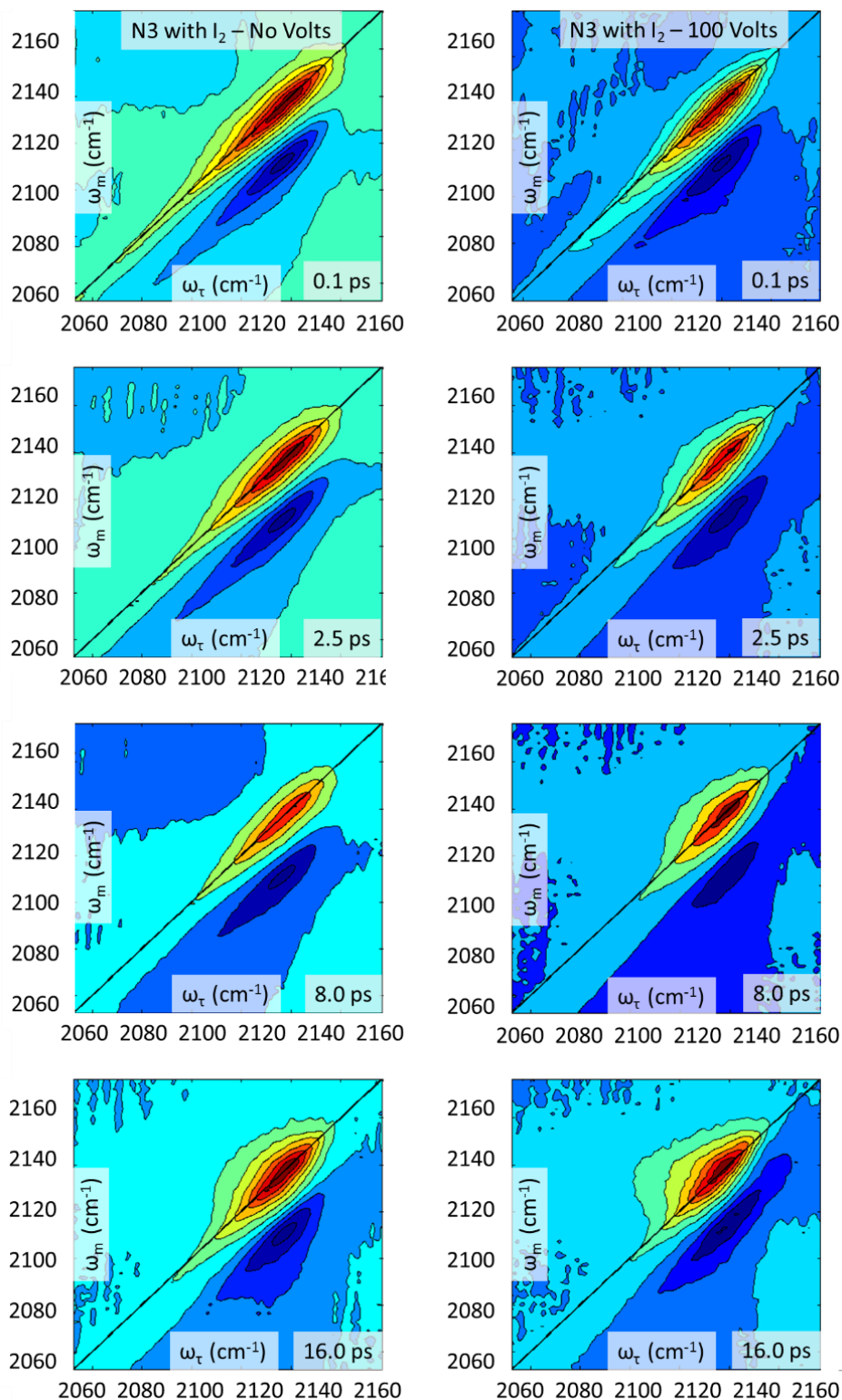
Figure 68: On the left are iodine doped N3 spectra with no voltage applied. There are dynamics due to the iodine. The squareness of the peak in both the 0 to 1 and 1 to 2 transition may indicate charge diffusion. On the right is the same sample with 100 V applied. The peak is much squarer than those with no voltage. This may be due to the applied field indicating increased CT at 16 ps.

153